AFRL-AFOSR-VA-TR-2022-0022

Uncovering Flow Physics for High-Speed Cavity Flow Control

Ukeiley, Lawrence
UNIVERSITY OF FLORIDA
207 GRINTER HALL
GAINESVILLE, FL,
US

11/04/2021
Final Technical Report

Air Force Research Laboratory
Air Force Office of Scientific Research
Arlington, Virginia 22203
Air Force Materiel Command

REPORT DOCUMENTATION PAGE

Form Approved
OMB No. 0704-0188

1. REPORT DATE *(DD-MM-YYYY)*	**2. REPORT TYPE**	**3. DATES COVERED** *(From - To)*
04-11-2021	Final	30 Sep 2017 - 29 Jun 2021

4. TITLE AND SUBTITLE
Uncovering Flow Physics for High-Speed Cavity Flow Control

5a. CONTRACT NUMBER

5b. GRANT NUMBER
FA9550-17-1-0380

5c. PROGRAM ELEMENT NUMBER
61102F

6. AUTHOR(S)
Lawrence Ukeiley

5d. PROJECT NUMBER

5e. TASK NUMBER

5f. WORK UNIT NUMBER

7. PERFORMING ORGANIZATION NAME(S) AND ADDRESS(ES)
UNIVERSITY OF FLORIDA
207 GRINTER HALL
GAINESVILLE, FL
US

8. PERFORMING ORGANIZATION REPORT NUMBER

9. SPONSORING/MONITORING AGENCY NAME(S) AND ADDRESS(ES)
AF Office of Scientific Research
875 N. Randolph St. Room 3112
Arlington, VA 22203

10. SPONSOR/MONITOR'S ACRONYM(S)
AFRL/AFOSR RTA1

11. SPONSOR/MONITOR'S REPORT NUMBER(S)
AFRL-AFOSR-VA-TR-2022-0022

12. DISTRIBUTION/AVAILABILITY STATEMENT
A Distribution Unlimited: PB Public Release

13. SUPPLEMENTARY NOTES

14. ABSTRACT

In this study, the flow physics and control of high speed flows over open cavities were examined through both numerical and experimental methodologies. The flow conditions involved both subsonic and supersonic free stream conditions and the analysis not only included extracting information about the flow but also the development on various data driven analysis techniques. In this context, the bene fits of including frequency in the application of the Proper Orthogonal Decomposition was demonstrated using time resolved velocity measurements. The importance of frequency based decomposition was used as the motivation to develop a linear multiple-input/multiple-output model that determines the optimal transfer functions between the input cavity wall pressure and the output velocity fi eld as part of spectral analysis modal methods (SAMMs). With the numerical simulations resolvent analysis was leveraged to determine optimal spanwise wavenumber and frequency of the unsteady actuation input for a fi xed momentum coefficient. Overall, this study developed tools that can be used for extracting wavenumbers and frequencies important to high speed cavity flows and demonstrated how to introduce

15. SUBJECT TERMS

16. SECURITY CLASSIFICATION OF:			**17. LIMITATION OF ABSTRACT**	**18. NUMBER OF PAGES**	**19a. NAME OF RESPONSIBLE PERSON**
a. REPORT	**b. ABSTRACT**	**c. THIS PAGE**			GREGG ABATE
U	U	U	UU	109	**19b. TELEPHONE NUMBER** *(Include area code)* 425-1779

Uncovering Flow Physics for High-Speed Cavity Flow Control

Lawrence Ukeiley & Surabhi Singh
Mechanical and Aerospace Engineering, University of Florida

Louis Cattafesta & Yang Zhang
Mechanical Engineering, Florida State University

Kunihiko Taira & Qiong Liu
Mechanical Engineering, UCLA

Yiyang Sun
Mechanical and Aerospace Engineering, Syracuse University

September 9, 2021

Summary

In this study, the flow physics and control of high speed flows over open cavities were examined through both numerical and experimental methodologies. The flow conditions involved both subsonic and supersonic free stream conditions and the analysis not only included extracting information about the flow but also the development on various data driven analysis techniques. In this context, the benefits of including frequency in the application of the Proper Orthogonal Decomposition was demonstrated using time resolved velocity measurements. The importance of frequency based decomposition was used as the motivation to develop a linear multiple-input/multiple-output model that determines the optimal transfer functions between the input cavity wall pressure and the output velocity field as part of spectral analysis modal methods (SAMMs). With the numerical simulations resolvent analysis was leveraged to determine optimal spanwise wavenumber and frequency of the unsteady actuation input for a fixed momentum coefficient. Overall, this study developed tools that can be used for extracting wavenumbers and frequencies important to high speed cavity flows and demonstrated how to introduce them as input for flow control.

Contents

1 Introduction

Essentially since the start of jet powered flight the flow over an open cavity has presented complex problems that can be detrimental to flight and the aircraft. The canonical representation of this type of cavity flow has provided an intriguing flow that represents contains a complex aeroacoustic environment that has been studied to control the detrimental effects. Large pressure fluctuations arise on the cavity floor and walls that can result in pressure tones of very high amplitudes (175 dB or 11.25 kPa) which poses a major acoustic and structural problem. These pressure fluctuations have been attributed to shear layer instabilities arising in the flow due to complex shear layer - cavity surface interactions. Research has revealed the associated flow and acoustics characteristics within the cavity are dependent on geometric parameters of the cavity as well as free stream and approaching flow characteristics. The current study deals with open cavity flows under transonic and supersonic free-stream conditions. The cavities and flow conditions considered in the current study represent a good prototype for flow observed around weapon bays and other open recesses in modern high speed aircraft.

When the flow goes past an open recess, upon encountering the stagnant flow inside it, a shear layer gets generated. As the flow moves downstream, the shear layer interacts with the rear wall generating pressure fluctuations that travel upstream further exciting the shear layer near the leading edge. This sets up a positive feedback loop making the flow highly unstable. One of the major goals of cavity flow control is to effectively reduce large pressure fluctuations to ensure less damage to the overall cavity structure and objects inside it.

Due to the rich dynamics and resulting flow instabilities, the study of cavity flows has revolved around studying the flow physics and applications of flow control methodologies. Various experimental and numerical studies have helped gain better control of the flow

through the use of various passive and active control designs. However, most of these attempts have been ad-hoc and there is scope for better physics-based designs to achieve better control. With the advancements in experimental and analytical techniques such as high speed imaging and machine learning techniques, it is now possible to extract intricate dynamics of the flow in terms of specific conditional events which previously remained largely unknown. Also, recent numerical and experimental work have elucidated the nature and wavelength of instabilities in open cavities and how they relate to experimentally employed control. With this wealth of information, the current work attempts to design experiments and use analytical techniques to understand conditional flow events in the cavity flow field which can give better idea of the cavity flow physics for better control. Concurrently, this work leverages previous control and instability studies to better design and understand cavity flow control.

1.1 Document Outline

The remainder of this document will be have three additional sections. Section two provides the particulars on the simulations and experimental approaches that were employed in this study as well as details of some of key data processing techniques. The third section provides the bulk of this document and details the results from the computational and experimental efforts. The final section will summarize the results of the computational and experimental efforts by drawing some conclusions and discussing future investigations.

2 Approaches

The combined numerical and experimental study utilized several facilities, detailed Large Eddy Simulations and many advanced data analysis techniques which are all discussed in this section.

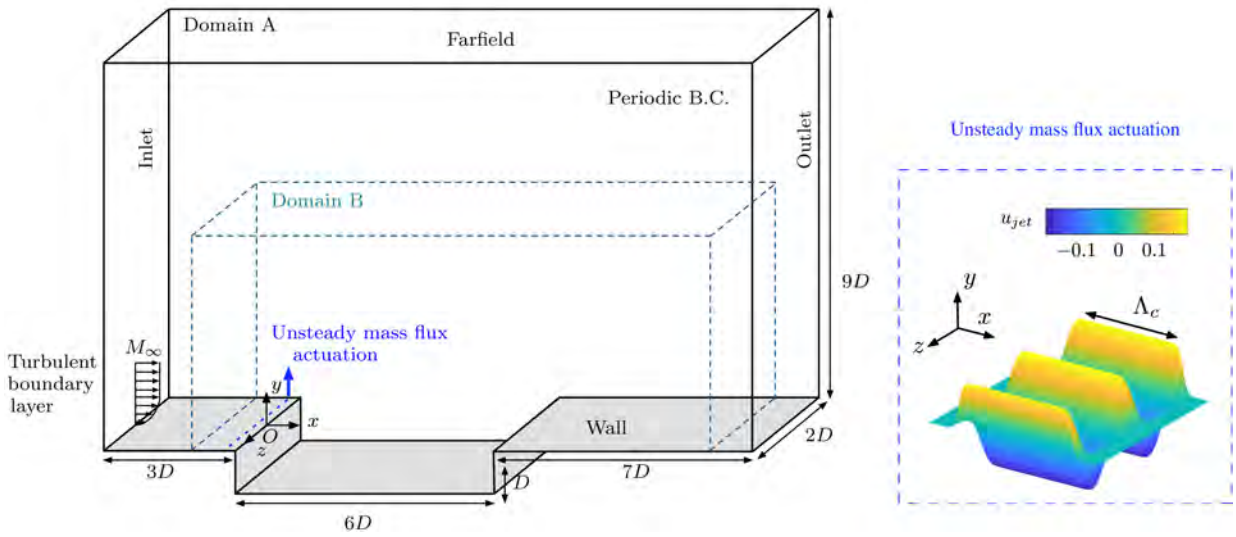

Figure 1: Setup for computational domain and boundary conditions. Domain A is used for the baseline and controlled LES cases. Domain B is used for resolvent and dynamic mode decomposition analyses. The right insert depicts the unsteady actuation control profile for $\beta_c = \pi$.

2.1 Computational Approach

2.1.1 Large eddy simulation setup

We study the turbulent cavity flow with LES using a compressible flow solver *CharLES* (Khalighi et al., 2011; Brès et al., 2017). The solver is based on a second-order finite-volume discretization and a third-order Runge–Kutta time integration scheme. For the present LES, Vremen's sub-grid scale model (Vreman, 2004) is utilized and the Harten-Lax-van Leer contact scheme (Toro et al., 1994) is used to capture shocks in the supersonic flows. Random Fourier modes are superimposed to the one seventh power law velocity profile to simulate unsteady fluctuations from the inlet (Bechara et al., 1994). No-slip and adiabatic wall boundary condition is specified along the cavity walls. A sponge boundary condition is applied at the farfield and outlet boundaries to damp out exiting waves and prevent numerical reflections.

The computational setup for the present study is shown in figure 1. A Cartesian coordinate system is used with its origin placed at the spanwise center of cavity leading edge, with x, y and z denoting the streamwise, wall-normal and spanwise directions, respectively. The computational domain extends upstream and downstream by 3 and 7 times of the cavity depth, respectively. The farfield extent is set to be 9 times of the cavity depth. The computational domain is discretized with a structured mesh with 14 million cells for the baseline and 16 million cells for the controlled simulations, for which mesh refinement is applied in the vicinity of the actuators. This computational setup has been verified to accurately characterize flow properties observed in experimental studies (Zhang et al., 2019; Sun et al., 2019). A small three-dimensional domain, labeled as Domain B in figure 1, is used for the modal analyses. It has a upstream length equal to the cavity depth. The downstream and farfield boundaries are placed 5 times of cavity depth away. The grid size for Domain B is approximately 70,000 cells.

2.1.2 Unsteady actuation setup

The active flow control of unsteady blowing and suction is introduced along the leading edge of the cavity through a mass flux boundary condition, as illustrated by the blue dashed line in figure 1. The actuator is located at $x_c = -0.0698/D$ with a streamwise slot extent of $\Lambda_c = 0.0175/D$ following our previous experimental studies (Lusk et al., 2012; George et al., 2015; Zhang et al., 2019). The unsteady actuation is prescribed with a wall-normal velocity profile of

$$u_{\text{jet}}(x, z, t) = A \sin(\omega_c t) \Phi(x, x_c, \Lambda_c) \cos(\beta_c z), \tag{1}$$

where A is the actuation amplitude, ω_c and β_c are the actuation frequency and spanwise wavenumber, respectively. In what follows, we report the actuation frequency ω_c through its dimensionless cavity length-based Strouhal number $St_c = \omega_c L/(2\pi u_\infty)$. The spatial

velocity profile for the actuator is given by

$$\Phi(x, x_c, \Lambda_c) = \frac{1}{4}\left\{1 + \tanh\left[\kappa_1(x - x_c + \Lambda_c/\kappa_2)\right]\right\}\left\{1 - \tanh\left[\kappa_1(x - x_c - \Lambda_c/\kappa_2)\right]\right\} \quad (2)$$

along the streamwise direction to avoid the velocity discontinuity at the edge of the actuator. Here, we choose $\kappa_1 = 2000$ and $\kappa_2 = 2.6$. The actuation frequency and spanwise wavenumber will be selected based on the resolvent analysis as discussed later in §**??**.

The actuation efforts in this study are reported in terms of the unsteady momentum coefficient defined by

$$C'_\mu \equiv \frac{J}{\frac{1}{2}\rho_\infty u_\infty^2 W \delta_0}, \quad (3)$$

where $J = (\rho_\infty \omega_c/2\pi)\int_{T_c}\int_S u_{\text{jet}}(x, z, t)^2 \mathrm{d}s\mathrm{d}t$ is the integral of momentum over the actuation area S and the period of the unsteady control actuation $T_c = 2\pi/\omega_c$. The denominator is the equivalent incoming freestream momentum through the boundary layer height at the leading edge of the cavity. In the present study, we set the unsteady momentum coefficient to be $C'_\mu = 0.02$, following canonical values from past unsteady control studies (Elimelech et al., 2011; Shaw, 1998; Williams et al., 2007).

The control effects are assessed using the surface integrated root-mean-square pressure on the aft and bottom walls ($\tilde{\Omega}$) defined as

$$\Delta\tilde{p}_{\text{rms}} = \frac{(\tilde{p}_{\text{rms,c}} - \tilde{p}_{\text{rms}})}{\tilde{p}_{\text{rms}}}, \quad \text{where} \quad \tilde{p}_{\text{rms}} = \int_{\tilde{\Omega}} \frac{p_{\text{rms}}}{\frac{1}{2}\rho_\infty u_\infty^2}\mathrm{d}S \quad (4)$$

and $\tilde{p}_{\text{rms,c}}$ is the surface integrated pressure fluctuation for the controlled cavity flows. The variable $\Delta\tilde{p}_{\text{rms}}$ quantifies the relative change of normalized root mean square (rms) pressure fluctuations over the cavity walls. Later in this paper, we show via resolvent analysis that the above actuator location is indeed appropriate for amplifying the injected perturbation over the cavity.

2.2 Experimental Approach

Throughout this project windtunnels at both the University of Florida and Florida State University were utilized and the following subsections will provide short descriptions of them.

2.2.1 Subsonic Flow Facility

The experiments are performed in the Pilot Wind Tunnel facility located at the Florida Center for Advanced Aero-Propulsion (FCAAP) at the Florida State University (FSU). This wind tunnel is a blowdown facility with air supplied from 3.4 MPa storage tanks. High-speed subsonic flow (Mach 0.6 for the current experiments) is achieved using a converging nozzle. The stagnation pressure, p_0, is measured by a pitot tube located inside the settling chamber using an Omega pressure transducer PX409-050A5V-XL with an uncertainty of $\pm$100 Pa). The stagnation temperature, T_0, is measured by a RTD (uncertainty of $\pm$ 0.1 K) in the settling chamber. The static pressure, p_s, is measured using a pressure transducer (Omega PX303-015A5V, uncertainty of $\pm$250 Pa) via a pressure tap on the sidewall upstream of the cavity model. Wind tunnel flow conditions are monitored and controlled through a LabVIEW program.

As shown in Fig. 2, the origin of the coordinate system is fixed at the middle of the cavity leading edge with the $\tilde{x}$, $\tilde{y}$, and $\tilde{z}$ axes denoting the streamwise, normal, and spanwise directions, respectively. The rectangular cavity model has a dimension of $L/D = 6$ and $W_c/D = 3.85$ with $D = 26.5$ mm. The incoming dimensionless turbulent boundary layer thickness at the cavity leading edge, δ_0/D, is approximately 0.16 with a shape factor of approximately 1.4 at Mach 0.6. The cavity model has an acoustically-treated ceiling (MKI Dynapore P/N 408020 metal sheet and 76.2-mm-thick bulk fiberglass) opposite to the cavity opening.

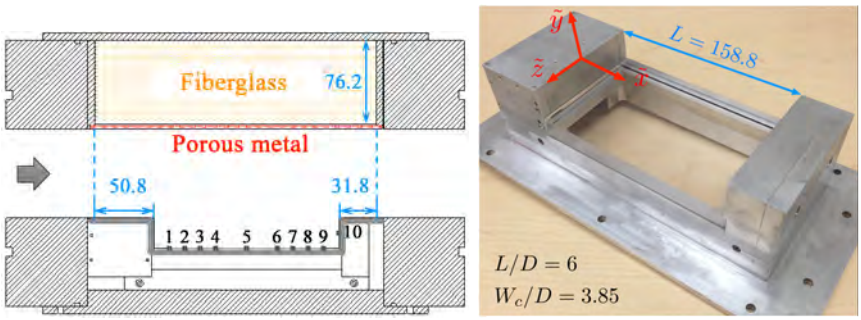

Figure 2: Schematic of the cavity model (units are in mm). Coordinates system $\tilde{x}$, $\tilde{y}$, and $\tilde{z}$ are non-dimensionalized by D.

2.2.2 Supersonic Flow Facility

Experiments were conducted in an intermittent, supersonic blowdown wind tunnel facility located in the Department of Mechanical and Aerospace Engineering (MAE) at the University of Florida. A Sullair (model LS-20T) compressor with the help of a dessicant dryer supplies dry air to two 14.39 m^3 tanks up to a pressure of 1447 kPa (210 lbf/in^2). This air is then allowed into the supersonic wind tunnel containing the cavity test section through a pneumatic control valve. After passing through the wind tunnel, the air is finally exhausted out of the building with the help of an exhaust pipe which vents it to the environment.

Details of the design of this wind tunnel was reported in **?** and only pertinent details will be discussed here. When the flow enters the wind tunnel after passing through the control valve, it first reaches the plenum after which it is passed through honeycomb structures to cut out any large scale flow fluctuations in the flow conditioning section. The flow then passes through a transition piece where the cross section changes from a circular pipe to a rectangular duct. This flow enters a converging-diverging nozzle which produced nominally a Mach 1.4 flow for experiments. This is followed by a test section with removable bottom plate where a desired structure can be placed for testing. The test section is 101.6 mm high, 76.2 mm wide and 228.6 mm long. After passing through the test section, the air is expanded using a diffuser and exhausted through a 304.8 mm piping. Figure 3 shows a

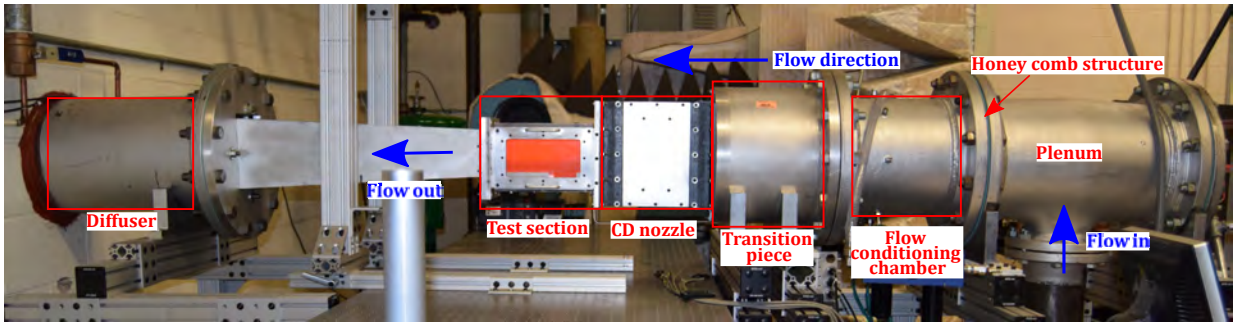

Figure 3: Supersonic Wind Tunnel facility with cavity test section inserted.

photograph of the wind tunnel test facility with the various sections labeled.

The incoming boundary layer thickness (δ), displacement thickness (δ^*), and momentum thickness (θ) along floor of the cavity at the leading edge were measured to be 3.8 mm, 1.1 mm and 0.9 mm respectively from previous experiments (**?**). The conditions in the tunnel are monitored using variety of measurements to ensure repeatability and flow quality. A Druck PMP 4015 50 psia transducer with an accuracy of 0.08 % of full scale was used to measure the pressure in the flow conditioning chamber. Since the flow velocity in this section is low, the static and stagnation pressure can be assumed to be nearly equivalent. The static pressure was measured by a similar Druck PMP 4015 15 psia transducer (0.08 % accuracy) ahead of the cavity. The voltage output of these transducers are digitized using NI 9215 voltage input module. The experimental conditions were monitored and controlled through a Fisher control valve in conjuction with a LABVIEW virtual instrument (vi). Proportional-Integral control in LabVIEW was implemented which monitors the stagnation pressure and uses it as a feedback to send current output to open or close the Fisher valve at 20 Hz. The cavity test setup was controlled for a stagnation pressure of 140 kPa. The stagnation temperature in the plenum was measured using an Omega Engineering P-L-1 ultra precise RTD sensor. The observed pressures throughout the wind tunnel exhibit a maximum deviation of under 2 % from the set value. The maximum deviation in Reynolds number is 1.6 % from the mean value. Standard isentropic relationships were used to

calculate the Mach number, Ma and static temperature, T. Table 1 lists the mean or nominal value for various parameters in the flow.

Table 1: Typical flow parameters

	Ma	P_0	U_∞	Q_∞
Typical values	1.40	140 kPa	410 m/s	62.8 kPa

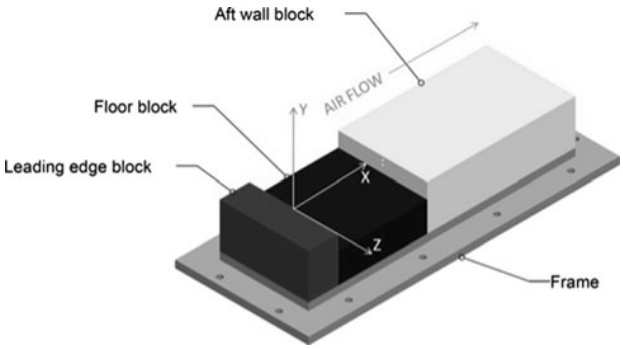

Figure 4: Cavity model inserted into the test section (Lusk et al., 2012)

The cavity model utilized here spans the full width of the wind tunnel with length, $L = 76.2\,mm$, width, $W = 76.2\,mm$ and depth, $D = 12.7\,mm$. This model is bolted on to the removable bottom plate of the test section, a drawing of the bottom plate along with the cavity which is inserted into the test section is shown in Figure 4.

2.3 Modal analysis

2.3.1 Resolvent analysis

Resolvent analysis is an operator-based modal analysis formulation that is capable of examining flow response to harmonic forcing input with respect to a given base state. For this analysis, the base state can be an equilibrium state or a time-average flow, provided that the flow is in statistical equilibrium. The dimensionless governing equation for fluid

flow is the (spatially discretized) Navier–Stokes equation expressed as

$$\frac{\partial \boldsymbol{q}}{\partial t} = N(\boldsymbol{q}), \tag{5}$$

where the state variable $\boldsymbol{q} = [\rho, \rho u, \rho v, \rho w, e]^T \in \mathbb{R}^{5m}$. Here, we have density ρ, velocity u, v, and w for streamwise x, transverse y, and spanwise z directions, and energy e. The number of grid points used to discretize the computational domain is denoted by m. All variables have been non-dimensionalized by the cavity depth and free stream values of the variables, and velocity is non-dimensionalized by free stream acoustic speed as described in Sun et al. (2017b). We decompose the flow state $\boldsymbol{q}$ into the 2D steady base state $\bar{\boldsymbol{q}}$ and the 3D perturbation $\boldsymbol{q'}$

$$\boldsymbol{q}(x, y, z, t) = \bar{\boldsymbol{q}}(x, y) + \boldsymbol{q'}(x, y, z, t). \tag{6}$$

Substituting this expression into Eq. (5), the governing equation for the perturbation becomes

$$\frac{\partial \boldsymbol{q'}}{\partial t} = \tilde{L}(\bar{\boldsymbol{q}})\boldsymbol{q'} + \boldsymbol{f'}, \tag{7}$$

where $\tilde{L}(\bar{\boldsymbol{q}})$ denotes the linear operator of the Navier–Stokes equations on $\boldsymbol{q'}$ and the term $\boldsymbol{f'}$ represents a forcing applied to the linear dynamical system. The above linearization holds only if $\bar{\boldsymbol{q}}$ is an equilibrium state. For non-equilibrium $\bar{\boldsymbol{q}}$, the forcing term $\boldsymbol{f'}$ can be interpreted as a combination of the right-hand-side of the original Navier–Stokes equation with respect to the base state, the nonlinear higher-order perturbation terms, and/or external forcing introduced into the fluid flow system. With the assumption that the flow to be examined is in a statistically stationary state, both forcing $\boldsymbol{f'}$ and perturbation $\boldsymbol{q'}$ can take the Fourier representations of

$$\boldsymbol{f'}(x, y, z, t) = \hat{\boldsymbol{f}}_{\omega,\beta}(x, y)e^{i(\beta z - \omega t)} + \text{complex conjugate}, \tag{8}$$

$$\boldsymbol{q'}(x, y, z, t) = \hat{\boldsymbol{q}}_{\omega,\beta}(x, y)e^{i(\beta z - \omega t)} + \text{complex conjugate}, \tag{9}$$

with real-valued radian frequency ω, real-valued spanwise wavenumber β, and $\hat{\boldsymbol{f}}_{\omega,\beta}$ and $\hat{\boldsymbol{q}}_{\omega,\beta}$ denoting spatial amplitude functions for forcing and perturbation, respectively. Here, we have assumed that the flow is spanwise periodic, although such assumption can be removed in general. By substituting Eqs. (8) and (9) into Eq. (7), the governing equation can be rewritten as

$$-i\omega\hat{\boldsymbol{q}}_{\omega,\beta} = L(\bar{\boldsymbol{q}};\beta)\hat{\boldsymbol{q}}_{\omega,\beta} + \hat{\boldsymbol{f}}_{\omega,\beta}. \tag{10}$$

When the system is unforced ($\boldsymbol{f}' = 0$), Eq. (7) reduces to an initial value problem, which can be solved for the homogeneous solution of Eq. (10) with $\hat{\boldsymbol{f}}_{\omega,\beta} = 0$. In other words, this can be formulated as an eigenvalue problem that analyzes the instabilities of the base flow. When the forcing term is nonzero, Eq. (10) describes the relationship between the flow response and harmonic forcing, which provides the particular solution of the inhomogeneous equation (Eq. (10)) for the system with a sustained forcing input.

For the forced system, by solving for $\hat{\boldsymbol{q}}_{\omega,\beta}$ from Eq. (10), we find

$$\hat{\boldsymbol{q}}_{\omega,\beta} = [-i\omega I - L(\bar{\boldsymbol{q}};\beta)]^{-1}\hat{\boldsymbol{f}}_{\omega,\beta} = H(\bar{\boldsymbol{q}};\omega,\beta)\hat{\boldsymbol{f}}_{\omega,\beta}, \tag{11}$$

where $H(\bar{\boldsymbol{q}};\omega,\beta) = [-i\omega I - L(\bar{\boldsymbol{q}},\beta)]^{-1}$ is referred to as the *resolvent operator*. Here, $H(\bar{\boldsymbol{q}};\omega,\beta)$ is the transfer function between the input $\hat{\boldsymbol{f}}_{\omega,\beta}$ and the output $\hat{\boldsymbol{q}}_{\omega,\beta}$ for the given base state $\bar{\boldsymbol{q}}(x,y)$, real-valued spanwise wavenumber β and real-valued frequency ω (Aström and Murray, 2010). The selection of the base state is important as discussed below.

For a stable base state, the resolvent analysis can be cast in the framework of singular value decomposition (SVD) of the resolvent operator to determine the dominant forcing directions $\hat{\boldsymbol{f}}_{\omega,\beta}$ and the output directions $\hat{\boldsymbol{q}}_{\omega,\beta}$. Using the matrix notation, we can express the decomposition as

$$H(\bar{\boldsymbol{q}};\omega,\beta) = \mathcal{Q}\Sigma\mathcal{F}^*, \tag{12}$$

where $H \in \mathbb{C}^{5m\times 5m}$, $\mathcal{Q} = [\hat{\boldsymbol{q}}_1, \hat{\boldsymbol{q}}_2, \ldots, \hat{\boldsymbol{q}}_k]$ contains a set of left singular vectors $\hat{\boldsymbol{q}}_j$ called the *response modes*, and $\mathcal{F} = [\hat{\boldsymbol{f}}_1, \hat{\boldsymbol{f}}_2, \ldots, \hat{\boldsymbol{f}}_k]$ holds a set of right singular vectors $\hat{\boldsymbol{f}}_j$ called the

forcing modes with the superscript $*$ representing the Hermitian transpose. Amplification ratio of response and forcing modes are given by the corresponding singular values $\Sigma = \mathrm{diag}(\sigma_1, \sigma_2, \ldots, \sigma_k)$ in descending order, where the leading amplification σ_1 is referred to as the *resolvent gain*. Alternatively Eq. (12) can be viewed as $\mathcal{Q}\Sigma = H\mathcal{F}$, where the resolvent operator maps the unit vector $\hat{\boldsymbol{f}}_j$ to the unit vector $\hat{\boldsymbol{q}}_j$ with the gain σ_j.

The resolvent gain is studied in the context of having a compressible flow energy norm (Chu, 1965) defined by

$$E = \int_S \left[\frac{\bar{a}^2 \rho^2}{\gamma \bar{\rho}} + \bar{\rho}(u^2 + v^2 + w^2) + \frac{\bar{\rho} C_v T^2}{\bar{T}} \right] \mathrm{d}s, \tag{13}$$

which yields

$$W_e^{\frac{1}{2}} H(\bar{q}; \omega, \beta) W_e^{-\frac{1}{2}} = Q \Sigma F^*, \tag{14}$$

where W_e is the weight matrix based on the compressible energy weight above and S is the area of analysis. This norm can be related to the induced 2-norm of the resolvent operator $H(\bar{\boldsymbol{q}}; \omega, \beta)$ through a weight matrix W, such that $||\hat{\boldsymbol{q}}||_E^2 = ||W\hat{\boldsymbol{q}}||_2^2$ (Schmid and Henningson, 2001; Yeh and Taira, 2019). The weight matrix W can be constructed based on the discretization scheme adopted in the numerical configuration. Consequently, the optimal ratio of this energy norm of response to forcing modes can be obtained via calculating the largest singular value of the resolvent operator, which is the induced 2-norm of the weighted resolvent matrix $WH(\bar{\boldsymbol{q}}; \omega, \beta)W^{-1}$. Because of the weight matrix W used in the induced 2-norm evaluation, the resulting forcing and response modes shown later have been scaled by W^{-1} to represent the correct flow field.

In discounted resolvent analysis (Jovanović, 2004) for an unstable flow, an exponential discount is introduced to the dynamical system, in which energy amplification within a finite-time window can be examined. The finite-time window is realized by introducing a real-valued parameter α into the original resolvent operator (Eq. (11)) to form the

discounted resolvent operator

$$H^{\alpha}(\bar{\boldsymbol{q}};\omega,\beta) = [-i(\omega + \mathrm{i}\alpha)I - L(\bar{\boldsymbol{q}};\beta)]^{-1} = [-i\omega I - L(\bar{\boldsymbol{q}};\beta) + \alpha I]^{-1}. \tag{15}$$

The eigenspectrum of maxtrix $[L(\bar{\boldsymbol{q}};\beta) - \alpha I]$ is equivalent to the eigenspectrum of $L(\bar{\boldsymbol{q}};\beta)$ shifted by $-\alpha$ along imaginary axis. In other words, the flow response under investigation is in a finite-time window characterized by $1/\alpha$. As $\alpha \to 0^+$, the window becomes infinite such that Eq. (15) reduces to the original resolvent operator in Eq. (11). For an unstable flow with $\max(\tilde{\omega}_i) > 0$, by choosing $\alpha > \max(\tilde{\omega}_i)$, we select to examine the harmonic response of the flow prior to the instabilities invalidating the formulation. It is important to note that the actual flow will not grow unboundedly. Nonlinearity will act to saturate the disturbance level, and its magnitude will stay bounded. In many cases, including flow control applications, the resolvent analysis is hoped to provide the dominant amplification that likely is going to trigger nonlinear effects to shift the mean flow to a desirable state for achieving some engineering benefits.

2.3.2 Multi-input/multi-output system

A MIMO model is devised to describe the relationship between the m unsteady surface pressure inputs and the output (u, v) velocity at n measurement locations (Bendat and Piersol, 2011). Fig. 5 illustrates a multi-input/single-output (MISO) model. A MIMO model is simply a MISO model for each velocity component at each measurement location.

It should be noted that the model is linear and approximates the nonlinear flow system. The velocity at each measurement location of interest is a sum of the contributions from all sensors and noise that is unique to each output and uncorrelated with the inputs.

By performing a Fourier transform, the time-domain model is transformed to the frequency domain (denoted by capital letters)

$$Y = HX + N, \tag{16}$$

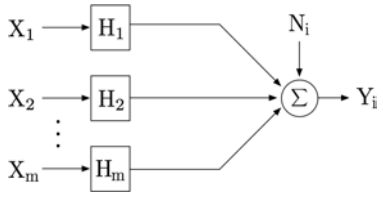

Figure 5: Schematic of a MISO system. A similar model is constructed at each output measurement location to produce a MIMO model.

where $X \in \mathbb{C}(m \times 1)$, $H \in \mathbb{C}(2n \times m)$, and both Y and $N \in \mathbb{C}(2n \times 1)$. Explicit frequency dependence in Eq. 16 and below has been suppressed. Note that the inputs are, in general, partially correlated. We wish to determine the optimal H that minimizes the output noise contribution. Solving for H generally requires TR pressure and velocity data. Unfortunately, TR velocity is not available in a conventional PIV system due to the low sampling frequency.

Right multiplying Eq. 16 by the complex conjugate transpose X' and taking $\frac{2}{T}E[\cdot]$, where $E[\cdot]$ denotes the expectation operator, yields

$$G_{xy} = HG_{x_i x_j}, \tag{17}$$

where $G_{xy} \in \mathbb{C}(2n \times m)$ is the cross spectral density matrix between pressure and velocity, and $G_{x_i x_j} \in \mathbb{C}(m \times m)$ is the Hermitian cross spectral density matrix of pressure, and whose diagonal elements are the autospectral density of the inputs. In general, $G_{x_i x_j}$ is full rank, enabling matrix inversion of Eq. 17 to solve for H at each frequency of interest. However, the equation above still cannot be calculated directly without TR velocity. Therefore, an alternative approach uses

$$G_{xy}(f) = \int_{-\infty}^{+\infty} R_{xy}(\tau) e^{-j2\pi f\tau} d\tau, \tag{18}$$

where R_{xy} is the cross-correlation matrix between pressure fluctuations, x, and velocity fluctuations, y, which can be calculated from the TR pressure data and the non-time-resolved (NTR) velocity by systematically shifting the time delay between pressure and

velocity snapshots. It should be noted that this methodology is equivalent to that employed in the Spectral LSE proposed by Tinney et al. (2006), but our implementation is explained below for clarity and completeness.

For stationary data, the cross-correlation R_{xy} is defined as

$$R_{xy}(\tau) = E[x(t)y(t+\tau)]. \tag{19}$$

However,

$$R_{xy}(\tau) = R_{yx}(-\tau) = E[y(t)x(t-\tau)]. \tag{20}$$

The last term in Eq. 20 is used to compute the cross correlation between velocity y and pressure x by sequentially shifting the pressure signal with respect to the PIV snapshots and averaging over all snapshots. Then the single-sided cross-spectral density is calculated via a Discrete Fourier Transform of $R_{xy}(\tau)$

$$\begin{aligned} G_{xy}\left(f_j\right) &= c\Delta t \sum_{k=1}^{N_{FFT}} w(k) R_{xy}\left(k\right) e^{-i\frac{2\pi(j-1)\left(k-1-\frac{N_{FFT}}{2}\right)}{N_{FFT}}}; \\ j &= 1 : N_{FFT}/2+1, \end{aligned} \tag{21}$$

where $f_j = (j-1)f_s/N_{FFT}$, w is a window function, $c = 1$ for $j = 1$ and $c = 2$ for $j \geq 2$, and $R_{xy}\left(k\right) = R_{xy}\left(-N_{FFT}\Delta t/2 + (k-1)\,\Delta t\right)$. By factoring and simplifying the phase term,

$$e^{-i\frac{2\pi(j-1)(-N_{FFT}/2)}{N_{FFT}}} = e^{i\pi(j-1)}, \tag{22}$$

we leverage the Fast Fourier Transform (when N_{FFT} is a power of 2), so that

$$G_{xy}\left(f_j\right) = c\Delta t e^{i\pi(j-1)}\, FFT(w \cdot R_{xy}, N_{FFT}). \tag{23}$$

After obtaining G_{xy} and G_{xx}, H is determined using Eq. 17.

Note that the POD eigenvectors Φ and eigenvalues Λ can be obtained via solution of the $2n \times 2n$ eigenvalue problem

$$\frac{YY'}{K}\frac{I_{2n}}{2n}\Phi = \Phi\Lambda, \tag{24}$$

where $I_{2n}/(2n)$ is a normalized area weight factor $= dA/A$ used to enable the comparison between different 2C2D PIV grids of aggregate size n, and I_{2n} is the $2n \times 2n$ identity matrix. This eigenvalue problem is large and intractable for PIV data on current desktop computers. As described in Schmidt and Colonius (2020a), the eigenvectors Φ are linear combinations of the velocity snapshots Y, leading to the (typically) smaller $K \times K$ eigenvalue problem via the method of snapshots, where K is the number of blocks (Sirovich, 1987)

$$\frac{Y'Y}{2nK}\Psi = \Psi\Lambda, \quad \Phi = Y\Psi, \tag{25}$$

where the modes Φ are normalized by their 2-norm such that $\Phi'\Phi/(2n) = I$. This approach is denoted as "SAMM-SPOD" because it uses the SPOD algorithm of Towne et al. (2018) as follows. After H is determined from Eq. 17, Eq. 16 is used to generate the estimated data matrix $\hat{Y} = HX$ (ignoring the noise term) from the FFT of the windowed and, if applicable, overlapped time-resolved pressure data records X. The details of this implementation are described in Zhang et al. (2019). It should be noted that acquiring the pressure data as long continuous records offers the possibility of overlapping in the construction of the data matrix. In the follow section, we introduce a simpler way to estimate the dominant POD modes and eigenvalues.

2.3.3 Conditional Spectral Analysis

The conditional spectral analysis herein is adapted from Bendat and Piersol (2011). The objective of the analysis is to determine the relationship between *unknown* independent inputs W and the outputs, Y, as depicted in Fig. 6. Right multiplying Eq. 16 by the complex conjugate transpose Y' and taking $\frac{2}{T}E[\cdot]$ of both sides yields the cross spectral density matrix of the velocity

$$G_{y_i y_j} = HG_{yx} + G_{nn}, \tag{26}$$

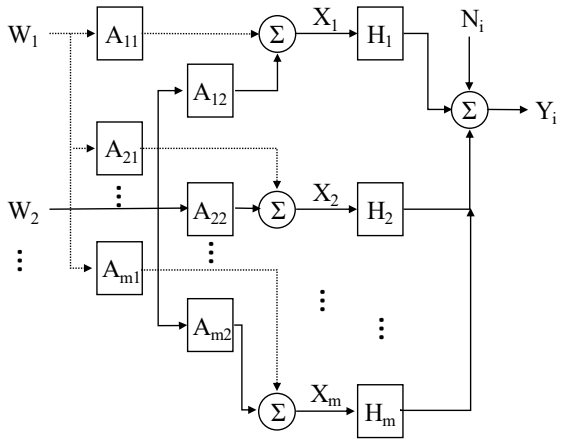

Figure 6: Schematic of a MIMO system in the frequency domain shown with two independent inputs.

where the first term on the right-hand side represents the model output, $\hat{G}_{y_i y_j}$, and the second term is an unknown diagonal matrix representing the noise. From Eq. 17 and noting that $G_{xy} = G'_{yx}$, the model output can be expressed as

$$\hat{G}_{y_i y_j} = H G'_{x_i x_j} H'. \tag{27}$$

Eq. 27 provides a way to compute the estimated cross-spectral density of the velocity field.

As noted earlier, the pressure inputs X are partially coherent and therefore not independent. Now assuming X is a linear combination of $r \leq m$ independent inputs W via a transfer matrix $A \in \mathbb{C}(m \times m)$ as shown in Fig. 6, then

$$X = AW. \tag{28}$$

Right multiplying this equation by X' and taking $\frac{2}{T}E[\cdot]$ yields

$$\frac{2}{T}E[XX'] = \frac{2}{T}E[AW(AW)'] = A\frac{2}{T}E[WW']A', \tag{29}$$

or

$$G_{x_i x_j} = A G_{ww} A'. \tag{30}$$

Therefore, a sorted eigendecomposition of the *small* $m \times m$ Hermitian input cross-spectral density matrix yields A and the autospectral density of the independent sources W in descending order of the eigenvalues and corresponding eigenmodes. Substituting Eq. 30 into Eq. 27 yields

$$\underbrace{\hat{G}_{y_i y_j}}_{2n\times 2n} = \underbrace{H}_{2n\times m}\underbrace{A}_{m\times m}\underbrace{G_{ww}}_{m\times m}\underbrace{A'}_{m\times m}\underbrace{H'}_{m\times 2n} \tag{31}$$

or

$$\hat{G}_{y_i y_j} = H_{yw} G_{ww} H'_{yw}, \tag{32}$$

which is the desired reduced-rank approximation of the cross spectral density matrix of the velocity field, denoted as "SAMM-RR". Note that $H_{yw} = HA$ is the estimated frequency response function between the model output velocity $\hat{Y}$ and independent inputs W and effectively provides the response modes of a resolvent analysis (Taira et al., 2017). Using the same scaling as in Eq. (24) yields

$$\hat{G}_{y_i y_j} = \overline{H}_{yw} \overline{G}_{ww} \overline{H'}_{yw}, \tag{33}$$

where $\overline{H}_{yw} = \frac{\sqrt{2n} H_{yw}}{|H_{yw}|}$ and $\overline{G}_{ww} = \frac{G_{ww}}{2n} \parallel H_{yw} \parallel^2$. Column j of $\overline{H}_{yw}$ is the estimated POD mode j. SAMM-RR is a computationally "simple" way to extract the spatiotemporal coherent structures of the velocity fields associated with particular frequencies. We emphasize that the approaches presented are achieved without TR-PIV. Therefore, the noise term, G_{nn}, of Eq. 26 cannot be computed, and so the multiple coherence function normally used to assess model adequacy cannot be evaluated. The SAMM-RR algorithm for calculating the velocity modes is illustrated in Fig. 7 and described as follows

1. Non-dimensionalize the NTR velocity fluctuations and TR surface pressure fluctuations by freestream velocity fluctuation vector $y = \frac{\vec{u'}}{U_\infty}$ and dynamic pressure $x = \frac{p'}{0.5\rho {U_\infty}^2}$.

2. Calculate the input cross spectral density matrix $G_{x_i x_j}$.

3. Perform a sorted eigendecomposition of $G_{x_i x_j}$ to obtain the eigenvectors A and eigenvalues G_{ww} at each frequency.

4. Calculate the cross-correlation of x and y as $R_{x_i y}$ for each velocity component at each PIV grid point using Eq. 20.

5. Calculate the cross-spectra matrix $G_{x_i y}$ using Eq. 21 with the same frequency resolution and window function as in step 2.

6. Calculate H using Eq. 17 for the specified frequencies of interest.

7. Calculate the transfer function H_{yw} using Eq. 32 for the specified frequencies of interest, and then use Eq. 33 for re-scaling. The columns of $\overline{H}_{yw}$ are the low-rank approximation of the spectral POD velocity modes, and $\overline{G}_{ww}$ is the independent source autospectral density matrix .

The application of the above methods to flow-induced cavity oscillations is discussed in the next section. We compare the non-TR SAMMs presented above to the results from independent TR-PIV measurements.

3 Results

In this section we will highlight the major results to come out of this effort. This will start with a discussion on the effects of finite span cavities. This is followed by an examination of various applications of the Proper Orthogonal Decompositon to high speed cavity flow and that of the newly developed SAMM method. The data from Large Eddy Simulations is examined by an application of Resolvent Analysis and that output is used to study space-time actuation at the cavities leading edge for the reduction of the fluctuating surface pressure within the cavity. Finally we present results from experiments demonstrating the similarities in the flow control mechanisms for passive tabs to the that slot blowing.

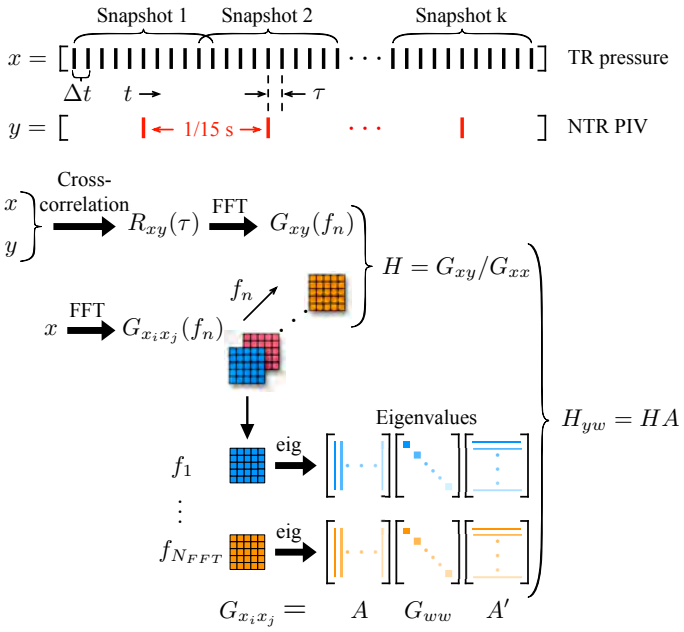

Figure 7: The "SAMM-RR" algorithm.

3.1 Baseline Flow

We discuss sidewall effects on the baseline flows, then examine the underlying mechanism of flow control. The compressibility effects are also investigated for the subsonic ($M_\infty = 0.6$) and supersonic ($M_\infty = 1.4$) cavity flows.

We first describe the flows at $M_\infty = 0.6$ for spanwise-periodic versus finite-span cavities. Representative visualizations of the flow fields are shown in figure 8. We use iso-surfaces of the Q-criterion (Hunt et al., 1988) to identify vortical structures and color them with instantaneous pressure coefficient C_p, which reveal intense pressure fluctuations in the baseline flows.

In the spanwise-periodic baseline flow shown in figure 8 (left), the shear layer rolls up into large spanwise aligned vortices after the flow passes over the leading edge and convects downstream. Smaller-scale turbulent vortical structures appear around the primary spanwise vortices. As these vortices advect downstream, the large structures lose coherence around $x/D \approx 4$. Large pressure fluctuations are prominent in two regions: one is in the

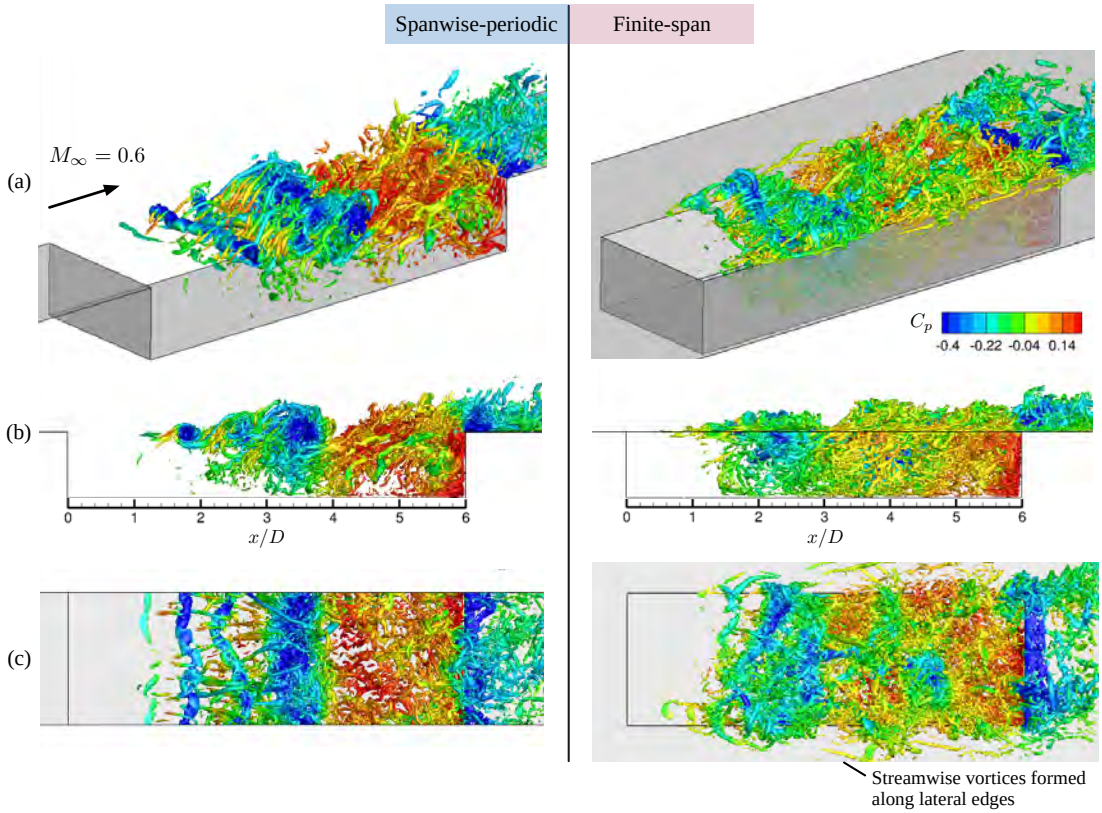

Figure 8: Iso-surfaces of instantaneous $Q(D/u_\infty)^2 = 14$ colored by $C_p = (p - p_\infty)/(\frac{1}{2}\rho_\infty u_\infty^2)$ from the baseline flow fields at $M_\infty = 0.6$. (a) Perspective, (b) side, and (c) top views of the spanwise-periodic and finite-span cavity flows.

shear-layer region ($1 \lesssim x/D \lesssim 4$) where the intense fluctuations are carried by the spanwise coherent vortex, and the other one is near the cavity trailing edge where the large-scale vortical structures impinge on the aft wall.

For the finite-span cavity flow shown in figure 8 (right), the spanwise coherent vortices roll up near the cavity leading edge, similar to that observed for the spanwise-periodic case. However, the sidewall edges bend these large spanwise vortices near the sidewalls and instigate the breakdown of the large coherent structures earlier. Investigation of numerous instantaneous snapshots indicate that the large vortical structures rarely appear after $x/D \approx 3$ compared to the spanwise-periodic case. Moreover, the presence of the sidewalls results in the formation of streamwise vortices that spread out away from the cavity. We also observe a reduction in instantaneous pressure fluctuations in the shear-layer region and on the aft wall of the finite-span cavity flow compared to the spanwise-periodic case. Detailed discussion on root-mean-square (rms) pressure is provided later to illustrate these reductions in the finite-span case.

For cavity flows at $M_\infty = 1.4$, compressibility plays a larger role in affecting the flow characteristics. As shown in figure 9 (left) for $M_\infty = 1.4$, large density gradient magnitudes $||\nabla\rho||$ are captured above the cavity indicating strong compression waves as seen in figure 9 (b). These waves are generated due to either the obstructions caused by the spanwise vortex roll-up in the shear layer or their impingement on the aft wall. Due to the emission of these compression waves, the normalized pressure fluctuations above the trailing edge become more intense than in the case of the subsonic flows. This is depicted from the rms pressure discussion presented later.

For the finite-span cavity flow at $M_\infty = 1.4$, the development of spanwise coherent structures is hindered because of the sidewalls, and streamwise vortical structures are formed from the lateral edges, in a manner similar to those observed from the subsonic cases. It is noteworthy that once the shear-layer roll-ups are weakened, the source of the compres-

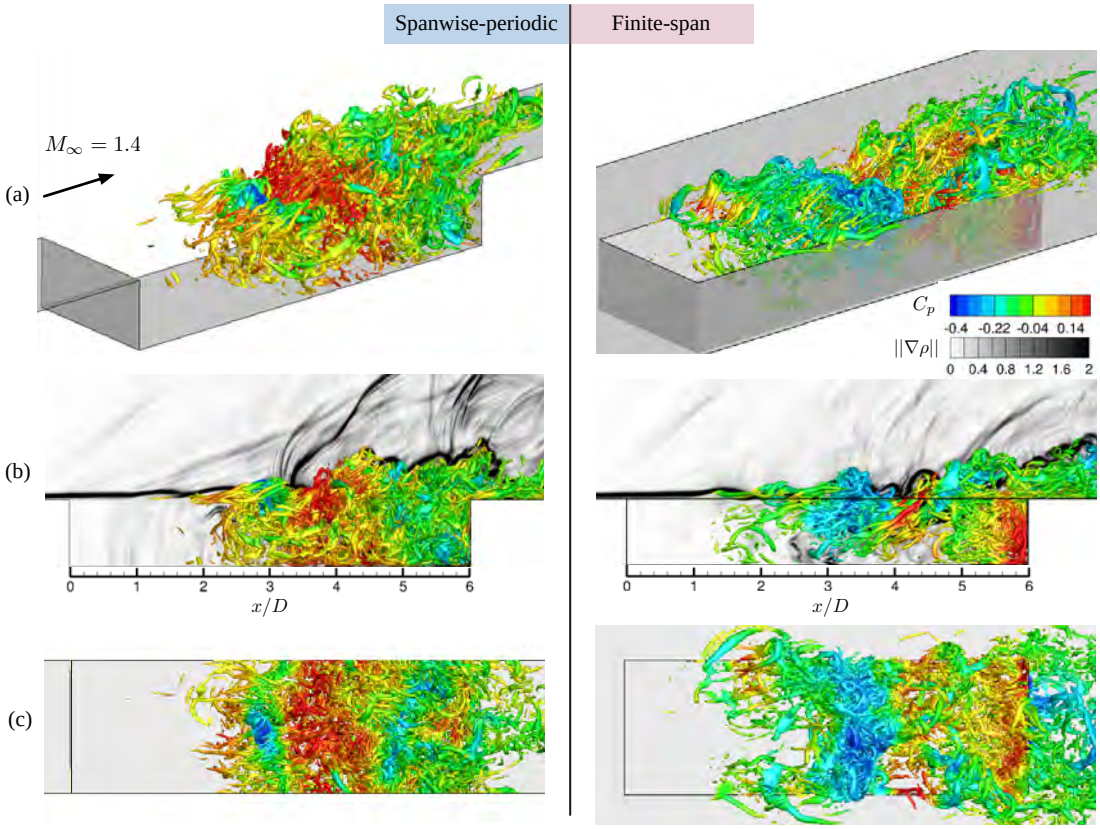

Figure 9: Iso-surfaces of instantaneous $Q(D/u_\infty)^2 = 14$ colored by $C_p = (p - p_\infty)/(\frac{1}{2}\rho_\infty u_\infty^2)$ from the baseline flow fields at $M_\infty = 1.4$. (a) Perspective, (b) side, and (c) top views of the spanwise-periodic and finite-span cavity flows. The contours of density gradient magnitude $||\nabla\rho||$ on the midspan ($z/D = 0$) are shown in the side views.

sion waves in the shear-layer region is diminished. Hence, the density gradient magnitudes above the cavity in the finite-span cavity flow are lower than those in the spanwise-periodic cavity flow as shown in figure 9 (b). The discussion on rms pressure presented later further supports this observation.

A global view of the normalized rms pressure is shown in figure 10. It is noted that all the reported pressure quantities are normalized by dynamic pressure ($\frac{1}{2}\rho_\infty u_\infty^2$). For the finite-span cases, the midspan ($z/D = 0$) is selected as a reference location, since the fluctuations are most intense along the midspan in the base flows. For both $M_\infty = 0.6$ and 1.4 cases, large values of rms pressure are observed mainly in the shear-layer region and near the trailing edge. However, since the sidewalls of the finite-span cavities hinder the development of spanwise roll-ups, the maximum rms pressure in the shear layer is reduced by 9% and 30% for $M_\infty = 0.6$ and 1.4, respectively, compared to the spanwise-periodic cases. Moreover, the regions of large pressure fluctuations $p_{\text{rms}}/(\frac{1}{2}\rho_\infty u_\infty^2) > 0.2$ in the shear layer verify that the shear-layer roll-ups are weakened in the finite-span cases compared to that of the spanwise-periodic ones. We also integrate the rms pressure on the aft wall, denoted as $\widetilde{p}_{\text{rms}}$, and list their values in table 2. In the baseline flows, $\widetilde{p}_{\text{rms}}$ in the finite-span cases are smaller than those in the spanwise-periodic cases by 30% and 21% for $M_\infty = 0.6$ and 1.4, respectively, indicating a reduced strength of the flow impingement on the aft wall.

In addition to the large rms pressure in the shear layer and on the aft wall, pressure fluctuations are intense in the region above the trailing edge at $M_\infty = 1.4$ in the spanwise-periodic cases, because of the compression waves generated around the trailing edge in the supersonic flow. However, these wave-induced fluctuations decrease in the finite-span cavity flow due to the lack of presence of spanwise coherent structures as revealed from the instantaneous flow fields such as that shown in figure 9 (b). With an increase in Mach number from $M_\infty = 0.6$ to 1.4 for both spanwise-periodic and finite-span cases, we further

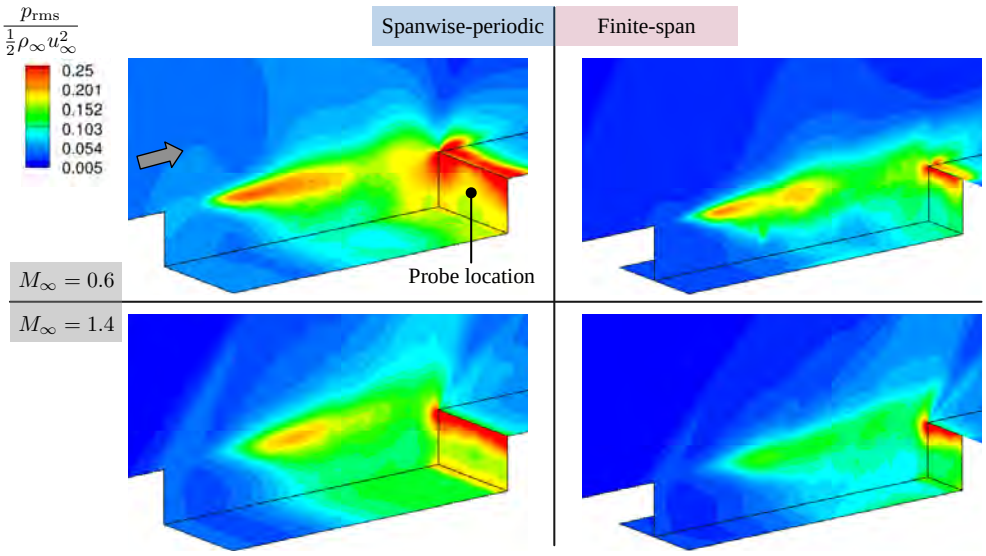

Figure 10: Normalized pressure fluctuations $p_{\mathrm{rms}}/(\frac{1}{2}\rho_\infty u_\infty^2)$ of baselines for the spanwise-periodic and finite-span cavity flows at $M_\infty = 0.6$ and 1.4. For finite-span cases, the midspan ($z/D = 0$) is selected as a reference location for visualization. Pressure time series are collected from the probe at $[x, y, z]/D = [6, -0.5, 0]$ as illustrated in the plot.

M_∞	Spanwise B.C.	$\widetilde{p}_{\mathrm{rms}}$		Reduction
		Baseline	Controlled	
0.6	Spanwise-periodic	0.401	0.228	-43.1%
	Finite-span	0.281	0.213	-24.2%
1.4	Spanwise-periodic	0.383	0.314	-18.0%
	Finite-span	0.305	0.277	-9.2%

Table 2: Integrated pressure fluctuations $\widetilde{p}_{\mathrm{rms}} = \int_{S_{\mathrm{aft\ wall}}} (p_{\mathrm{rms}}/\frac{1}{2}\rho_\infty u_\infty^2) dS$ on the aft wall in all the cases considered. The reduction is evaluated as $(\widetilde{p}_{\mathrm{rms,\ controlled}} - \widetilde{p}_{\mathrm{rms,\ baseline}})/\widetilde{p}_{\mathrm{rms,\ baseline}} \times 100\%$.

notice a stabilizing effect due to compressibility (Sun et al., 2017b) that the roll-up of the shear layer is delayed. The maximum normalized rms pressure is reduced and its location moves farther downstream in the supersonic case. This stabilizing effect of compressibility has also been observed in the experimental work by (Beresh et al., 2016).

3.2 POD Approaches

The datasets being analyzed in this section have been obtained for an open cavity in Sandia National Laboratories' Trisonic Wind Tunnel facility and were detailed by Beresh et al. (2017). The datasets are of a rectangular cavity of dimensions 127 mm in length, 127 mm in width and 25.4 mm in depth ($L/D = 5, L/W = 1, W/D = 5$). The cavity is installed in the lower wall of the tunnel and had an approaching boundary layer thickness of 10-15 mm for range of Mach numbers tested. The test was conducted for three freestream Mach numbers of 0.6, 0.8 and 0.94 with associated freestream velocities of 215, 280 and 315 m/s respectively. The freestream dynamic pressure was kept at a constant value of 33 kPa.

The experiment performed was pulse-burst PIV (refer to Beresh et al. (2015) for details on pulse-burst PIV imaging technique), which helped obtain two-dimensional time-resolved velocity measurements in a region encompassing the cavity shear layer along the centerline plane. Pulse-burst PIV imaging used pulse-burst lasers that generated a burst lasting 10.2 ms once every 8 s, allowing the capture of 386 snapshots per burst at a sampling rate of 37.5 kHz. Between 250 and 300 such records were collected for each tested Mach number. The images were collected using two CMOS cameras placed side-by-side to extend the view in the streamwise direction giving a combined field of view of 118 by 31 mm^2. Processing of the images was done using LaVision's DaVis v8.2. The image pairs were background corrected, intensity normalized and then interrogated with interrogation windows of size 64×64 pixels for the initial pass and 24×24 pixels for 2 subsequent passes with a 50 %

overlap. This resulted in a spatial resolution of 1 by 1 mm^2 for each vector. The vector fields were then validated using signal-to-noise ratio, nearest-neighbor comparisons, and an allowable velocity range. In addition to the PIV data, synchronous measurements using a high-frequency pressure sensor (Kulite XCQ-062-50A) was mounted on the cavity aft wall at $y = -10.7$ mm along the centerspan which measured pressure fluctuations at a sampling rate of 125 kHz.

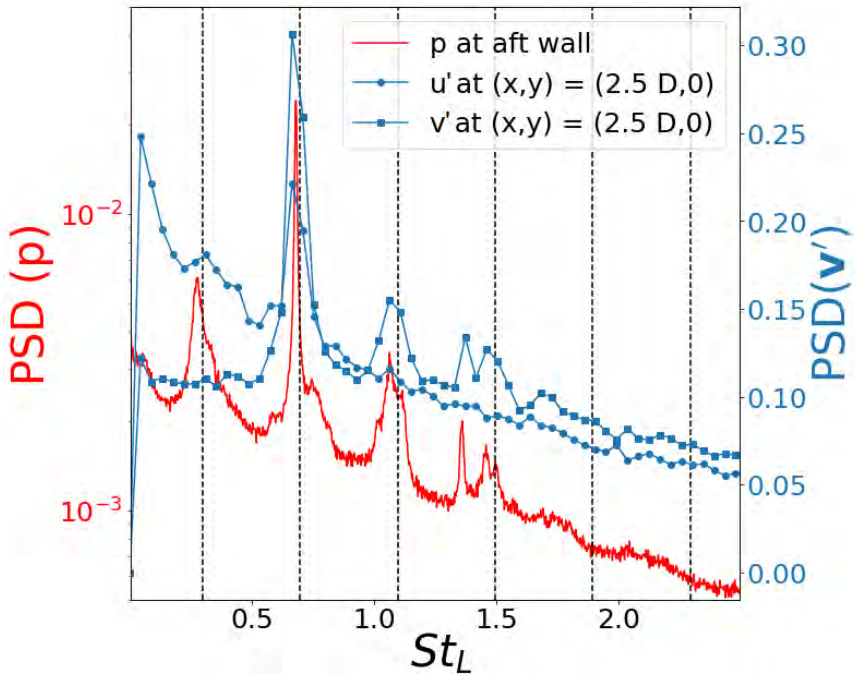

Figure 11: PSD of aft wall pressure fluctuations overlaid with PSD of stream-wise and wall-normal velocity fluctuations at (x,y) = (2.5D,0) for Mach 0.8 flow

First, comparisons will be made between POD modes obtained using the snapshot POD application and the space-time POD application when applied to Mach 0.8 datasets. Some details about these datasets are being mentioned here. The PSD plots for pressure and velocity fluctuations for Mach 0.8 data can be seen in Figure 11. The PSD values for pressure and velocity fluctuations for this figure and subsequent PSD plots in this section are calculated using eq 34 and 35 respectively.

$$PSD(p) = \frac{\sqrt{< \hat{p}(f)\hat{p}^*(f) > \Delta f}}{Q_\infty} \tag{34}$$

and velocity fluctuation spectra are calculated from,

$$PSD(\mathbf{v}^{'}) = \frac{\sqrt{< \hat{\mathbf{v}}'(f)\hat{\mathbf{v}}'^*(f) > \Delta f}}{\sqrt{< \mathbf{v}^{'2} >}}, \tag{35}$$

where, <> implies ensemble averaging. These PSD values were calculated using Bartlett's method (Bartlett, 1948, 1950) by averaging the PSD values over all runs. The dashed lines in the figure represents the Rossiter frequency predictions.

Pressure and velocity fluctuations in the figure are plotted in separate axes with scaling to ease comparisons in the spectra. The resulting frequency resolution for pressure and velocity fluctuation PSD is 5 and 97.56 Hz respectively. Peaks are observed at the first 4 Rossiter frequencies with the highest peak observed for Rossiter frequency 2. This is consistent with pressure PSD peaks observed in Murray et al. (2009).

The mean and wall-normal rms contour plots for Mach 0.8 data can be seen in Figure 12. The plots are consistent with cavity flow literature.

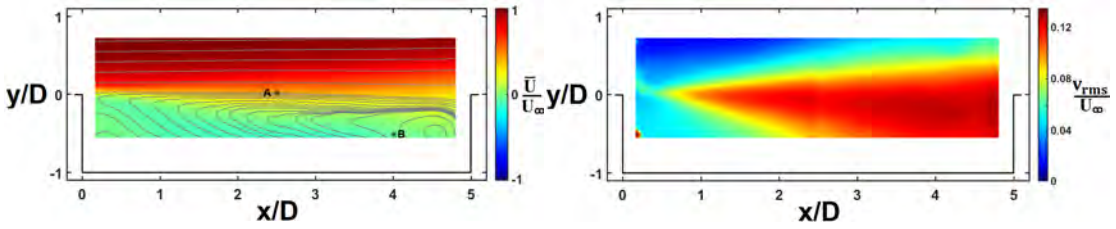

(a) Mean stream-wise velocity (b) Rms wall-normal velocity fluctuations

Figure 12: Mean stream-wise velocity field overlaid with streamlines and Rms wall-normal velocity fluctuation fields for Mach 0.8 flow

First introduced to the turbulence community by Lumley (1967), proper orthogonal decomposition (POD) is now a popular method to extract coherent structures from a complex flow field. As typically applied, the POD technique seeks basis vectors or modes

to maximize the turbulent kinetic energy of a flow field. This effectively reduces to the following eigenvalue problem,

$$\int_T \int_\Omega < u(\mathbf{x},t)u(\mathbf{x}',t') > \Phi(\mathbf{x}',t')d\mathbf{x}'dt' = \lambda^n \Phi^n(\mathbf{x},t). \tag{36}$$

Many times one does not have four-dimensional data (space and time), so often a direction is ignored in the integral of eq. 36. For instance, in the current PIV data, the data is arranged as a function of x, y and t. If time, t is ignored, the above equation results in a spatial eigenvalue problem as,

$$\int_\Omega < u(\mathbf{x})u^*(\mathbf{x}') > \Phi(\mathbf{x}')dx' = \lambda^n \Phi^n(\mathbf{x}). \tag{37}$$

With the advent of highly spatially resolved data from PIV and numerical simulations, the spatial eigenvalue becomes increasingly computationally expensive. Sirovich (1987) developed the snapshot POD which is a computationally efficient approach to solve the spatial eigenvalue problem when resolution in the spatial domain exceeds the number of independent observations or snapshots. The snapshot approach is solved using the following eigenvalue problem,

$$\mu^n a^n(t) = \int_T < u(x,t)u(x,t') > a^n(t')dt'. \tag{38}$$

The spatial eigenvectors can be extracted from flow field and temporal vectors using, $\Phi^n(\mathbf{x}) = \frac{<ua^n>}{<(a^n)^2>}$

Snapshot POD application is based on independent realizations (or snapshots) of flow. It is to be noted here that since the data is time-resolved, successive snapshots may not be independent. Figure 13 makes this clearer where the auto-correlation coefficient for the streamwise and wall-normal components for two representative points in the flow does not go to zero with successive snapshots ($\tau = 0.026ms$) but at a longer time lag ($\tau = 0.45ms$).

For further understanding, snapshot POD is applied to datasets with lag time 0.026 ms and datasets with lag time 0.45 ms.

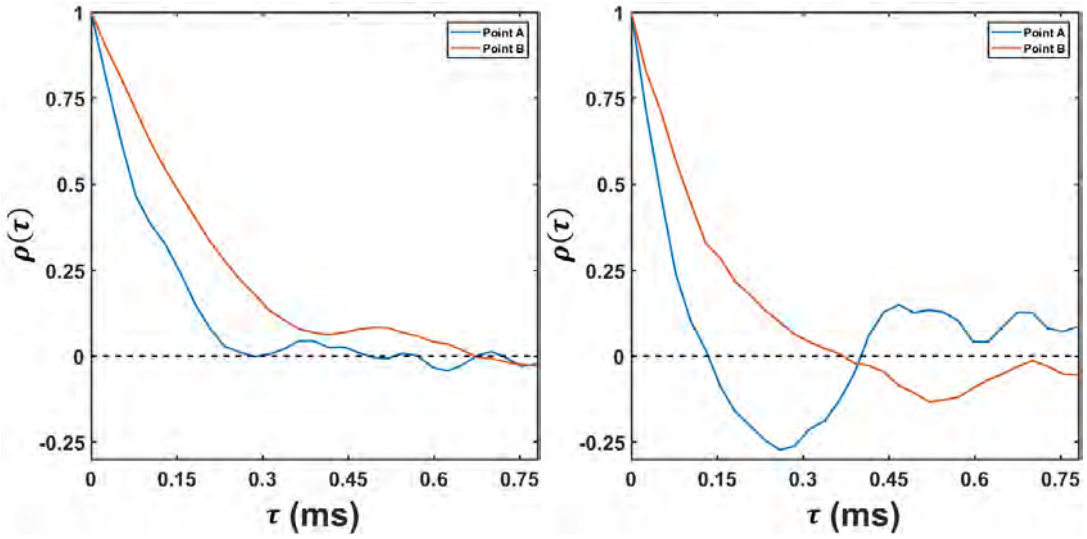

(a) $\rho(\tau)$ in the stream-wise direction (b) $\rho(\tau)$ in the wall-normal direction

Figure 13: Autocorrelation coefficient decay of streamwise and wall-normal velocity fluctuations at two representative points in the cavity shear layer

Since snapshot POD is based on independent realizations, snapshots from multiple runs were stacked to form larger datasets for POD application. Since POD is a stochastic tool it is expected that the properties associated with its modes become invariant or more resolved with the addition of more datasets. Since POD modes are orthonormal vectors, mode invariance can be checked by the spatial inner product which should result to a value of 1. This was tested by calculating inner product between POD modes for multiple sets of snapshots considered, one between 2500 and 3000 snapshots considered. The other between 5000 and 5500 snapshots. The inner product for the first 60 modes is plotted in Figure 14. The colorbar is on an exponential scale to highlight the significance of values closer to unity. For both sets of snapshots taken, the diagonal elements, which represent inner product for the n^{th} mode, are closer to 1 for $\tau = 0.45ms$ than for $\tau = 0.026ms$. This indicates that fewer snapshots are required to get properly resolved eigenvectors when considering independent

snapshots ($\tau = 0.45\,ms$ in this case). This highlights the fact that while it is accepted that turbulence satisfies the ergodic theory, more snapshots are required to obtain fully resolved modes when time-resolved velocity snapshots are used in the formulation of the POD. To get resolved modes from POD, it is better to consider uncorrelated or independent snapshots to reduce the computational expense. This also highlights that the temporal resolution of the data doesn't provide any additional information on the mode structures and instead increases the computational burden as more snapshots are required to get fully resolved snapshot POD modes.

The POD eigenvalues, λ^n, a measure of the weight of a given mode, when applied to flowfield data are analogous to the turbulent kinetic energy of the flow. The convergence of eigenvalues obtained from the snapshot POD application were calculated as,

$$\eta_{conv}(n) = \frac{\sum_{l=1}^{n} \lambda^l}{\sum_{l=1}^{N} \lambda^l}, \tag{39}$$

where, *conv* stands for convergence. The POD eigenvalue convergence plot can be seen in Figure 15. Some observations from the plot is that the fractional energy captured by the first, first 3 and first 7 POD modes are nominally 20%, 35% and 50% respectively. These findings are consistent with Murray et al. (2009) for an open cavity with free-stream Mach number of 0.73 and $L/D = 6$.

Eigenvectors, $\Phi^n(x)$, for the wall-normal velocity component are plotted in Figure 16. Alternating bands of opposite magnitudes are observed with their wavelength decreasing with increasing mode number. This suggests that large scale structures are associated with the leading POD modes which contain higher energy whereas small scale structures are associated with the higher POD modes which contain comparatively less energy. This is consistent with the definition and formulation of snapshot POD where the decomposition is only spatial. These results are also consistent with Murray et al. (2009) for an open cavity ($L/D = 6$) at Mach 0.73. It is interesting to note that, in their work, Murray et al. (2009)

$\tau = 0.026ms$ $\tau = 0.45ms$

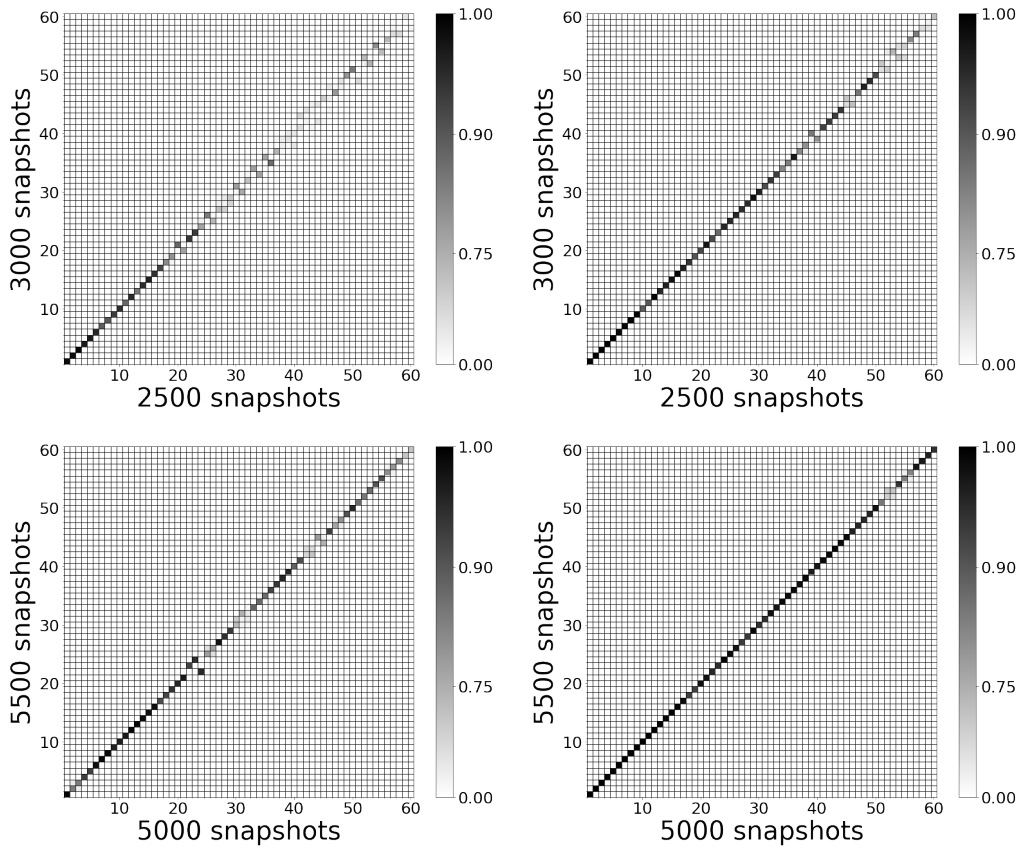

Figure 14: Inner product between POD modes calculated from 2500 and 3000 snapshot datasets for $\tau = 0.026\,ms$ and $\tau = 0.45\,ms$ Inner product between POD modes calculated from 5000 and 5500 snapshot datasets for $\tau = 0.026\,ms$ and $\tau = 0.45\,ms$

.

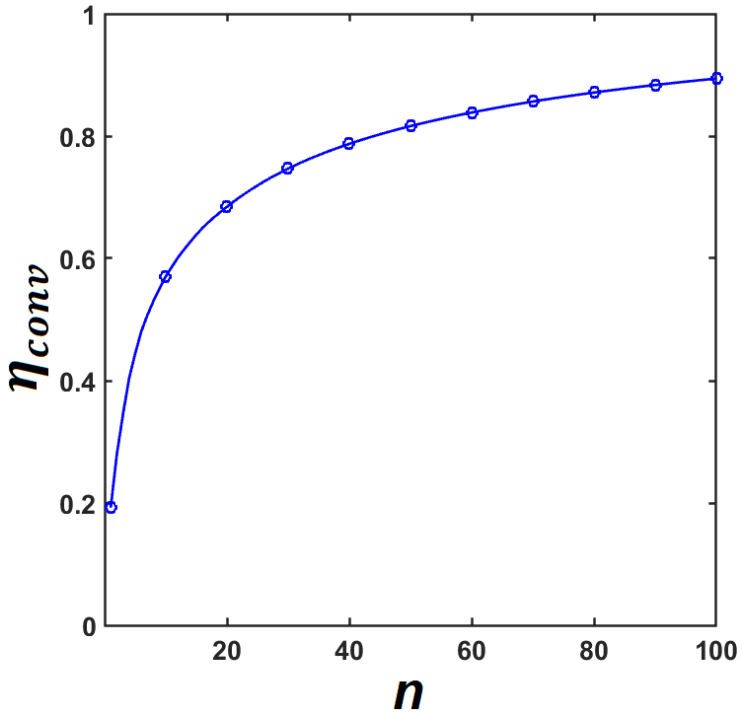

Figure 15: Eigenvalue convergence of snapshot POD modes

noted that the spatial structure of dominant snapshot POD modes was not significantly altered for different free-stream conditions.

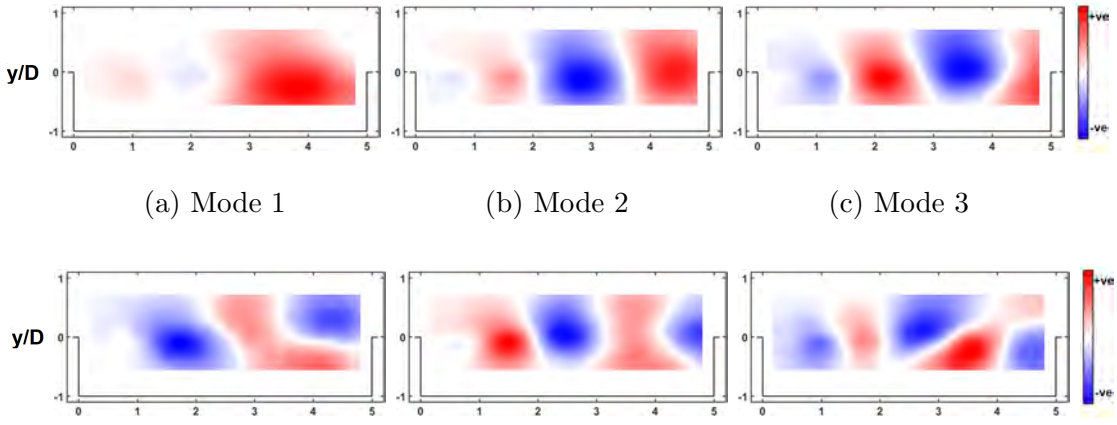

(a) Mode 1 (b) Mode 2 (c) Mode 3

(d) Mode 4 (e) Mode 5 (f) Mode 6

Figure 16: Snapshot POD eigenvectors in the wall-normal direction with increasing mode number

The reduced order representation of the velocity fluctuation field can be calculated using,

$$u(\mathbf{x},t) = \sum_{n=1}^{N} a^n(t)\Phi^n(\mathbf{x}), \tag{40}$$

where the time varying expansion coefficients, $a^n(t)$ can be extracted from the velocity fluctuation field using the following equation,

$$a^n(t) = \int_{\Omega} u(\mathbf{x},t)\Phi^n(\mathbf{x})d\mathbf{x}. \tag{41}$$

Wall-normal rms flow field for these reconstructions have been plotted in Figure 17. This figure shows reconstructions for when first, first 3, first 7 and first 16 POD modes are considered which capture 20%, 35%, 50% and 65% of the total turbulent kinetic energy respectively. It can be seen that as the number of modes included in the reconstruction is increased, the rms plots start to look similar to original flow field (Figure 12((b))). An important observation is that when significantly low number of modes are used, the reconstructions do not reproduce the original flow field and only when sufficient number of modes are captured in the reduced order representation that the reconstruction start to look similar to the original flow field.

In the available PIV data, the data is arranged in x, y and t. The formulation in eq. 36 implies that all spatial directions are non-homogeneous and time direction would be considered non-stationary. For turbulence data, we can invoke stationarity to transform the cross-correlation matrix as, $< u(\mathbf{x},t)u(\mathbf{x}',t') >= C(\mathbf{x},\mathbf{x}',t,t') \rightarrow C(\mathbf{x},\mathbf{x}',t-t') \rightarrow C(\mathbf{x},\mathbf{x}',\tau)$, which can be transformed in the frequency domain through the use of fourier transform as,

$$S(\mathbf{x},\mathbf{x}',f) = \int_{T} C(\mathbf{x},\mathbf{x}',\tau)e^{-i2\pi f\tau}d\tau. \tag{42}$$

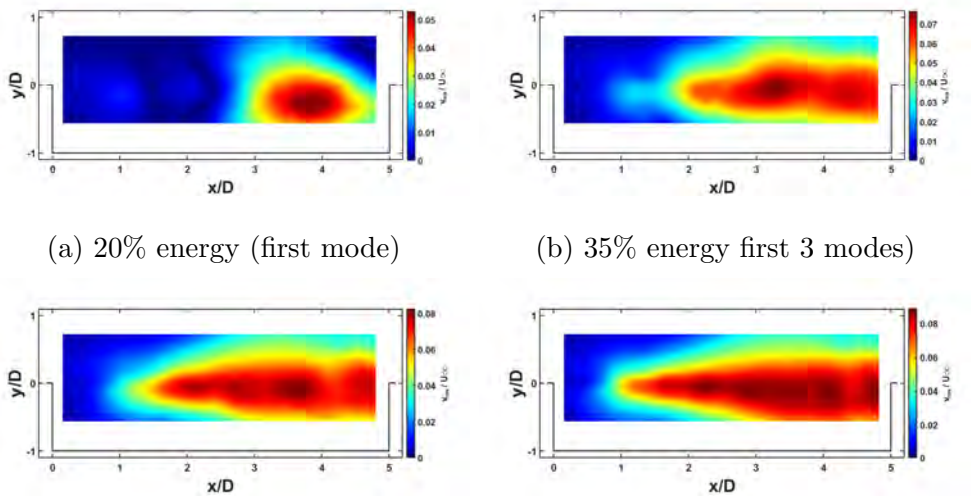

(a) 20% energy (first mode)

(b) 35% energy first 3 modes)

(c) 50% energy (first 7 modes)

(d) 65% energy (first 16 modes)

Figure 17: Reconstructed wall-normal rms velocity fluctuation contours for snapshot POD on including different number of modes constituting increasing energy content

This results in the following form of eigenvalue problem,

$$\lambda^n(f)\Phi^n(\mathbf{x},f) = \int_\Omega < u(\mathbf{x},f)u(\mathbf{x}',f) > \Phi^n(\mathbf{x}',f)d\mathbf{x}'. \tag{43}$$

It has been shown that application of POD in this manner is separable and a discrete version of this equation can be solved independently at each frequency (Glauser and George, 1987). Recently, this formulation of the POD has been reworked in Towne et al. (2018) where they also presented a computationally inexpensive algorithm to apply the snapshot POD in the frequency domain. It must be noted, though, that application of the POD in mixed fourier-spatial domain have been historically performed since Lumley, some of which have been reviewed in Tutkun and George (2017). In the current work, computationally inexpensive algorithm given by Towne et al. (2018) is applied as it resulted in significant speed up in POD application.

Figure 18((a)) shows the eigenvalue spectrum of the first 3 POD which are normalized as,

$$\eta = \frac{\lambda^n(f)}{\sum_{n',f'} \lambda^{n'}(f')}. \tag{44}$$

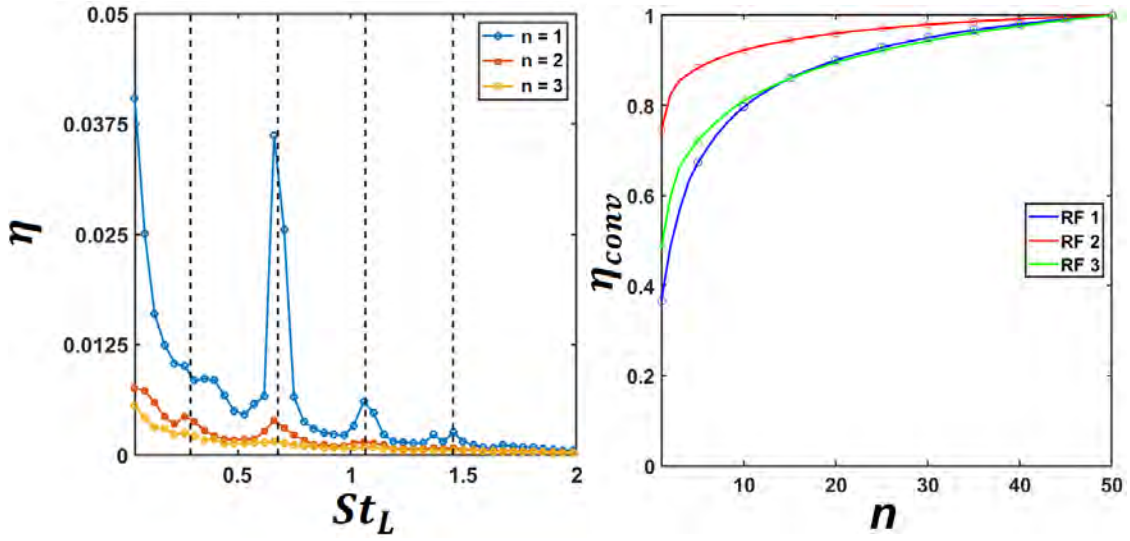

(a) Eigenvalue spectra

(b) Eigenvalue convergence

Figure 18: Eigenvalue spectra of first 3 POD modes and eigenvalue convergence at Rossiter frequencies of space-time POD modes. Rossiter frequency predictions in dashed vertical lines

Significant peaks are observed at Rossiter frequencies with the highest peak at Rossiter frequency 2 suggesting that it dominates the dynamics of the flow in terms of energy. This peak is consistent with the pressure spectra which suggests that shear layer dynamics and pressure fluctuations are related, a clear indication of aero-acoustic feedback phenomena.

Additionally, eigenvalue convergence at specific frequencies can been calculated using,

$$\eta_{conv} = \frac{\sum_{n'=1}^{n} \lambda^{n'}(f)}{\sum_{n'=1}^{N_b} \lambda^{n'}(f)}. \tag{45}$$

Eigenvalue convergence at Rossiter frequencies have been plotted in Figure 18((b)). The plots show that mode convergence happens faster for Rossiter frequency 2, the most dominant frequency for this flow condition. This is followed by Rossiter frequency 3 and 1. The

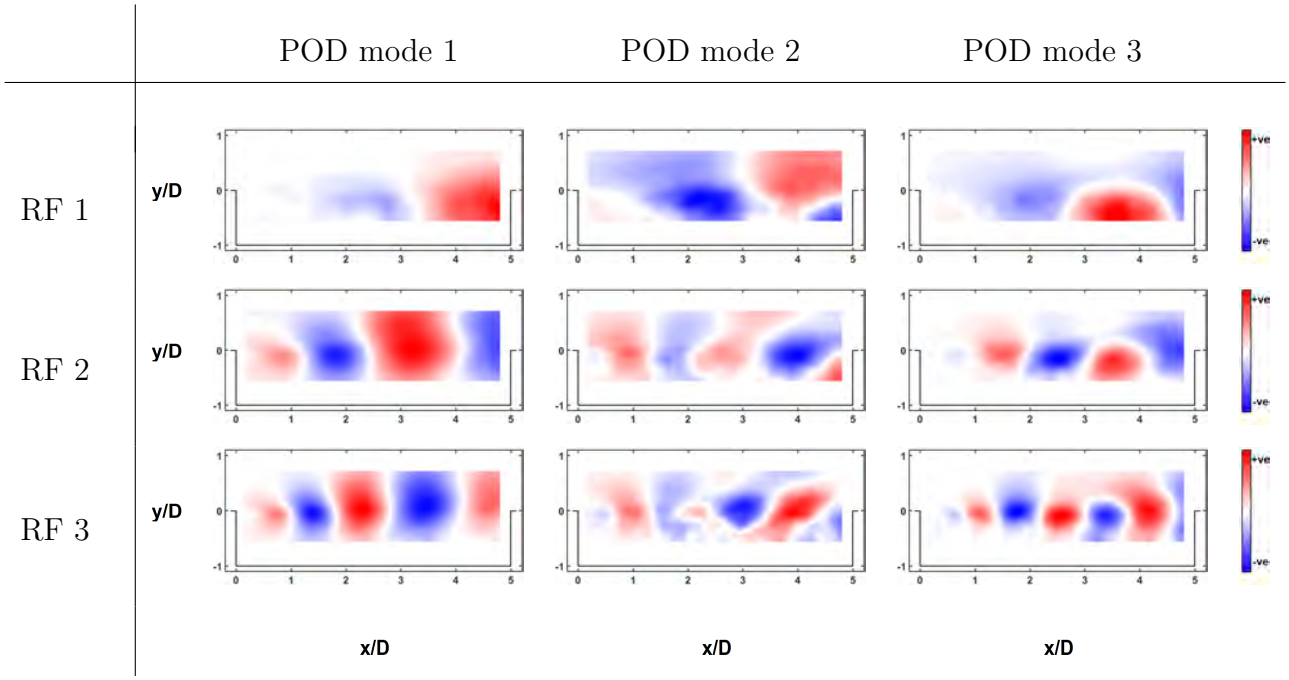

Figure 19: Contour plots depicting wall-normal POD eigenvectors at different POD mode numbers and frequency indices ($real(\Phi_v(\mathbf{x}, f))$

fast convergence (especially at Rossiter frequency 2) signifies existence of a major dominant phenomena at these frequencies which is indicative of cavity resonance phenomena.

The real part of the wall-normal eigenvectors (complex in nature) of the first 3 POD modes for the first 3 Rossiter frequencies can be seen in Figure 19. Alternating bands of opposite magnitudes are observed where wavelength of these bands are related to the frequency (more specifically, St_L). This is consistent with Rossiter's formulation based on wavelengths across the cavity and what has been shown in many studies of the flow structure associated with the different Rossiter (streamwise) modes (**?**).

Velocity reconstructions from space-time POD were calculated by the inverse fourier transform of,

$$u(\mathbf{x}, t) = IFFT(\sum_{f,n} a^n(f)\Phi^n(\mathbf{x}, f)) \tag{46}$$

where f, n represent different frequency - POD mode number pairs to be included for recon-

structions. When these frequency - POD mode pairs are arranged in a purely decreasing energy fashion, this results in modes identified as $\Phi_i^{(n)}$ also termed as 'Big Eddies' in Lumley (1967). Such representation of modes is similar to Aubry et al. (1988); Glauser and George (1987); Ukeiley et al. (2001) where decreasing energy wave number - POD mode pairs were used to construct low-dimensional models. The reconstructions were calculated by increasing the number of modes (POD mode-frequency pairs) for the first 9, first 37, first 146, and first 599 frequency - POD mode pairs which capture about 20 %, 35 %, 50 %, and 65 % of the turbulent kinetic energy respectively and have been plotted in Fig. 20 along with eigenvalue weights in the frequency - POD mode number space. It can be seen that as the number of modes included for reconstructions is increased, the rms velocity fluctuations become closer and closer to the original rms field (see Fig. 12((b))). Also, in contrast to snapshot POD reconstructions, even at very low-dimensional reconstructions, the expanding shear layer structure is well evident for the rms fields of velocity reconstructions.

Several reconstructions have been considered here. Time has been non-dimensionalized as $t^* = tU_\infty/L$ and the start time of all evolutions has been assigned $t^* = 0$. Figure 21 shows time evolution of measured velocity fluctuations (column II in figure) compared with reconstructions obtained by considering different frequency indices of the leading POD mode ($n = 1$). The third column shows reduced order reconstructions of these velocity fluctuation fields using the leading POD modes at all frequencies. The next three columns show individual contribution to reconstructions in column III at the first 3 Rossiter frequencies. The reconstructions at Rossiter frequencies show harmonic functions with defined periodicities. The time scale associated with the wave (characterized by two alternating eddies) at Rossiter frequency 1 is 3.74, at Rossiter frequency 2 is 1.4, and at Rossiter frequency 3 is 0.934 which correspond to 590 Hz, 1572 Hz, and 2358 Hz respectively indicating the periodic nature of these reconstructions.

% energy	Weights of modes	Rms fluctuation plot
20 %	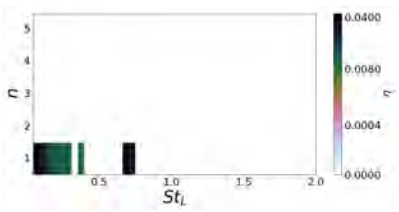	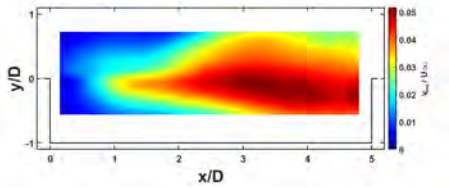
35 %	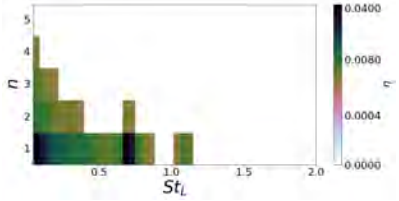	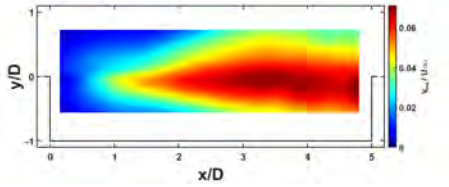
50 %	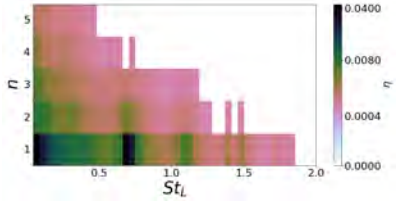	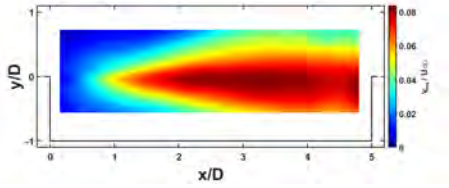
65 %	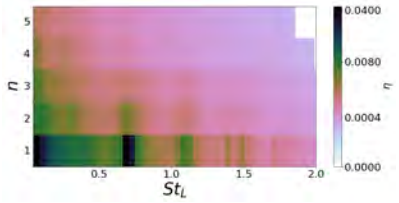	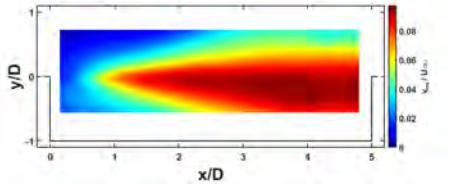

Figure 20: Reconstructed wall-normal rms velocity fluctuation contours increasing number of included space-time POD modes for increasing energy content

Commonalities between reconstructions are observed. These reconstructions show large scale eddie structures expanding as they convect downstream which is characteristic of the growing shear layer. There are differences, however, in the path taken by these eddie structures. Rossiter frequency 1 reconstructions are more dominant in the recirculation region of the cavity and interact with the lower section of the cavity aft wall. Reconstructions at Rossiter frequencies 2 and 3, however, are more prominent in the entire shear layer and interact with the upper half of the cavity aft wall. A major point evident from single mode reconstructions is that while reconstructions from individual modes of the snapshot POD are stationary with respect to the cavity flow field, reconstructions with the frequency based POD modes convect down the cavity shear layer representing physically meaningful structures. It is to be noted that even though individual reconstructions at Rossiter frequencies do not fully represent large scale structures, interactions of these structures reproduce most of the large scale structures in the measured velocity fluctuation field as seen in column III.

To analyze effects of different POD modes at a given frequency, Fig. 22 compares instantaneous POD reconstructions with bandpass filtered measured velocity fluctuations (using an FFT based filter) at Rossiter frequency 2. Figures 22((c)), ((d)) and ((e)) show POD reconstructions of modes 1, 2 and 3 respectively at Rossiter frequency 2. The three reconstructions show different events with eddies interacting with different sections of the cavity aft wall. It can be seen that, even at a defined frequency, resonance phenomena is not a simple event but is composed of many events at that frequency. The interactions of these events, as seen in Fig. 22((b)), provides a better representation of the large scale structures of the velocity fluctuation field at Rossiter frequency 2.

Since ample research has been done to elucidate the Mach number dependencies associated with snapshot POD modes, such as Murray et al. (2009), here we only discuss Mach number dependencies of the space-time POD modes. As mentioned before, the datasets are

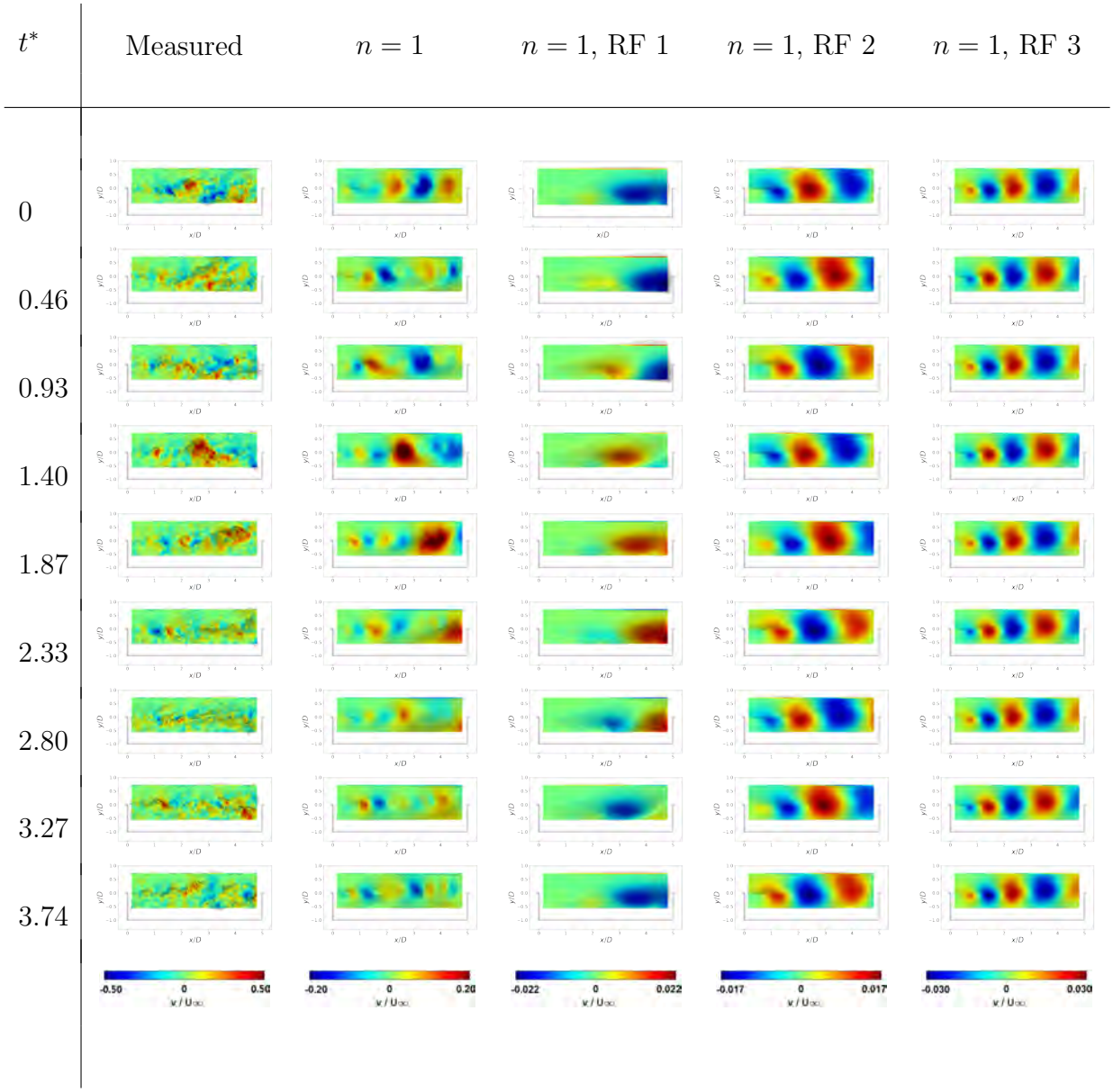

Figure 21: Time evolution of leading POD mode reconstructions of velocity fluctuations with overlaid wall-normal component contours for all frequencies compared with first 3 Rossiter frequencies

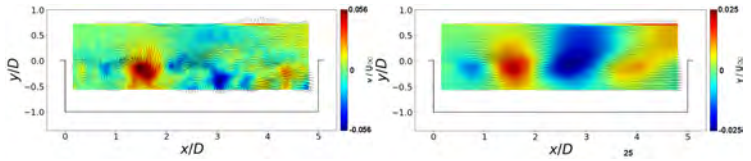

(a) Bandpass filtered measured

(b) First 3 POD mode reconstruction

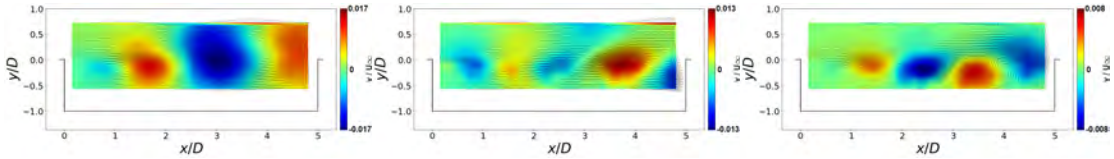

(c) POD mode 1 reconstruction

(d) POD mode 2 reconstruction

(e) POD mode 3 reconstruction

Figure 22: Instantaneous POD reconstructions of velocity fluctuations with overlaid wall-normal component contours at Rossiter frequency 2 with measured velocity bandpass filtered at Rossiter frequency 2

for three different free-stream Mach numbers of 0.6, 0.8 and 0.94. The pressure PSD plots at the three Mach numbers can be seen in Figure 23. It can be seen that the most dominant peaks for Mach 0.6 flow occur at Rossiter frequency 3, for Mach 0.8 flow at Rossiter frequency 2 and for Mach 0.94 flow at first 3 Rossiter frequencies, meaning, different Rossiter frequencies dominate the flow at different free-stream Mach numbers.

Eigenvalue spectrum of space-time POD modes for the first 2 POD modes at the three Mach numbers can be seen in Figure 24. It can be observed that, the most dominant peak for Mach 0.6 flow occurs at Rossiter frequency 3, for Mach 0.8 flow at Rossiter frequency 2 and for Mach 0.94 flow it occurs at all the first 3 Rossiter frequencies. These are consistent with peaks in their respective pressure PSD plots. Mach 0.6 spectra also peaks at Rossiter frequency 5 which is consistent with the peak seen at this frequency in the pressure spectra.

Eigenvalue convergence of the POD modes at individual Rossiter frequencies have also been calculated and can be seen in Figure 25.

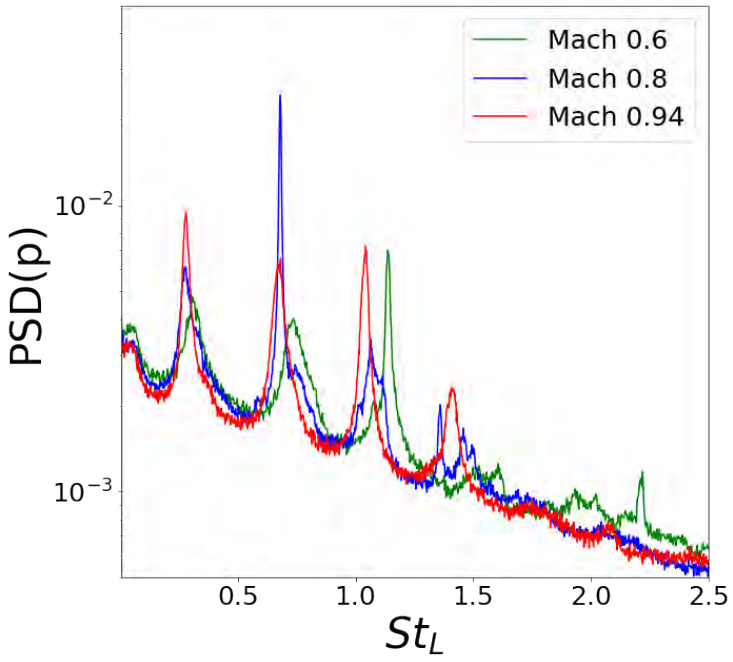

Figure 23: Aft wall pressure fluctuation PSD at different free-stream Mach numbers

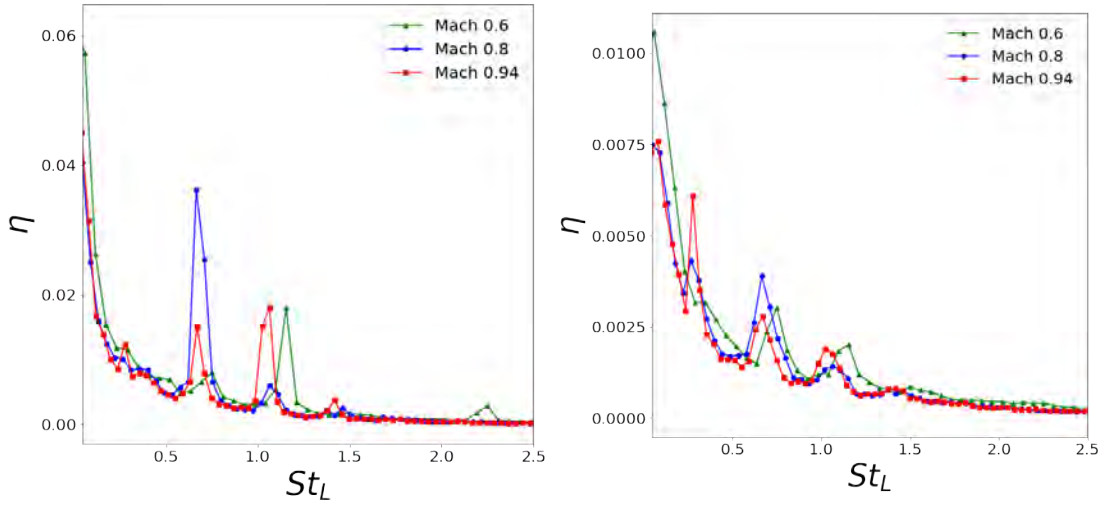

(a) POD mode 1

(b) POD mode 2

Figure 24: Eigenvalue spectrum at different free-stream Mach numbers for the first 2 POD modes

Figure 26 compares the leading wall-normal POD eigenvectors (complex in nature) for the first 3 Rossiter frequencies for the three different Mach numbers where only the real part is shown as before. On inspection, a similarity in scale and shape is observed for

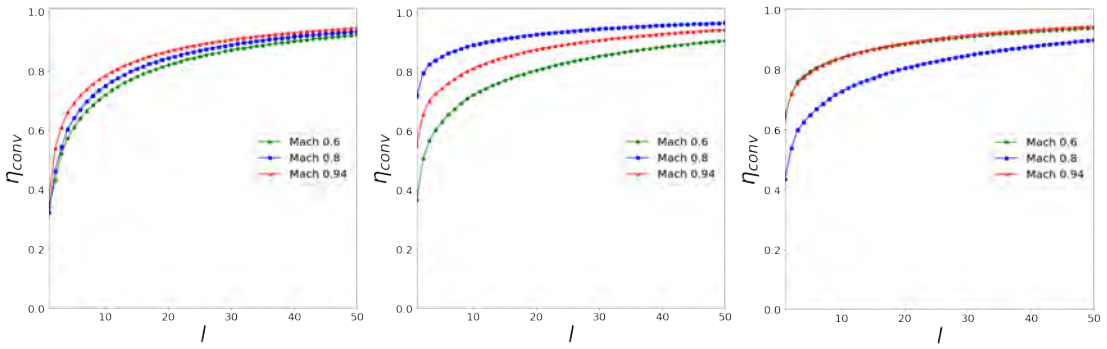

(a) Rossiter frequency 1 (b) Rossiter frequency 2 (c) Rossiter frequency 3

Figure 25: Eigenvalue convergence of different free-stream Mach numbers at the first 3 Rossiter frequencies

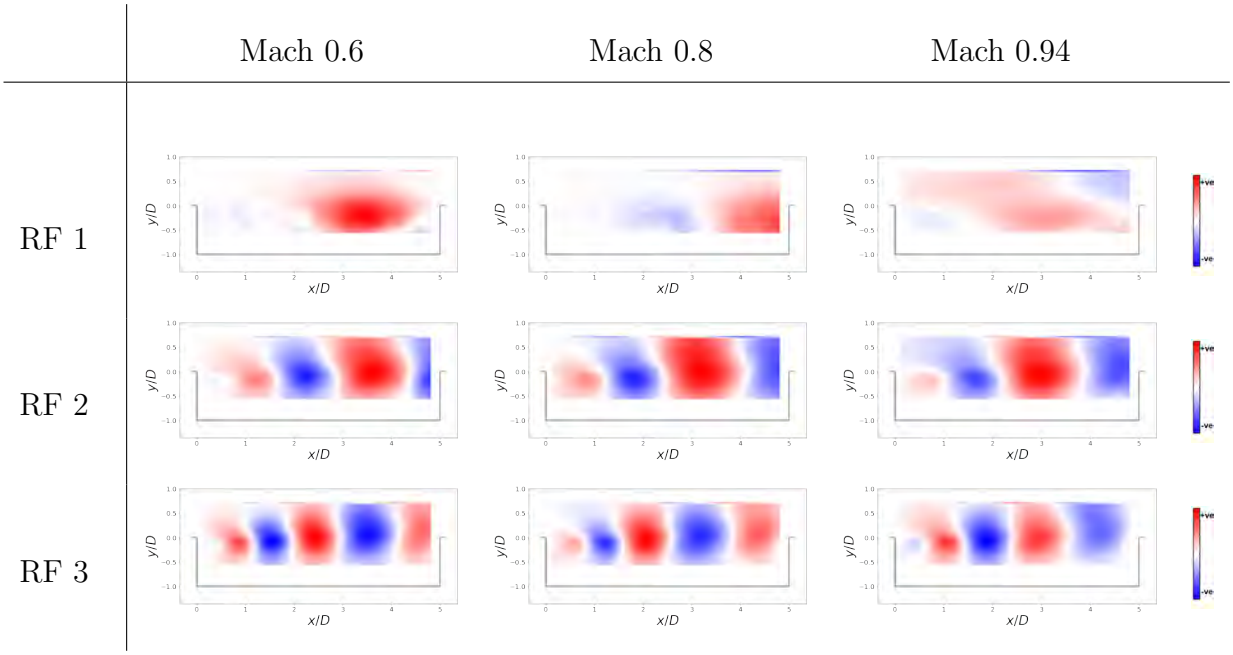

Figure 26: Contour plots for space-time POD eigenvectors in wall-normal direction ($real(\Phi_v(\mathbf{x}, f))$) of the first POD mode at the first 3 Rossiter frequencies at three distinct free-stream Mach numbers

eigenvectors at the same Rossiter frequencies despite different free-stream flow conditions. This suggests that similar eddie structures are present at Rossiter frequencies irrespective of the free-stream Mach number. Since Rossiter's formulation (Rossiter, 1964) predicts the

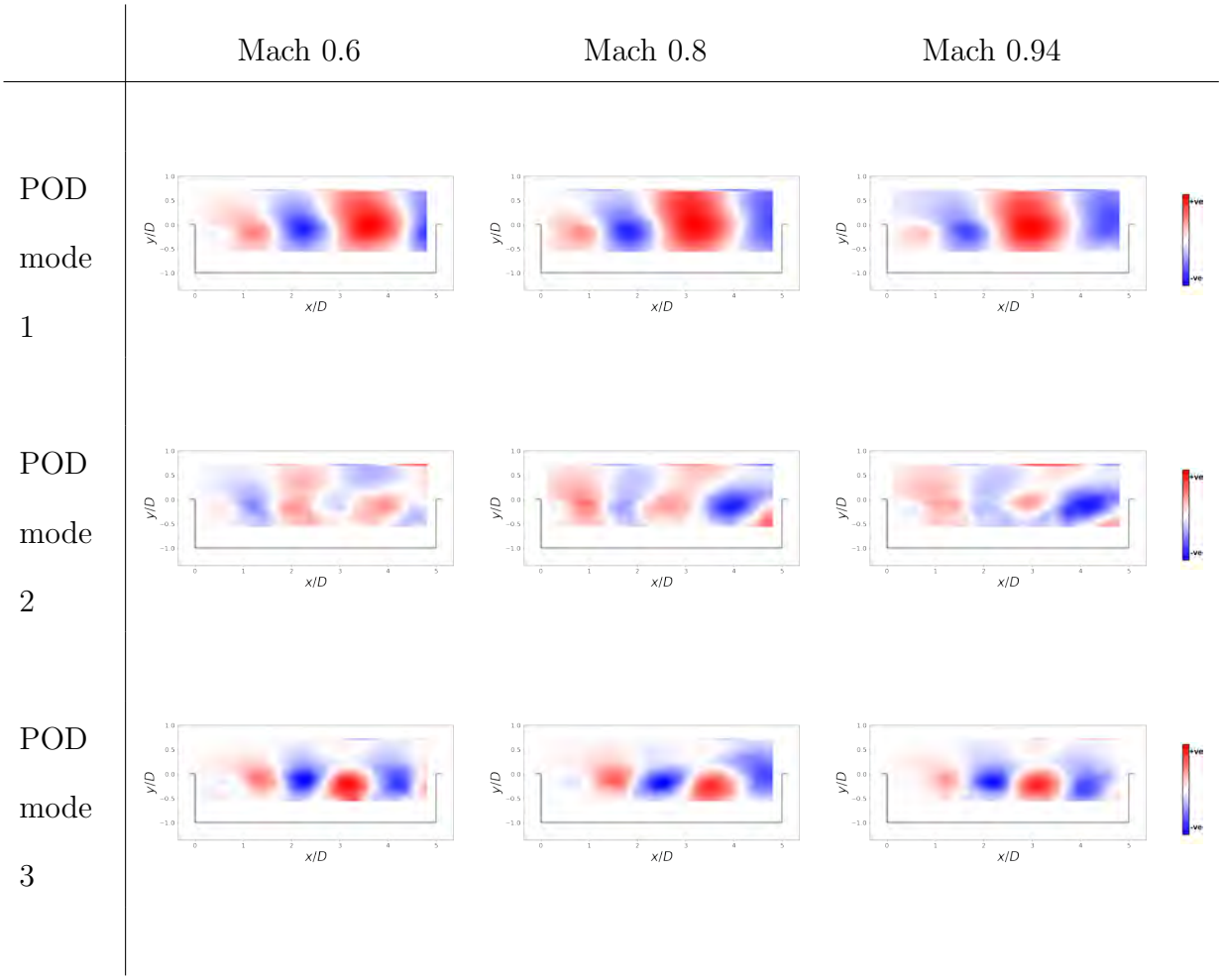

Figure 27: Contour plots for space-time POD eigenvectors in wall-normal direction ($real(\Phi_v(\mathbf{x}, f))$) of the first three POD modes at Rossiter frequency 2 at three distinct free-stream Mach numbers

Strouhal numbers of resonant tones, this suggests that the mode structures may be linked to the Strouhal numbers they correspond to. Further, contour plots have also been compared at the three free-stream conditions for the first 3 POD modes at Rossiter frequency 2 in Fig. 27. Again, only the real part of the complex eigenvector in the wall-normal direction have been presented with a red-white-blue color scheme. Similarity in scale and shape of the eigenvectors for the same POD mode number is also evident despite the difference in free-stream flow conditions. In order to quantitatively assess the similarity in the mode

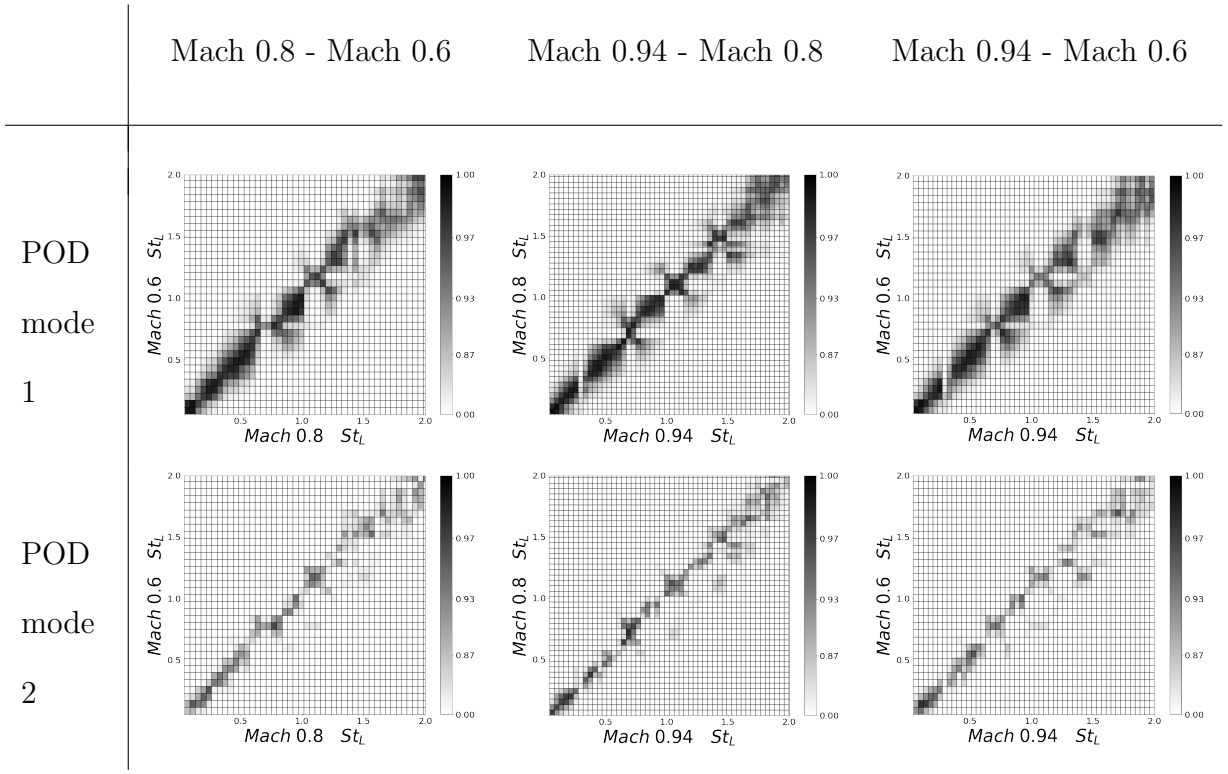

Figure 28: Similarity parameter between different free-stream Mach numbers at first 2 POD mode numbers

structures, the use of a similarity parameter defined by Rempfer **?** can be employed. This can be obtained by spatial dot product defined by,

$$\gamma_{i,j} = *(\vec{\Phi}^i)_1(\vec{\Phi}^j)_2, \quad i,j = 1,2,..., \tag{47}$$

where, i and j represent different free-stream Mach numbers and $\vec{\Phi}$ represents the basis function in vector form. Since POD modes are unitary vectors, the similarity in structures can be identified by closeness of the similarity parameter to a unit value. Additionally, if the modes are dissimilar, this parameter will go to zero. This similarity parameter, for space-time POD modes, is a function of frequency f, and POD mode number, n. The Strouhal number variation of similarity parameter for the first and second POD mode number for space-time POD eigenvectors is shown in Fig. 28. To enhance the higher magnitude similarity parameters, an exponential colorbar is used. High magnitudes are observed

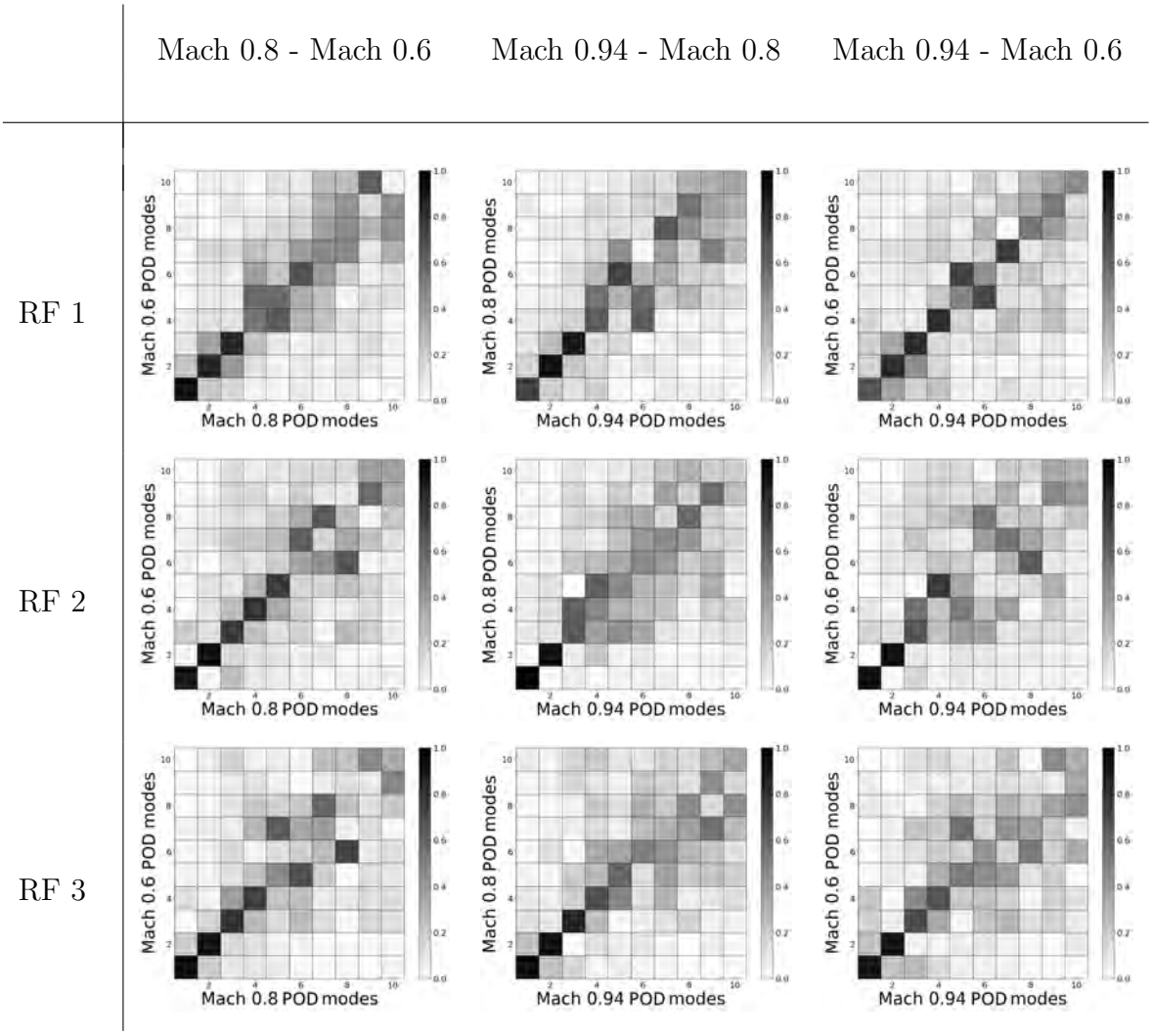

Figure 29: Similarity parameter between different free-stream Mach numbers at first 3 Rossiter frequencies

along the diagonals of both the plots. This suggests that similar eigenvectors exist at the same Strouhal number for different free-stream Mach numbers. This highlights the spatial structure at a given frequency being consistent with Rossiter's work (Rossiter, 1964) where wavelengths of structures across cavity are associated with different Rossiter (stream-wise) modes which scale with Strouhal number. Following this analysis, similarity parameters were studied for various POD mode numbers obtained at Rossiter frequencies. This is shown for first 3 Rossiter frequencies in Fig. 29. Higher magnitude along the diagonal for each of the comparisons show that the leading POD mode structures at Rossiter frequencies

resemble each other at different free-stream conditions.

3.3 SAMM

$G_{x_i x_j}$ consists of the auto- and cross-spectral densities of the pressure signals along and off the diagonal, respectively. As a result of finite random measurement noise, the inputs are partially correlated, in which case $G_{x_i x_j}$ is a full-rank matrix and can be inverted to solve for H via Eq. 17. Furthermore, it can be decomposed via an eigendecomposition. Thus, Eq. 30 is used to compute the independent source auto-spectral densities, G_{ww}, and the eigenvalue spectra of the first five modes are shown in Fig. 30. By construction, the eigenvalues of POD mode 1 possess the well-known characteristics of a cavity flow, showing multiple spectral peaks indicative of the Rossiter tones. The modified Rossiter equation (Heller et al., 1971) is

$$St = \frac{fL}{U_\infty} = \frac{n - \alpha}{1/\kappa + Ma/\sqrt{1 + (\gamma - 1)Ma^2/2}}, \tag{48}$$

where $\alpha = 0.38$ is the phase lag, $\kappa = 0.65$ is the convective speed ratio as reported in Zhang et al. (2019), n is the Rossiter mode index, and γ is the specific heat ratio. It is clear that the prediction matches well with the tonal frequencies. The eigenvalues of lower ranked modes are significantly lower, adding broadband content. The POD velocity modes associated with the Rossiter frequencies, indicated by the black squares, are presented later.

Recall that the eigenvectors, A, of $G_{x_i x_j}$ are also obtained via Eq. (30). Therefore, we can construct a low-rank approximation of $G_{x_i x_j}$. Rank-1 approximations of $G_{x_i x_i}$ of sensors 1 and 10 are compared to their respective measured autospectral density in Fig. 31. The rank-1 approximations match well with the measured autospectral density at the narrowband peaks. Minor discrepancies exist in the broadband content, which shows that broadband turbulent features cannot be accurately captured with such an approximation.

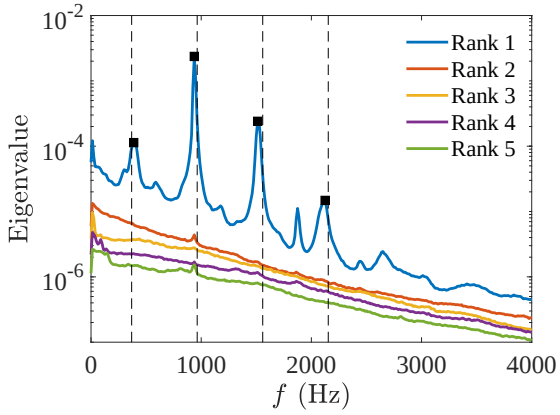

Figure 30: Eigenvalue spectra of the first five modes of $G_{x_i x_j}$ versus frequency using all 10 sensors. The dashed-lines are the predicted Rossiter frequencies using Eq. 48. The square markers indicate the frequencies for the velocity modes.

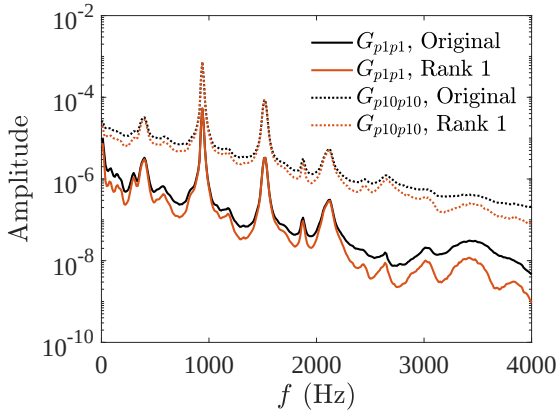

Figure 31: Low-rank approximation of $G_{p_i p_i}$ using 10 sensors.

Fortunately, we are primarily interested in capturing the dynamics of the energetic coherent flow structures, so the rank-1 approximation is suitable in this instance.

With the TR-PIV data, the spectral POD modes of the velocity fields can be directly calculated using the pwelch algorithm provided by Towne et al. (2018) with the same normalized area weighting approach as for the 15 Hz PIV data. A Hamming window is used, and the N_{FFT} is 1280 with a 75% overlap, which results in 23 effective blocks. The random uncertainty associated with this analysis is approximately 20% due to the limited number of records. With these settings, the spectral resolution is 12.5 Hz, which is chosen to match that of the SAMMs with $N_{FFT} = 2048$.

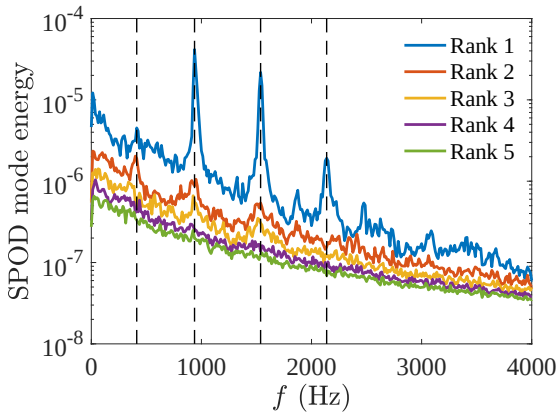

Figure 32: Eigenvalue spectra of the first five modes versus frequency from TR-PIV SPOD.

Fig. 32 shows the re-scaled eigenvalue spectra for the five highest-ranked POD modes. The energy in the rank-1 mode is significantly higher than the rest, which is similar to that observed for $G_{x_i x_j}$ in the previous section. The modes shapes associated with the Rossiter frequencies indicated by the dashed lines are extracted as shown in Fig. 33. Mode shapes of both u and v exhibit traveling wave patterns that are clearly observed via animation of the modes (not shown). The wavelength of the coherent structures reduces with increasing frequency as expected.

For SAMMs, one of the open questions is the number and location of unsteady pressure sensors used in the MIMO system (Arunajatesan et al., 2007). In an open cavity, in which

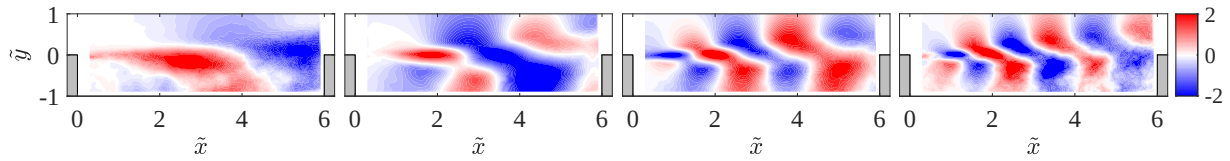

(a) Mode shape of u

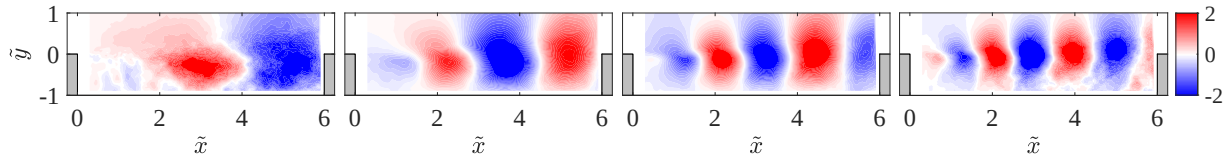

(b) Mode shape of v

Figure 33: Dominant mode shapes corresponding to first 4 Rossiter frequencies from SPOD of TR-PIV.

the shear layer spans the cavity mouth, the trailing edge is generally acknowledged as the acoustic source that generates acoustic waves, indicative of a single dominant source. Fig. 30 verifies that only one independent source is required to describe the characteristics of the cavity flow. It is perhaps intuitive to choose at least one sensor near the trailing edge. Therefore, we tested three combinations of sensors to investigate the effects:

1. All ten sensors,

2. Two sensors with one near the leading edge (sensor 1) and the sensor on the aft wall (sensor 10), and

3. Two sensors near the leading edge (sensors 1 and 2, see Fig. 2).

Case 1 uses information from all sensors, while Case 2 captures the global features with just two sensors closest to the source. Case 3 is challenging because these two sensors are located farthest from the source. The following discussion compares these three cases.

As described previously, SAMM-SPOD calculates X for multiple blocks and $\hat{Y}'\hat{Y}$ directly after computing H. The POD modes are then obtained by solving the smaller

snapshot eigenvalue problem using Eq. 25. The spectra of the rank-1 eigenvalues for different cases are compared in Fig. 34. For the same combination of sensors (1 and 2), the eigenvalues do not change significantly with an increasing of number of blocks. This is expected as the eigenvalues are the characteristics of the system. When all of the sensors are used, the eigenvalue spectrum changes slightly at the less-energetic first and fourth Rossiter frequencies. The eigenvalue amplitude does not change significantly at the most energetic (2^{nd} and 3^{rd}) Rossiter frequencies.

With all 4772 blocks used in the SAMM-SPOD in the current example to obtain the modes, the results are shown in Fig. 35. We find that the mode shapes are consistent for the different sensor combination cases; therefore, only the mode shapes for the all-sensors case are shown for brevity. We note that increasing the number of blocks reduces the noise in the ensemble average. The modes show, suitably adjusted in phase, are in very good agreement with those from the TR-PIV results shown in Fig. 33, particularly the dominant second and third Rossiter modes.

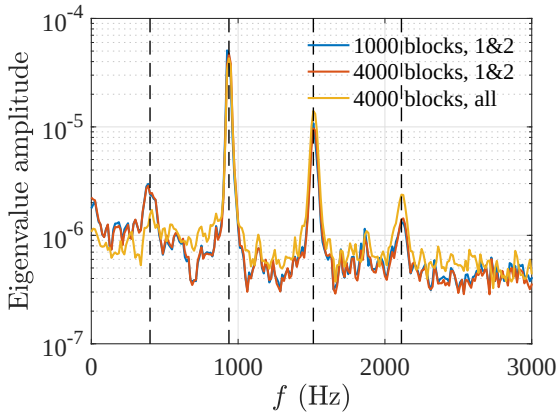

Figure 34: Eigenvalues from SAMM-SPOD for v-component versus frequency. The dashed lines indicate Rossiter frequencies.

The SAMM-RR algorithm shown in Fig. 7 is a reduced-rank approximation that is much more computationally efficient than SAMM-SPOD since it does not require an eigen-decomposition of the velocity cross-spectral matrix. The re-scaled eigenvalues ($\overline{G}_{ww}$ from

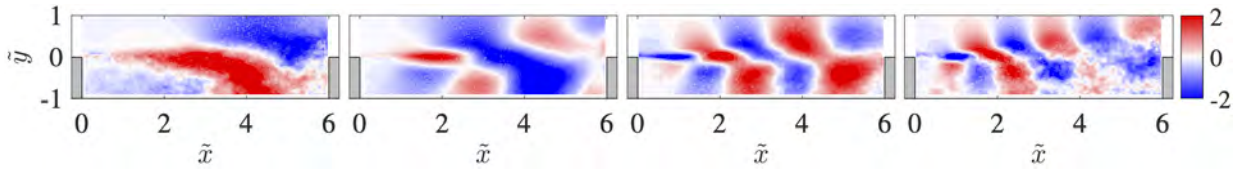

(a) mode shape of u

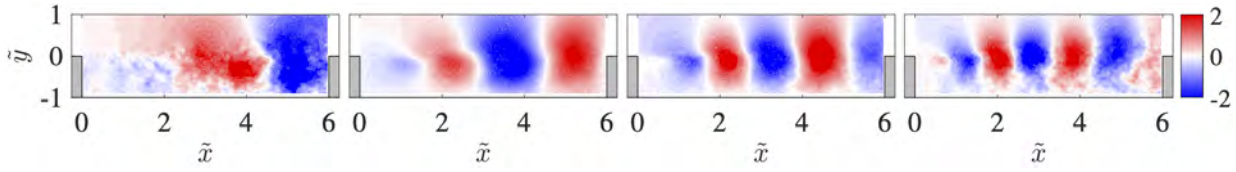

(b) mode shape of v

Figure 35: Rank-1 POD modes corresponding to first 4 Rossiter frequencies from SAMM-SPOD using 10 sensors.

Eq. 33) versus frequency for three cases are shown in Fig. 36. For SAMM-RR, the dominant eigenvalues do not change significantly for the different sensor combinations, which indicates the global nature of the flow field. We also note that the eigenvalues at the Rossiter frequencies are very close to those of SAMM-SPOD in Fig. 34.

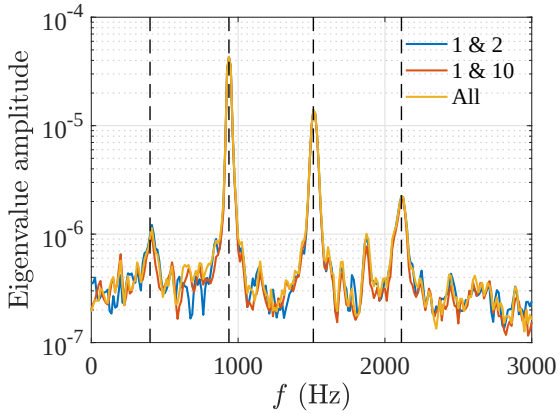

Figure 36: Eigenvalues (rank-1 of $\overline{G}_{ww}$) for v-component versus frequency. The dashed lines indicate the Rossiter frequencies.

The dominant POD modes, located in the first column of $\overline{H}_{yw}$, associated with first four Rossiter frequencies are obtained. Again, we compare the results obtained for the 3 sensor

combinations above in Fig. 37. It is clear that these modes are very similar to the TR-PIV SPOD modes in Fig. 33. Furthermore, the modes obtained by different combinations of sensors are almost identical. These observations indicate that the dynamics of the cavity flow is a global feature that can be captured by a sensor located anywhere inside the cavity (except at a pressure node). The good agreement between the SPOD modes and SAMMs modes shows that the SAMMs are capable of finding the dominant dynamic coherent flow structures without time resolved velocity data.

Here we assess the uncertainty of G_{xy}. While $G_{x_i x_j}$ can be accurately estimated using the standard periodogram method via the long time series of the TR pressure data, the cross correlations between unsteady TR pressure and NTR velocity must use Eq. 20 followed by Eq. 23. The reduced number of terms in the ensemble average compared to that available with all TR data increases the random error. We can evaluate the impact of the number of averages qualitatively by examining the difference between using TR vs. NTR pressure data to estimate the correlations. The NTR pressure data sequence is obtained by retaining only those samples corresponding to the instances when the dual lasers pulse, thereby simulating the PIV data sequence.

Fig. 38 shows a "zoomed-in" view of the cross correlation coefficient as a function of dimensionless time delay between pressure sensors 1 and 10 computed two ways. The first, denoted as "TR", uses all TR pressure data, while the second, denoted as "NTR", uses a NTR pressure sequence combined with a second TR pressure data sequence. The one calculated using NTR data uses 4772 averages, corresponding to the number of PIV snapshots, while the TR data is computed using the entire time series of pressure data. A slight amplitude mismatch is noted at the local extrema, while the temporal locations of the extrema are accurately captured. Although the example shown is for the unsteady pressure signals, similar discrepancies are expected for the cross correlations between the unsteady pressure and the velocity field.

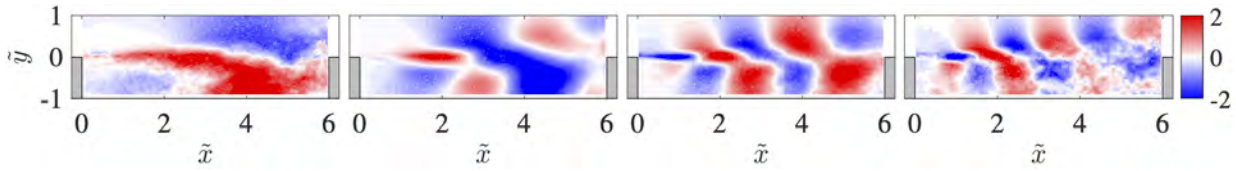

(a) Mode shape of u, case 1

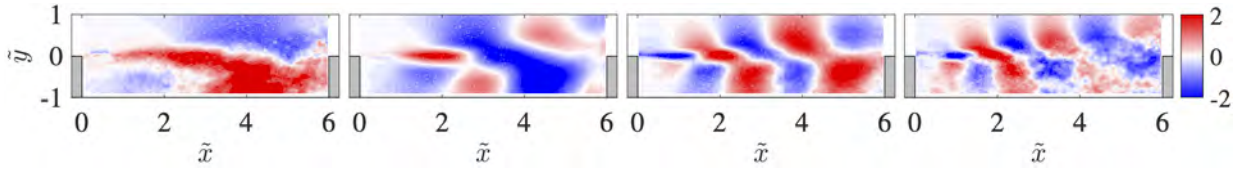

(b) Mode shape of u, case 2

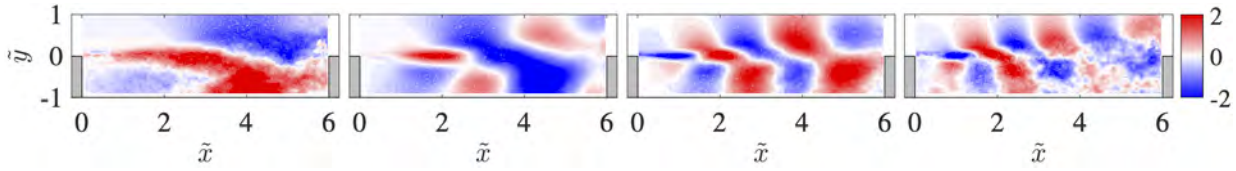

(c) Mode shape of u, case 3

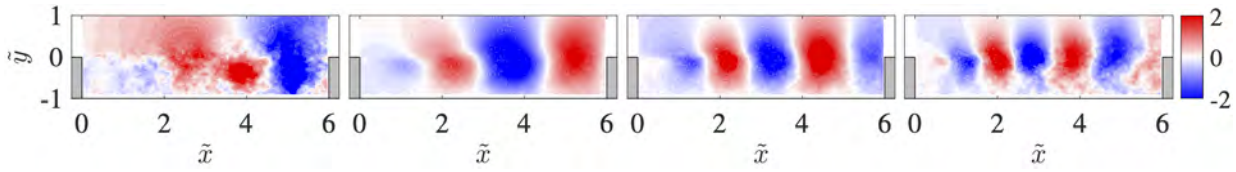

(d) Mode shape of v, case 1

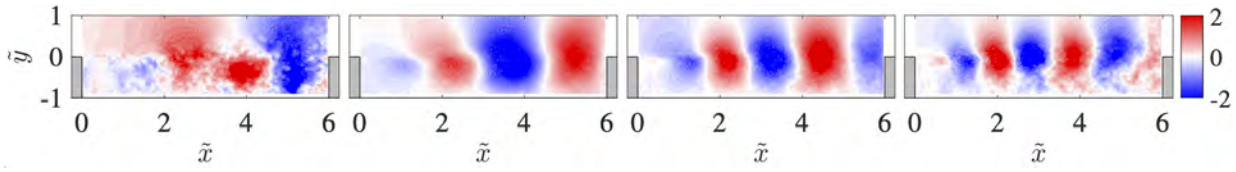

(e) Mode shape of v, case 2

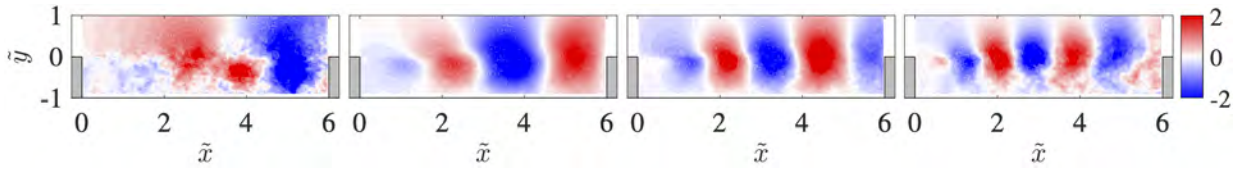

(f) Mode shape of v, case 3

Figure 37: Rank-1 POD modes corresponding to first 4 Rossiter frequencies from SAMM-RR. Case 1: all sensors; case 2: 1^{st} and 10^{th} sensors; case 3: 1^{st} and 2^{nd} sensors.

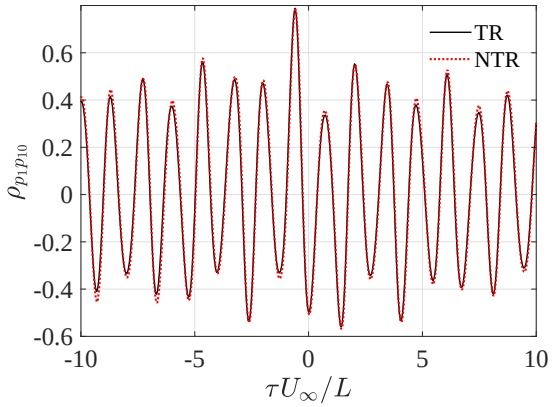

Figure 38: Zoomed-in comparison between the cross-correlation coefficient between pressure sensors 1 and 10 calculated using TR data and NTR data via Eq. 20.

Bendat and Piersol (2011) provide an estimate for the normalized rms random error in the cross correlation coefficient between two zero-mean TR signals, x and y, under the assumption that both are band-limited white noise signals, as

$$\epsilon[\hat{R}_{xy}(\tau)] \approx \frac{1}{\sqrt{2BT_{\text{total}}}}[1 + \rho_{xy}^{-2}(\tau)]^{0.5}, \tag{49}$$

where B is the bandwidth, $T_{\text{total}} = N_{\text{total}}\Delta t$ is the total record length, and ρ_{xy} is the dimensionless correlation coefficient. For TR data, the term $2BT_{\text{total}} \approx N_{\text{total}}$, so ϵ exhibits the expected inverse square root dependence on the number of averages. By increasing the number of PIV snapshots, the correlation functions calculated from the NTR data will converge to the ones calculated using TR data; thus, the random error can be reduced. This is illustrated in Fig. 39, where the mean-square difference between the two cross correlation coefficient estimates, which is expected to be close to the mean-squared error for an unbiased estimator, is $\propto 1/N_{\text{averages}}$. Experimentation for the cavity flow case suggests that at least 1000 snapshots are required for statistical convergence.

The other item to address with regards to uncertainty is the FFT of the windowed cross correlation. A zoomed-out view of the cross-correlation in Fig. 38 is shown in Fig. 40. The magnitude of the correlation coefficient decreases for large $|\tau|$. However, it does not rapidly

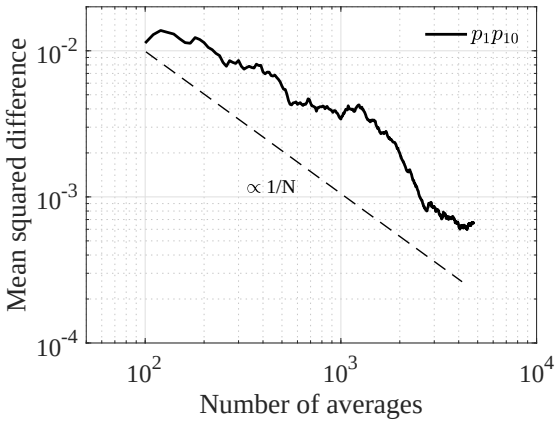

Figure 39: Mean-squared difference between the cross-correlation coefficient computed between pressure sensors 1 and 10 using NTR data versus TR data.

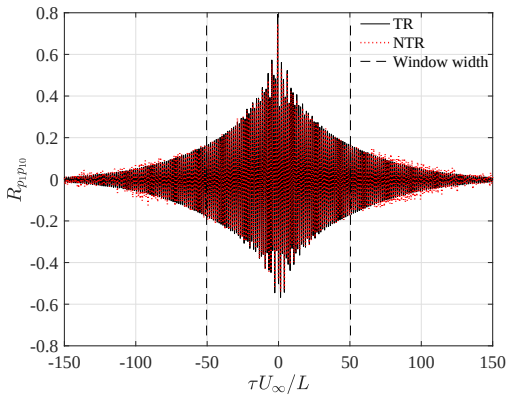

Figure 40: Zoomed-out comparison between the cross-correlation coefficient between pressure sensors 1 and 10 calculated using TR data and NTR data via Eq. 20.

decay to zero due to the natural self-sustaining oscillations of the cavity flow. In practice, the maximum time delay, $\tau_{\max}$, should be large enough so that the correlation coefficient decays to approximate noise levels and such that $1/(2\tau_{\max})$ is the desired frequency resolution f_s/N_{FFT}. For example, $N_{FFT} = 2048$ and 4096 correspond to $(\tau U_\infty/L)_{\max} = 50$ and 100, respectively in Fig. 40, yielding correlation coefficients of ≈ 0.1 or less. Noting the increasing discrepancy between for $(\tau U_\infty/L)_{\max} > 60$, we find $N_{FFT} = 2048$ to be a suitable compromise.

3.4 Resolvent Analysis and Control of Numerical Simulations

Analysis of the numerical simulation data were conducted using resolvent methodology and these results were used to guide numerical flow control experiments which are discussed in the following section.

3.4.1 Resolvent Analysis

As we initiate the resolvent analysis of the turbulent cavity flow, stability analysis is first performed on $L(\bar{q};\beta)$ to evaluate its stability properties. The eigenspectra and pseudospectra are shown in figure 41(a) for two representative cases with $\beta = \pi$ and 3π. The imaginary part of the eigenvalue λ is normalized as $\lambda_i L/(2\pi u_\infty)$ and the real part is normalized as $\lambda_r D/u_\infty$. The results indicate the linear operator $L(\bar{q};\beta)$ is unstable with positive growth rates ($\lambda_r D/u_\infty > 0$) of the eigenmodes, including both centrifugal and shear-layer modes. The spatial structures of two representative unstable modes, a centrifugal and a shear-layer mode, are shown in figure 41(b). The centrifugal mode is present inside of the cavity, which corresponds to the recirculation (Brès and Colonius, 2008). However, the shear-layer mode appears over the cavity and is formed due to the Kelvin-Helmholtz instability.

We show the pseudospectra contours (Trefethen and Embree, 2005) of the linear operator $L(\bar{q};\beta)$ as the background in figure 41(a). Higher values of contours appear on

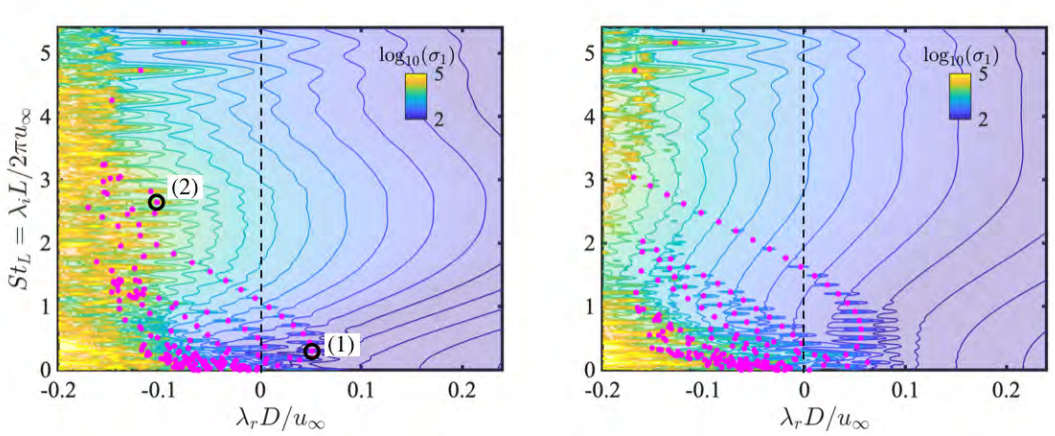

(a) Eigenspectra at $\beta = \pi$ and 3π

(b) Centrifugal and shear layer modes

Figure 41: (a) Eigenspectra and pseudospectra of $L(\bar{q};\beta)$ for spanwise wavenumbers $\beta = \pi$ (left) and 3π (right). The magenta dots indicate the growth rates and frequencies of $L(\bar{q};\beta)$. The dashed line indicates the neutral stability line. The contour plots visualize the pseudospectra. (b) The (1) centrifugal and (2) shear-layer modes visualized by the real component of the streamwise velocity. The locations of their eigenvalues are indicated on plot (a).

the left-hand side planes for both cases of $\beta = \pi$ and 3π, where the stable eigenvalues are located. For the case of $\beta = \pi$, pseudospectral levels protrude far into the unstable plane at $1 < \lambda_i L/(2\pi u_\infty) < 4$ representing non-normal behavior of the operator. For the case of $\beta = 3\pi$, the non-normal behavior of the operator occurs in the frequency range of $2 < \lambda_i L/(2\pi u_\infty) < 5$. The non-normal behavior of the operator can cause the flow to exhibit significant energy amplification.

Because the linear operator $L(\bar{\boldsymbol{q}}; \beta)$ is unstable, we perform a discounted resolvent analysis. The discounting parameter is associated with temporal windowing of the system response to examine the dynamics before the instability diverges, as discussed in **??**. The leading and secondary gains for the case of $\beta = 2\pi$ using different discounting parameters of $\kappa D/u_\infty = 0.1$, 0.2 and 0.3 are shown in 42. We observe that, as $\kappa D/u_\infty$ increases, the magnitude of resolvent gain decreases. However, the profile of the gain distribution is not altered by the choice of discounting parameter. In fact, the maximum gain is achieved at the same Strouhal number of $St_L \approx 3$.

The large separation between the primary and secondary gains (σ_1 and σ_2) for $St_L > 0.5$ enables the application of the rank-1 assumption in the present study. By using the rank-1 assumption, we focus on the leading gain and its corresponding forcing and response modes (McKeon and Sharma, 2010; Gómez et al., 2014; Schmidt et al., 2017). Here we choose the discounting parameter of $\kappa D/u_\infty = 0.2$ in the resolvent analysis to analyze the unstable system.

The leading singular value versus various combinations of spanwise wavenumber and frequency is presented in figure 43, revealing the optimal energy amplification of harmonic forcing. Larger amplification that emerges around $2 < St_L < 4$ and $\pi/2 < \beta < 5\pi/2$ is apparent in this figure. As Rossiter modes primarily stem from two-dimensional shear-layer instabilities, the gain distribution with $\beta = 0$ exhibits discrete peaks at the Rossiter mode frequencies, which are consistent with the power spectral density of pressure shown in

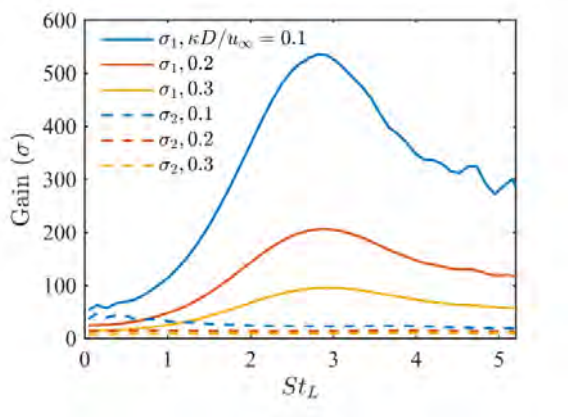

Figure 42: Resolvent gain calculated using discounting parameter of $\kappa D/u_\infty = 0.1$, 0.2 and 0.3 for $\beta = 2\pi$.

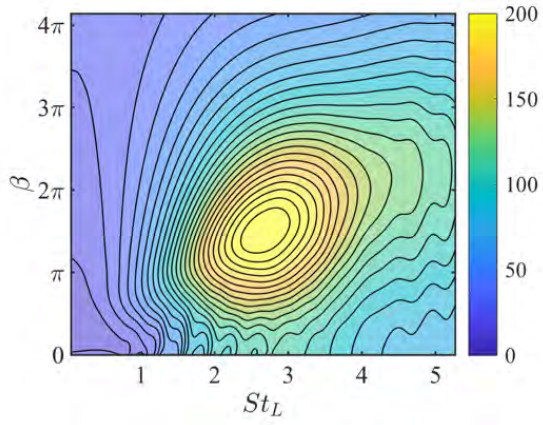

Figure 43: The leading energy amplification σ_1 over β and St_L for a discount parameter of $\kappa D/u_\infty = 0.2$.

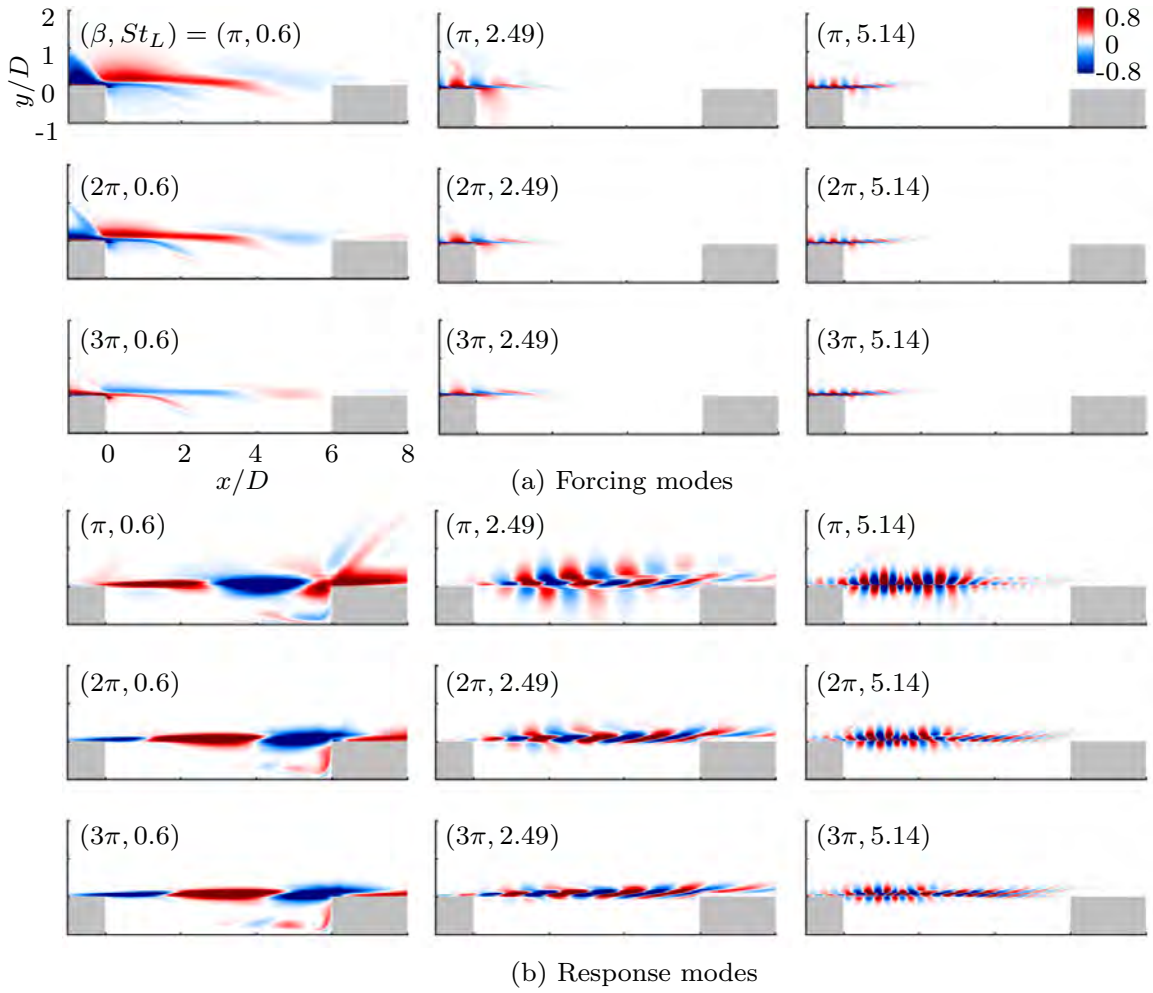

(a) Forcing modes

(b) Response modes

Figure 44: Real streamwise velocity component of the (a) forcing and (b) response modes at $St_L = 0.6$, 2.49 and 5.14 with $\beta = \pi$, 2π and 3π.

figure **??** from the nonlinear flow simulation. On the other hand, for spanwise wavenumbers $\beta > \pi$, the gain exhibits a smoother distribution versus Strouhal number.

The representative forcing and response modes are presented in figure 44 for $\beta = \pi$, 2π and 3π at $St_L = 0.6$, 2.49 and 5.14 which show the lower, middle and high-frequency cases. The forcing and response modes are shown with the real streamwise component in figure 44(a) and (b), respectively. The influence of frequency and spanwise wavenumber on mode structures are similar for both forcing and response modes. As the frequency increases, the streamwise structures exhibit a finer pattern. The structures become more compact in the transverse direction as the spanwise wavenumber increases. For the forcing modes, the dominant structures emerge at the leading edge of the cavity. This indicates that the optimal spatial location for the unsteady forcing input is indeed at the leading edge of the cavity, substantiating the actuator location discussed in §**??**. For the response modes, the structures appear over shear layer region and inside the cavity for the low-frequency case. As the frequency increases, the response mode structures are confined to the shear-layer region.

Wave structures emerge at the leading and trailing edges of the cavity for the case of $(\beta, St_L) = (\pi, 0.6)$. Such wave structures become weaker and disappear for larger values of β. This change is due to the two-dimensional property of compression waves. As the spanwise wavenumber increases, the three-dimensionality suppresses the generation of two-dimensional compression waves. For the case of $St_L = 2.49$, the compression waves structures disappear. For higher frequencies, the compression waves appear at the leading edge, as shown for the cases of $(\pi, 5.14)$ and $(2\pi, 5.14)$. The higher frequency forcing magnifies the obstruction effect at the leading edge, which results in the formation of compression waves in the response structures.

3.4.2 Resolvent analysis based active flow control design

In this section, the findings from the above resolvent and DMD analyses are used to design open-loop active flow control strategies for the attenuation of intense pressure fluctuations. The performance of the flow control techniques is then assessed through nonlinear LES. For all controlled cases considered below, the oscillatory momentum coefficient defined in (1) is fixed at 0.02. While the primary effort here is to reduce pressure fluctuations at $= 10,000$, we desire a control approach that can generalize to higher Reynolds numbers, thereby favoring case with the largest reduction. Therefore, we seek effective control setups but especially those that perform exceptionally well that can be promising for more challenging flow setup in future studies.

As discussed above, the DMD analysis reveals the coherent structures that are responsible for large-scale unsteadiness over the cavity. In a complementary manner, the resolvent analysis identifies structures that can be amplified through sustained forcing. Here, we look for the means to identify candidate input perturbations that will amplify over the cavity and inhibit the generation of the natural large-scale spanwise vortical structures identified by DMD. It should be noted that resolvent analysis is a linear analysis technique which essentially acts as a model for the nonlinear turbulent cavity flow with active flow control input. We therefore anticipate some differences but do not consider them to lead to substantial contradictions that prevent achievement of the objective of determining an effective control setup. We emphasize that resolvent analysis based guidelines discussed herein should be treated as a necessary condition but not as a sufficient condition to achieve effective flow modification. This means that the control parameter search space can be significantly reduced but requires careful assessment with companion LES (or experiments).

The DMD analysis of the uncontrolled flow shows that the primary oscillation at frequency of $St_L = 1.33$ is associated with the dominant spanwise wavenumber of $\beta = \pi$, as

shown in figure **??**. The control goal is therefore to force the cavity flow in a sustained manner to disrupt the formation of this undesirable structure. The optimal input disturbance should ideally persist over the entire cavity length without spilling its energy to the naturally energetic structures. It is noteworthy that our previous experiments (Lusk et al., 2012) indicated that effective three-dimensional steady blowing persisted over the entire cavity length, while less effective disturbances decayed. A subsequent experimental companion study (Zhang et al., 2019) showed that steady blowing actuation introduced counter-rotating vortex pairs in between blowing slots that distorted the shear layer and inhibited the growth of the large-scale vortical structures, mitigating the impingement effect. However, the control modification decayed towards the rear part of the cavity, which likely limited the control effectiveness. The goal in the present study is hence to select unsteady three-dimensional forcing inputs that persist over the cavity length and do not energize the natural $\beta = \pi$ disturbances.

Motivated by these previous studies and the results presented thus far, we introduce a guiding metric to assess the integrated kinetic energy along the streamwise direction using the leading response mode:

$$\hat{E}_1(x) = \int_{-D}^{\infty} \frac{1}{2}\sigma_1^2 \bar{\rho} \left[\hat{u}_1 \hat{u}_1^* + \hat{v}_1 \hat{v}_1^*\right] \mathrm{d}y, \tag{50}$$

where σ_1 is the leading gain, $\bar{\rho}$ is the time-averaged density, and $\hat{u}_1$ and $\hat{v}_1$ are the streamwise and vertical components of the response mode, respectively. Their complex conjugate counterparts are denoted as $\hat{u}_1^*$ and $\hat{v}_1^*$. The metric $\hat{E}_1$ quantifies the response kinetic energy and assesses the effectiveness of perturbation amplification over the cavity. For an effective amplification mechanism, we should observe a sustained profile of $\hat{E}_1$ over the entirety of the cavity shear layer to ensure that the forcing input remains influential over the whole extend of the cavity. We emphasize here that both the high value of $\hat{E}_1$ and the sustained profile over the cavity are sought to mitigate the large-scale fluctuations in

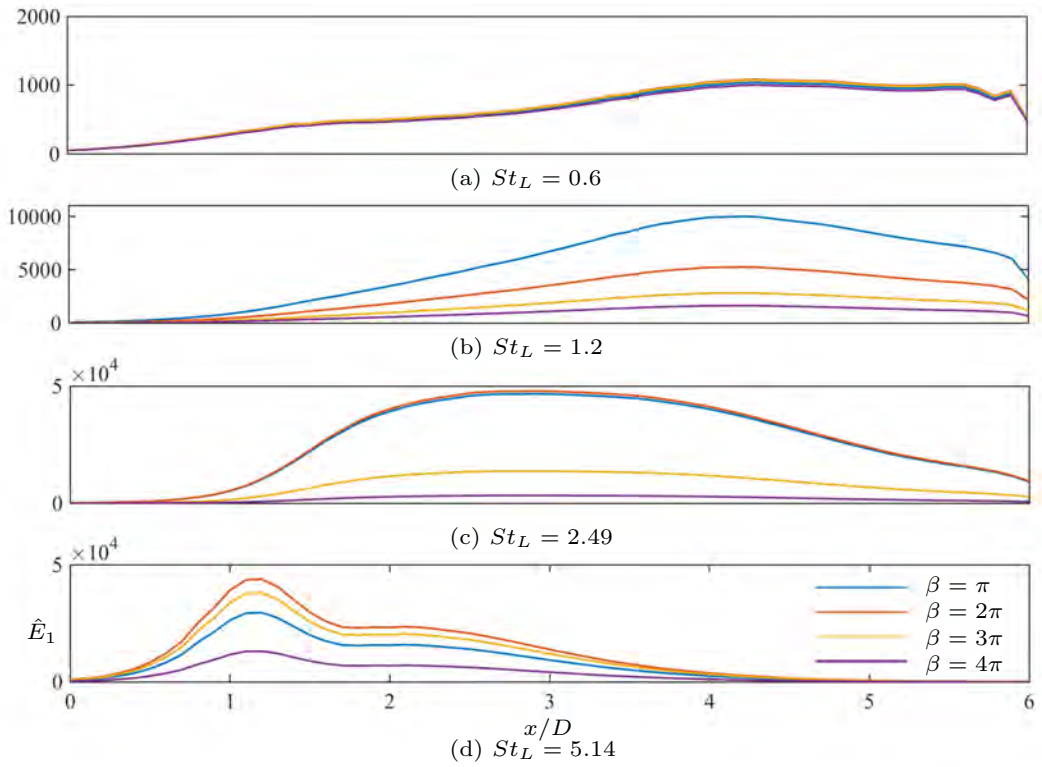

Figure 45: Kinetic energy amplification profiles based on the primary response mode over the cavity at frequencies of (a) $St_L = 0.6$, (b) 1.2 (c) 2.49 and (d) 5.14 for spanwise wavenumbers of $\beta = \pi, 2\pi, 3\pi$ and 4π.

cavity flow, as we discuss in detail below. This metric should be considered in conjunction with the physical insights gained from baseline LES and DMD analysis, and be viewed as a necessary condition to expect effective modification of the mean flow. This is due to the fact that the resolvent analysis is based on a linearization about the mean flow and can show some differences from the nonlinear cavity flow during the flow control process, for which we should place some care. Saturation of control performance in terms of reduction in pressure fluctuations could exist despite of favorable feature of the metric $\hat{E}_1$ due to nonlinear effects in the cavity flow.

The primary kinetic energy amplification profiles $\hat{E}_1(x)$ over the cavity for representative cases at frequencies of $St_L = 0.6$, 1.2, 2.49 and 5.14 and spanwise wavenumbers of $\beta = \pi$, 2π, 3π and 4π are shown in figure 45. For the cases at $St_L = 0.6$, the energy amplification over the cavity maintains a low magnitude, reaching only up to $\hat{E}_1 = 1000$ compared to cases with other frequencies. As the front part of the cavity ($0 \leq x/D \leq 3$) is a critical region for shear-layer roll-ups to develop, the relatively low value of $\hat{E}_1$ suggests that control with $St_L = 0.6$ may not hold sufficient control authority to change the baseline flow feature. Moreover, the distribution gradually increases from the leading edge to the trailing edge and is almost identical for the different spanwise wavenumbers, which indicates that the spanwise wavenumber has limited impact on the magnitude of the primary energy amplification for $St_L = 0.6$. For the case of $St_L = 1.2$, the overall magnitudes of $\hat{E}_1$ over the cavity are higher than those at $St_L = 0.6$. The primary energy amplification decreases as the spanwise wavenumber increases and reach their maximum values around $x/D \approx 4$.

Next, we turn our attention to the primary energy amplification at a higher frequency of $St_L = 2.49$. Compared to the previous cases at $St_L = 0.6$ and 1.2, the energy amplification exhibits a sustained profile and much higher magnitude over the cavity. The perturbations with spanwise wavenumbers of $\beta = \pi$ and 2π are especially prominent. For these cases, the primary kinetic energy amplification remains high over the entire cavity length, with its

maximum value attained around the middle of the cavity. Although the magnitudes of $\hat{E}_1$ decrease as the spanwise wavenumbers increase, they remain high ($\sim O(10^5)$) compared to the other frequencies, except for the case of $\beta = 4\pi$ with $\hat{E}_1 \approx 2500$. However, given the prominence of the $\beta = \pi$ structure in the DMD analysis of the baseline, we suspect that introducing a $\beta_c = 2\pi$ disturbance forcing may be the more effective of the two.

For the high-frequency cases of $St_L = 5.14$, the response energy significantly amplifies in the front of the cavity, but decreases past $x/D \approx 1$, becoming significantly lower in magnitude towards the rear part of the cavity. This distribution of the response kinetic energy, losing its authority in the rear part of the cavity, is suspected to be indicative of a sub-optimal control case. Other coherent structures may emerge when the response kinetic energy is weak to sustainable forcing. For this reason, it appears that such high-frequency forcing will be less effective for the suppression of fluctuations in open cavity flows.

3.4.3 Assessments of resolvent analysis based cavity flow control

Unsteady actuation is introduced in LES for the forcing frequency St_c and spanwise wavenumber β_c identified by the resolvent analysis to be potentially effective for flow modification. Because practical forcing cannot be introduced globally, local forcing is imposed along the cavity leading edge, which is where the forcing modes are concentrated as shown in figure 44(a). In the above discussion, it was revealed that forcing frequency of $St_L = 2.49$ with spanwise wavenumbers between π to 3π exhibit a sustained and high-valued response kinetic energy $\hat{E}_1$ over the cavity based on the resolvent analysis. LES are performed for these choice of parameters and some other representative cases to assess the effectiveness of the actuation setup. The resolvent analysis here aids the study by reducing the control parameter search space. We, in particular, consider forcing frequency and spanwise wavenumber in the range of $0.6 \leq St_c \leq 5.14$ and $\pi \leq \beta_c \leq 4\pi$ for the following validation LES cases. Let us note that the uses of unsteady actuation are likely be effective for many

of these cases as long as they disrupt the formation of the large-scale spanwise vortices in the uncontrolled flow. The key question here is to find the near-optimal control case, in which the forcing effect remains influential over the long cavity.

The pressure fluctuations obtained from LES of controlled flows are examined over the cavity surfaces and the shear layer. Intense pressure oscillations appear over these regions in the uncontrolled cavity flow. A number of representative controlled cases are investigated, including the controlled cases with the parameters that are identified to provide sustained forcing over the cavity by resolvent analysis. The pressure fluctuations for the controlled cases are shown in figure 46. Compared to the pressure distribution for the uncontrolled flow, we observe that some of the controlled cases show significant attenuation of the fluctuations over the shear layer and on the cavity walls.

For the control cases with $St_c = 0.6$, the pressure fluctuations are reduced over the shear-layer region and along the cavity walls compared to the uncontrolled cavity flow. Along the cavity floor, the area experiencing large pressure fluctuations are limited to the aft third of the cavity, which is reduced in size from the uncontrolled case. Above the shear layer, actuation is able to modify the flow field to reduce the spatial extent over which large fluctuations appear, but the unsteady shock-induced fluctuations remain strong over the rear half of the cavity in the case of forcing spanwise wavenumbers of $\beta_c = \pi$ and 2π. As the values of metric $\hat{E}_1$ calculated from resolvent analysis for frequency $St_c = 0.6$ are relatively low (figure 45), the discrepancy in pressure reductions among those cases from $\beta = \pi$ to 3π results from nonlinearity of the flow. Although the case with $(\beta_c, St_c) = (3\pi, 0.6)$ has a desirable control performance, this scenario may require additional guidance beyond resolvent analysis.

Next, the controlled flows with a forcing frequency of $St_c = 2.49$ are considered. All of the forcing spanwise wavenumbers of $\beta_c = \pi$, 2π, and 3π shown in figure 46 significantly reduce the pressure fluctuations over the cavity walls as well as the shear layer. Most

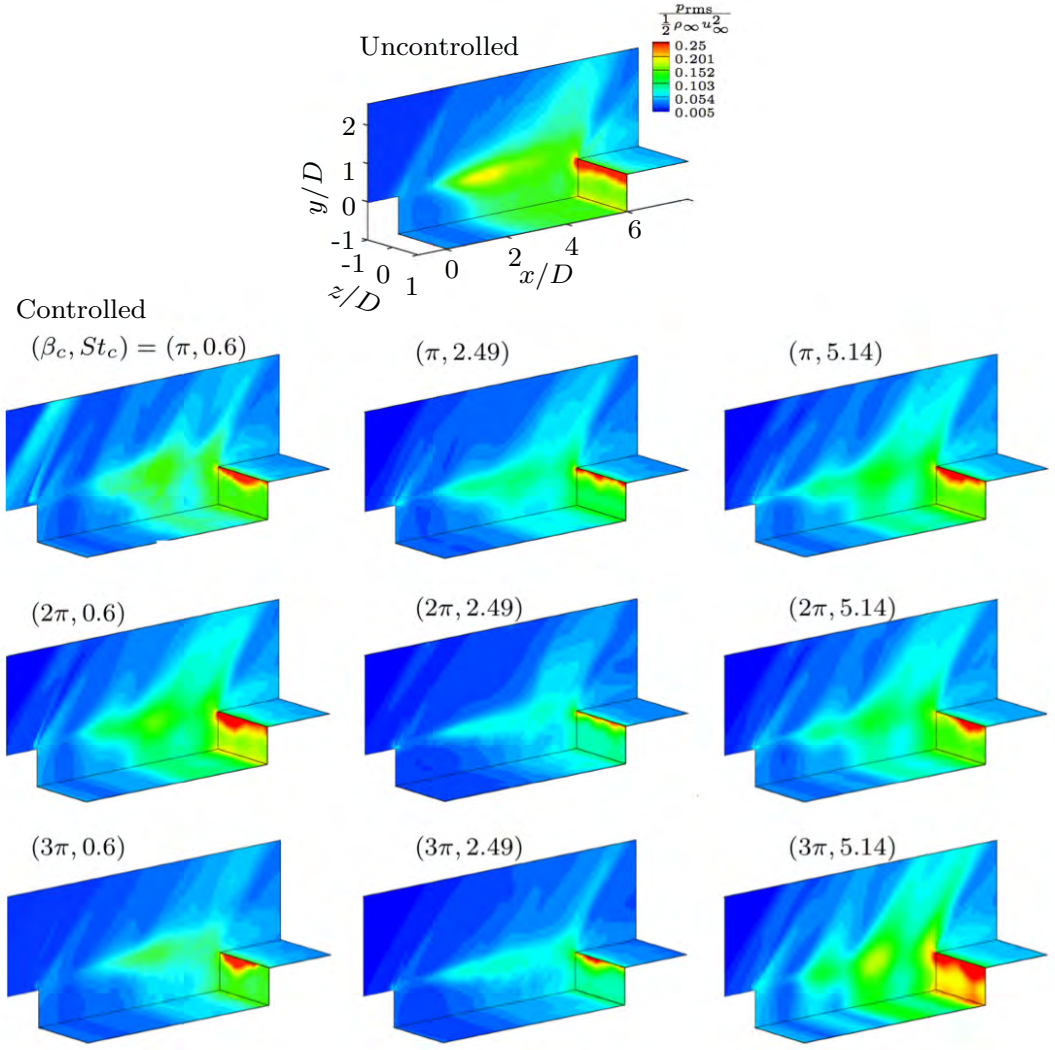

Figure 46: The rms pressure $p_{\text{rms}}/(\frac{1}{2}\rho_\infty u_\infty^2)$ over the cavity surfaces and the $x-y$ plane at $z/D = -1$ for the uncontrolled (top) and controlled cases.

noteworthy here are the cases where the spanwise wavenumbers of the forcing input are 2π and 3π. For these cases, the unsteady forcing is able to shorten the spatial (vertical) extent of large fluctuations. Due to the stabilizing effect in the shear layer and weakened impingement of flow structures, we observe remarkable reductions in the pressure fluctuations above 50% along the aft and bottom walls of the cavity (see summary in table 3). Compared to the baseline and the other controlled cases, high levels of pressure fluctuations are experienced only along the trailing edge of the cavity.

Although at $St_c = 2.49$ the metric $\hat{E}_1$ for $\beta = 2\pi$ is much higher than $\beta = 3\pi$ as shown in figure 45, similar control effectiveness in terms of the level of P_{rms} reductions suggest that the control effects are experiencing saturation due to nonlinearities at the frequency of $St_c = 2.49$. For the case of $\beta = 4\pi$, the reduction level may appear lower in value, but the E_1 value is higher than the those for the case of $St = 0.6$. The substantial reduction of pressure fluctuations over the cavity is achieved with the choice of control parameters identified from the resolvent (response mode) based kinetic energy based metric (50). This implies that the input-output relationship captured by resolvent analysis for the turbulent cavity flow can indeed point to an effective set of control parameters with significantly less computational resources than what is required by an uninformed parametric LES study.

Forcing at a frequency of $St_c = 5.14$ is also examined, which is higher than the frequency identified by the resolvent analysis. For these controlled cases, the pressure fluctuations over the shear layer are higher in magnitude compared to the cases of $St_c = 2.49$, as shown in figure 46. These results are expected as the forcing to enhance mixing across the shear layer is not as sustained as in the case of $St_c = 2.49$, which is indicated by figure 45. In fact, the unsteady control induces the appearance of oblique shocks for all spanwise wavenumber cases shown in figure 46, which renders the control counter-productive. We also observe strong impingement of vortical structures for the spanwise wavenumber of 3π, which increases the pressure fluctuations on the entire aft wall above

Cases	β_c	St_c	$\tilde{p}_{\mathrm{rms}}$	$\Delta\tilde{p}_{\mathrm{rms}}$
Baseline	-	-	1.37	-
Unsteady control	π	0.6	0.98	-28%
	π	1.2	0.85	-38%
	π	2.49	0.85	-38%
	π	3.13	0.94	-31%
	π	5.14	1.13	-18%
	2π	0.6	1.25	-9%
	2π	1.2	0.91	-34%
	2π	2.49	0.66	-52%
	2π	3.13	0.96	-30%
	2π	5.14	1.05	-23%
	3π	0.6	0.82	-40%
	3π	1.2	0.80	-42%
	3π	2.49	0.67	-51%
	3π	3.13	1.08	-21%
	3π	5.14	1.44	+5%
	4π	2.49	0.88	-36%
Steady control (Sun et al., 2019)	3π	0	0.98	-28%

Table 3: Summary of flow control cases with unsteady actuation.

that of the uncontrolled case. Note that it is not only the maximum value of E_1 but also sustained distribution (flatness) of the E_1 profile are important.

Looking closer at the flow fields for some of the cases presented in figure 46, we visualize in figure 47 the instantaneous vortical structures for effective controlled cases with $(\beta_c, St_c) = (2\pi, 2.49)$ and $(3\pi, 2.49)$ as well as an ineffective controlled case with $(3\pi, 5.14)$. Shown in this figure are the iso-surfaces of the Q-criterion colored by the pressure coefficient. For the case of $(\beta_c, St_c) = (2\pi, 2.49)$ shown in figure 47(a), small streamwise vortices are generated from the leading edge and propagate downstream, which gradually spread over the shear layer. Large-scale spanwise shear layer roll-ups disappear in the flow field compared to the uncontrolled cavity flow (recall figure **??**). The modification of the flow field produced by the unsteady actuation greatly attenuates the large-scale flow structure impingement on the aft-wall by breaking up large structures and reduces the fluctuations over the cavity. The aft wall only experiences small-scale vortical structures hitting the wall in an incoherent manner. As the kinetic energy profile (50) foreshadows, the mixing and breakup of the large-scale spanwise vortices are sustained over the entire cavity length and yield an effective control approach to reduce the pressure fluctuations.

For the controlled case with $(\beta_c, St_c) = (3\pi, 2.49)$ presented in figure 47(b), the flow structure appears similar to those from the case of $(\beta_c, St_c) = (2\pi, 2.49)$. With the choice of a high wavenumber, the structures are generated by the unsteady actuation from the cavity leading edge in a closely packed manner. These streamwise vortical structures appear to cancel the vortical influence from each other due to their close proximity and cannot suppress the spanwise instability from appearing as effectively as the case with $(\beta_c, St_c) = (2\pi, 2.49)$. This leads to a correspondingly larger fluctuations over the cavity and local thickening of the shear layer, as visualized by the wider range of pressure values in figure 47(b).

For the case of $(\beta_c, St_c) = (3\pi, 5.14)$ shown in figure 47(c), the streamwise vortices

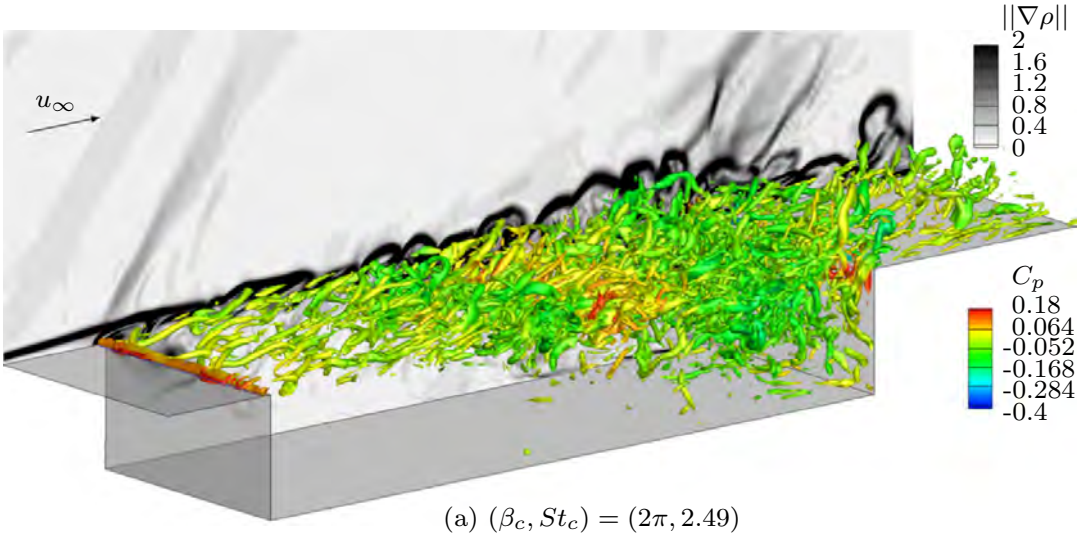

(a) $(\beta_c, St_c) = (2\pi, 2.49)$

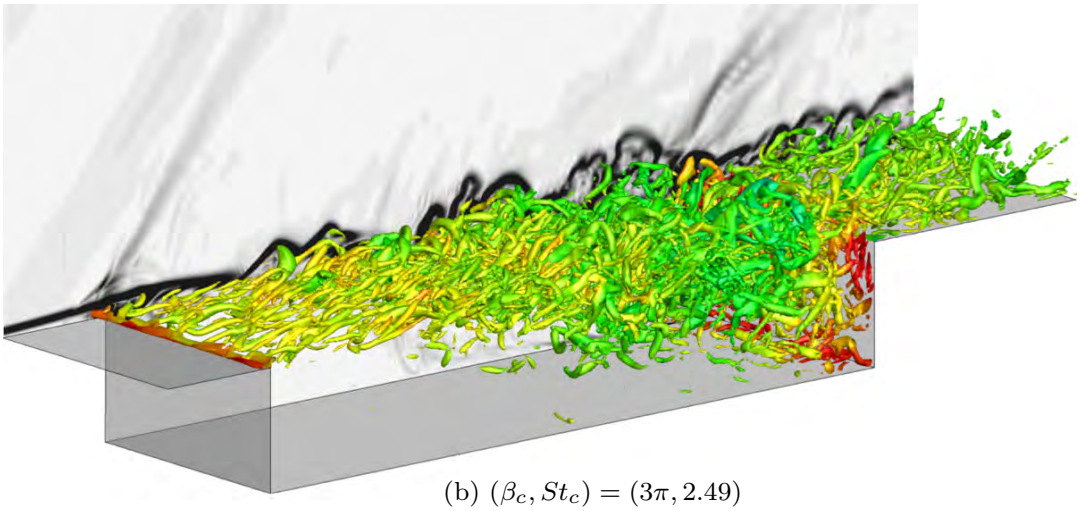

(b) $(\beta_c, St_c) = (3\pi, 2.49)$

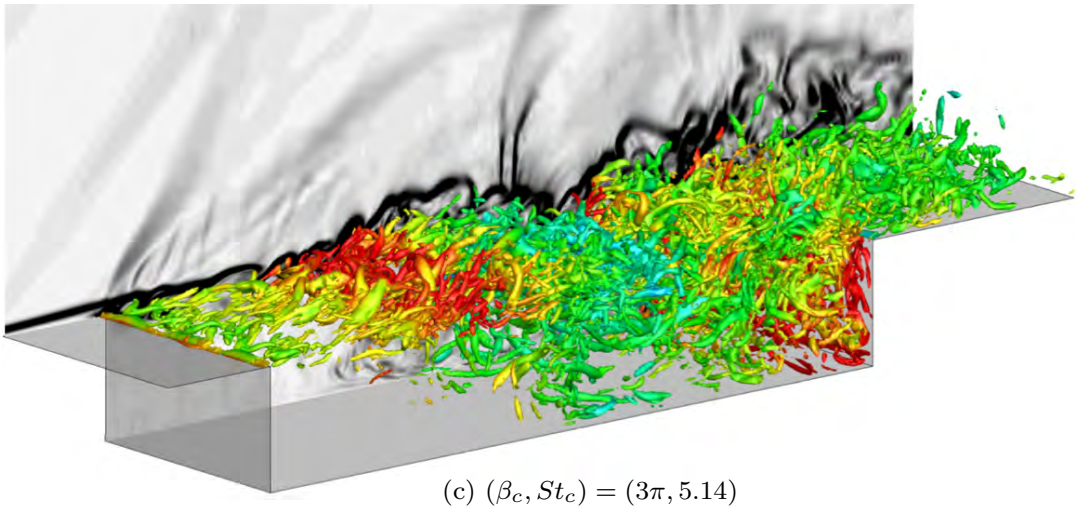

(c) $(\beta_c, St_c) = (3\pi, 5.14)$

Figure 47: Instantaneous controlled cavity flows with (a) $(\beta_c, St_c) = (2\pi, 2.49)$, (b) $(3\pi, 2.49)$ and (c) $(3\pi, 5.14)$, visualized with the Q-criterion $Q(D/u_\infty)^2 = 10$ colored by $C_p = (p - p_\infty)/(\frac{1}{2}\rho_\infty u_\infty^2)$ at $M_\infty = 1.41$. Numerical schlieren is shown in the background in gray scale.

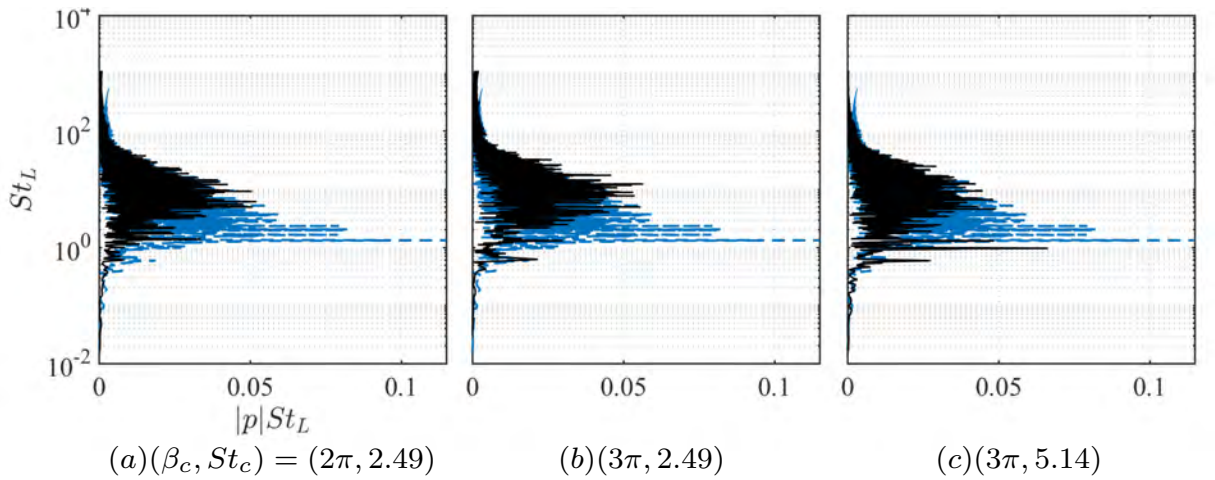

Figure 48: Pre-multiplied pressure spectra at mid-cavity along the shear layer for the controlled flows shown in black. The baseline spectra are shown by the blue dashed lines.

generated from unsteady actuation are truncated to become shorter than what are observed for the lower frequency actuation. By the middle of the cavity, the shear layer rolls up into a spanwise vortical coherent structure with a size comparable to the cavity depth that penetrates both into the freestream and the cavity. The local obstructions of the incoming flow by these large-scale vortical structures lead to the appearance of strong compression waves, adding to the increased pressure fluctuations over the shear layer and along the cavity walls. Compared to the other controlled cases, strong acoustic waves emitted from the leading edge of the cavity are observable.

The pre-multiplied pressure spectra visibly exhibit significant pressure fluctuation reductions for the controlled cases, as shown in figure 48. For the two effective control cases of $(\beta_c, St_c) = (2\pi, 2.49)$ and $(3\pi, 2.49)$, the actuation inputs successfully suppress the tone at $St_L = 1.33$ in the baseline case and reduce the turbulent pressure fluctuations. Even with a slight magnitude increase at $St_L = 0.6$ for the case of $(3\pi, 2.49)$, the actuation effectively suppresses the overall pressure fluctuations due to the substantial reduction of magnitude over other frequency bands. For the ineffective case of $(3\pi, 5.14)$, the actuation suppresses the tone at $St_L = 1.33$. However, the apparent increase of pressure fluctuations

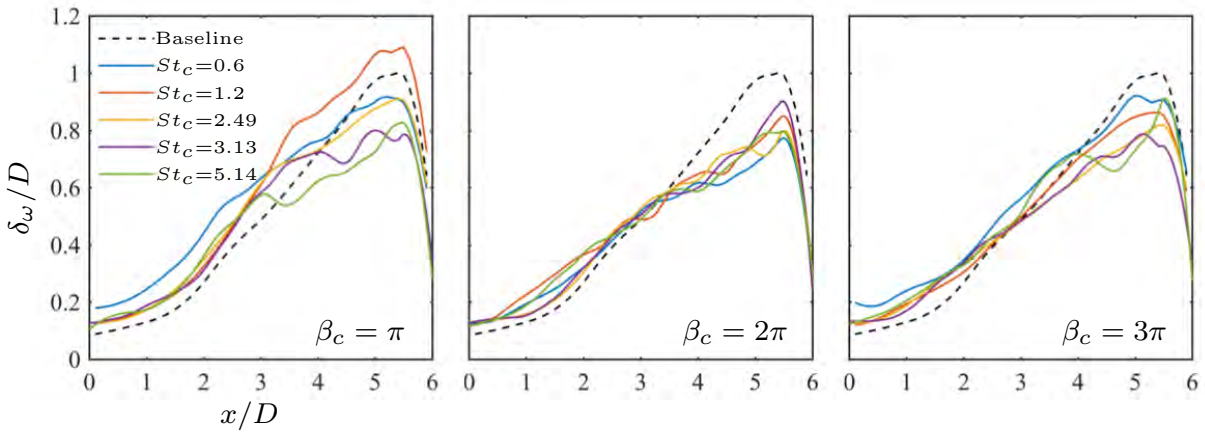

Figure 49: Vorticity thickness δ_ω for the uncontrolled and controlled cases.

over the frequency band of $St_L < 1$ gives rise to strong oscillations over the cavity. Those strong oscillations with $St_L < 1$ are associated with the larger vortical coherent structures and results in ineffective control outcome.

It is observed above that the control input influences the shear-layer thickness and consequently the pressure fluctuation level. For this reason, the vorticity thickness

$$\delta_\omega = \frac{u_\infty}{(\partial \bar{u}/\partial y)_{\max}} \tag{51}$$

is considered to quantify the direct influence of the unsteady actuation on cavity flow. Here, $\bar{u}$ is the spanwise and time-averaged streamwise velocity. Figure 49 shows the vorticity thickness of the shear layer from controlled cases at spanwise wavenumbers of $\beta_c = \pi, 2\pi$, and 3π. For the controlled cases, δ_ω is thicker at the leading edge compared to the uncontrolled case. This local thickening of the shear layer at the leading edge reduces its receptivity to the acoustic disturbances and stabilizes the shear layer as it advects downstream. For the cases of $\beta_c = 2\pi$, a significant reduction of vorticity thickness is observed in the rear part of the cavity. Note that the sudden decrease in the vorticity thickness near the trailing edge is due to the effect of impingement on the cavity trailing edge.

The magnitude of pressure fluctuations inside the cavity is coupled with the pressure fluctuations occurring above the shear-layer region. We quantify the control effectiveness by

integrating the pressure fluctuations over the floor and aft-wall of the cavity using equation (4). The unsteady control cases in general achieve significant reductions of pressure fluctuations compared to the uncontrolled case. Particularly noteworthy is the control case with $(\beta_c, St_c) = (2\pi, 2.49)$ which achieves 52% reduction in the pressure fluctuations, as summarized in table 3. Additionally, the present unsteady control substantially outperforms our previous control efforts using steady three-dimensional actuation (Sun et al., 2019). The trends summarized in table 3 are consistent with the predictive metric for control design, which validates the conceptual approach of how to use the results of the resolvent analysis to determine an effective unsteady flow control setup.

3.4.4 Dynamic mode decomposition of the controlled flows

Let us further assess the influence of unsteady actuation on the turbulent cavity flow using DMD analysis. Here, the DMD analysis serves as an a posteriori analysis of the nonlinear flow with control to assess the control effectiveness and is not meant to provide any direct comparison with resolvent analysis. We extract the coherent structures produced at the forcing frequency to examine the persistence of forcing input (perturbation) from the leading edge of the cavity. Here, the DMD analysis extracts the key flow response structures around the optimal control case for the forcing frequency of $St_c = 2.49$ with spanwise wavenumbers of $\beta_c = \pi$, 2π and 3π. Presented in figure 50 are the spatial structures of the spanwise velocity associated with the forcing frequency of $St_c = 2.49$. We also note in passing that, while not shown, the DMD modes are in good agreement with spectral POD modes (Schmidt et al., 2017; Schmidt and Colonius, 2020b) extracted from the controlled flows. By examining the spatial evolution of the DMD modes over the cavity, we can understand the mechanism by which the forcing input prevents the undesirable large-scale vortex roll-up from appearing over the cavity.

Consider the controlled flow case of $\beta_c = \pi$, shown in figure 50(a). This forcing

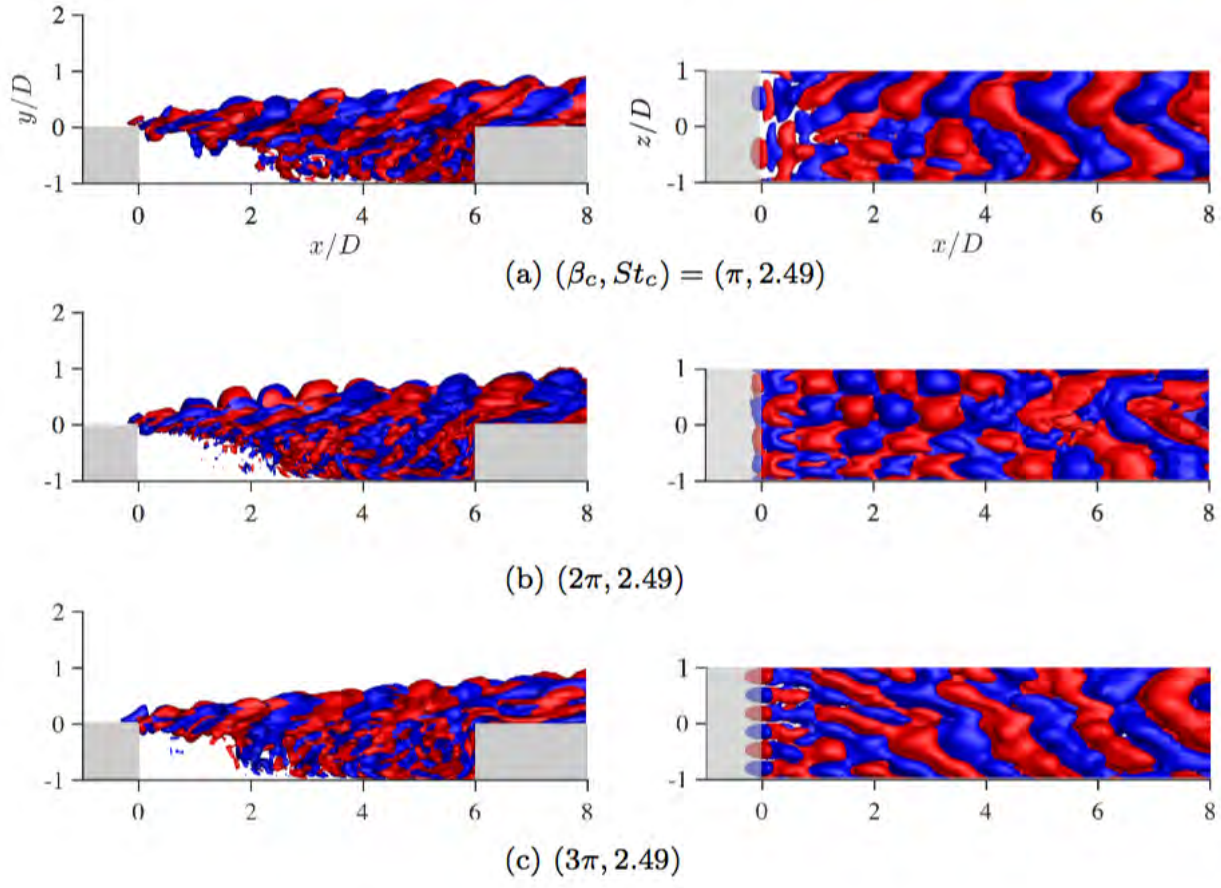

Figure 50: Side and top views of the real spanwise velocity of DMD modes for the control cases. Iso-surface values of streamwise velocity are 0.1 (red) and −0.1 (blue).

wavenumber is the same as the dominant spanwise wavenumber observed in figure ?? for the uncontrolled flow. From the top view in figure 50(a), we notice that the flow structures essentially maintain the spanwise wavenumber of $\beta = \pi$, except for some regions over $1 \lesssim x/D \lesssim 3$ due to nonlinear interactions. The fact that $\beta = \pi$ remains the primary wavenumber indicates that the control is ultimately unable to fully attenuate the undesirable fluctuations.

For the case of controlled flow with $\beta_c = 2\pi$, shown in figure 50(b), we observe that the flow structures predominantly possess the spanwise wavenumber of $\beta = 2\pi$ almost over the entire cavity ($x/D \lesssim 6$). This means that the actuation is able to attenuate the undesirable large-scale unsteady vortical structure with $\beta = \pi$. As discussed earlier, the flow control input for this flow produces a range of small-scale structures, reducing the spatial fluctuation level over the shear layer. This modification of the flow in turn avoids the generation of unsteady oblique shock waves over the cavity.

For the higher control input wavenumber of $\beta_c = 3\pi$, we observe the finer structures introduced from the leading edge of the cavity, as seen in figure 50(c). As the flow convects downstream, the spanwise vortical structures start merging past $x/D \approx 2$. Once this spanwise merging process takes place, the flow relaxes back to the large-scale structures with $\beta = \pi$. However, full relaxation does not appear until $x/D \approx 3$, which allows the flow to delay the formation of the large-scale structures. From the insights gained through the DMD-based analysis, we can assess the spatial extent over which the actuation input remains effective. The present DMD analysis confirms that the choice of $(\beta_c, St_c) = (2\pi, 2.49)$ is indeed a good choice for attenuating fluctuations generated in the present supersonic turbulent cavity flow.

3.5 Passive Tabs

The control strategy in the current work is inspired by and builds upon the work of Lusk et al. (2012); therefore, all control methodologies have been designed for the same spanwise wavelength of $\overline{\lambda} = 1$, which was deemed the best of the cases in their study. This choice of $\overline{\lambda}$ is in agreement with resolvent analysis conducted on cavities with $L/D = 6$ in Liu, Sun, Yeh, Ukeiley, Cattafesta, and Taira (Liu et al.).

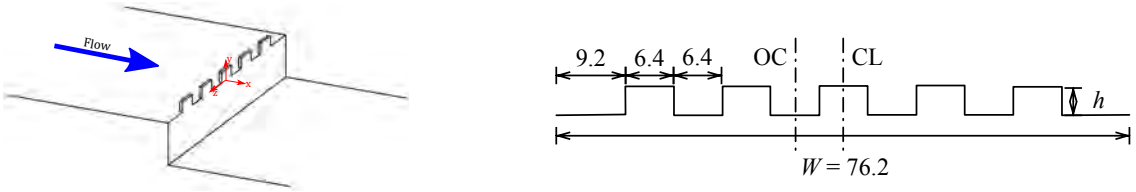

(a) Leading edge tab array location

(b) Leading edge tab array dimensions

Figure 51: A spanwise array of leading-edge tabs with $\overline{\lambda} = 1$ that protrude into the approaching boundary layer by a height h. (dimensions in mm). CL: centerline of the tabs ($z/D = 0$), OC: off-centerline i.e. between two tabs ($z/D = 0.5$)

For controlling the flow, spanwise-arranged leading-edge tabs with a thickness of 1.6 mm were manufactured which was equivalent to the blowing slot thickness in Lusk et al. (2012). Three different heights h of δ, $\delta/2$, and $\delta/4$ were considered in the current study and were flushed with the front face of the leading edge, as shown in Fig. 51(a). Each of the tab configurations were machined into their own leading edge block making them fully integrated to the cavity structure. The origin is chosen to coincide with the midspan at the lip line of the cavity leading edge as can be seen in the figure. The figure also shows the chosen axes directions with the zero being at the midspan of the tunnel on the cavities leading edge. Bending analysis on the tabs using SolidWorks revealed a minimum factor of safety value of 5.46 with the tabs most likely to fail. Also, experiments confirmed that the

tabs did not deflect due to the flow. The spanwise profile of the tabs with dimensions can be seen in Fig. 51(b). For comparison, seeded actuator imaging of the best blowing case (maximum rms pressure reduction) of leading-edge slots reported in Lusk et al. Lusk et al. (2012) were conducted. For this purpose, the flow to the slots were seeded with DEHS oil and a Uniphase HYBRID B2.3 532 nm continuous wave laser was used for illumination. Imaging was done using an X-stream XS-5 camera with a resolution of 1280×1024 fitted with a 200 mm lens to capture zoomed in images of the penetrating jet. A scaling was performed before taking flow images to relate pixel dimensions to physical dimensions resulting in a spatial resolution of 0.06 mm per pixel. A total of 100 flow images were averaged to get the approximate penetration height. Figure 52 showed the outer edge of the penetrating jet, the height of which was found to be around 0.8 mm which corresponds closest to the $\delta/4$ tabs (see Fig. 52).

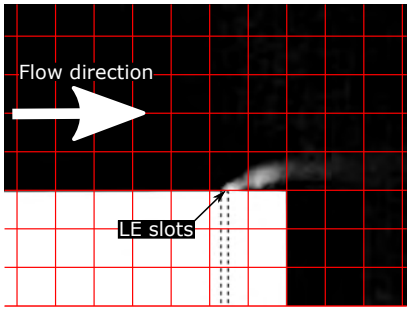

Figure 52: Seeded blowing actuation penetrating into the boundary layer flow captured in images. Spacing between grid lines represents a length of 1 mm in each direction. The cavity leading-edge block is represented in white color and location of leading-edge slots is represented by dashed black lines.

Kulite piezoresistive pressure transducers were installed along the cavity center span at two locations on the cavity floor and at one location on the cavity aft wall. Table 4 gives details about the Kulites installed. For convenience of representation in subsequent text,

the two locations on the cavity floor ($y/D = -1$) will be referenced by their x/D value and the one located at $x/D = 6$ and $y/D = -0.5$ will be referenced as aft wall.

Table 4: Location of Kulite transducers

Sensor location	x/D	y/D	Model number
Front floor	1.5	-1	XCS-062-5D
Rear floor	5.25	-1	XCQ-062-0.35BARD
Aft wall	6	-0.5	XCQ-062-50A

Power spectral density (PSD) plots of surface fluctuating pressure are compared at three locations (see Table 4) for the baseline and controlled cases as shown in Fig. 53. Reduction in tonal amplitudes are observed with all tab configurations, while reduction in broadband contents are achieved with tabs of heights $\delta/4$ and $\delta/2$. Out of all tabs employed in the current work, tabs of height $\delta/4$ are the most effective. The tallest tab height (δ) presents an interesting result since they essentially eliminate the resonance tones. However, they are not effective at eliminating broadband contents as the other two tabs ($h = \delta/2$ and $\delta/4$) and even increase the broadband level compared to the baseline cavity at $x/D = 1.5$. This results in their overall reductions being significantly less.

As noted previously, the most effective control has a tab height of $\delta/4$, which is the closest to the penetration height of best blowing case of mass injection arrangement of the same spanwise wavelength. When compared with mass injection in Lusk et al. (2012), it is revealed that both tabs and mass injection are capable of suppressing broadband and tonal pressure fluctuation amplitudes over the entire spectrum at similar levels. Table 5 shows summary of overall pressure reductions at various locations on the cavity floor for the installed tabs and compares with findings from blowing in Lusk et al. (2012). Both the spanwise-arranged $\delta/4$ tabs (passive control) and mass injection (active control) reduce

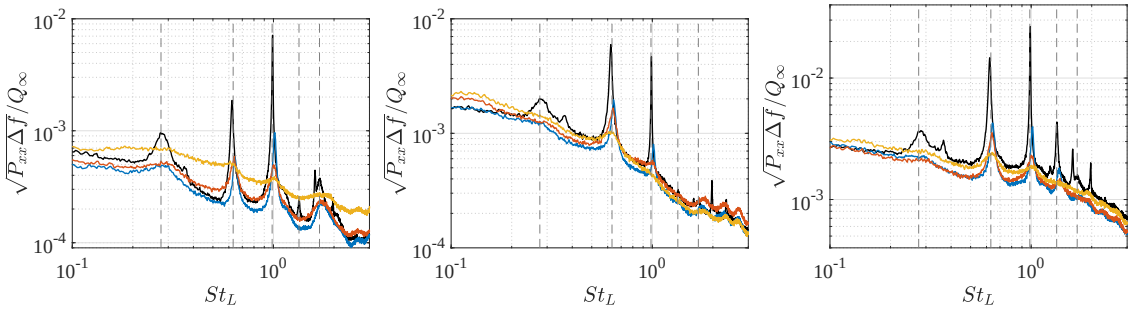

(a) $x/D = 1.5$ (b) $x/D = 5.25$ (c) Aft wall

Figure 53: Pressure fluctuation PSD of baseline compared with tabs of different heights. −: baseline; −: $h = \delta/4$; −: $h = \delta/2$; and −: $h = \delta$. Dashed-lines are tonal frequency predictions using $St_L = (n - \alpha)/(1/\kappa + Ma_\infty/\sqrt{1 + (\gamma - 1)Ma_\infty^2/2})$ (Heller and Bliss, 1975), where $\alpha = 0.22$ and $\kappa = 0.61$ were determined by a least-squares fit.

rms pressure fluctuations on the cavity surfaces by similar amounts, indicating that passive control using tabs of a height similar to penetration height of the steady active control can effectively replace them for controlling cavity oscillations under the current flow conditions. To this end, flow field measurements for $\delta/4$ tabs are conducted to further elucidate flow phenomena that may be responsible for its effectiveness.

Table 5: Summary of rms pressure reductions

Control	$x/D = 1.5$	$x/D = 5.25$	Aft wall
δ tabs	23.0 %	9.3%	34.1 %
$\delta/2$ tabs	40.9 %	15.9 %	40.6 %
$\delta/4$ tabs	46.5 %	30.6 %	40.3 %
Blowing(Lusk et al., 2012)	41.0 %	N.A.	44.0 %

After determining the efficacy of the passive tabs of height, $\delta/4$, flow field measurements were conducted to understand associated flow phenomena that lead to effective flow control. To this end, two-component PIV and stereoscopic PIV measurements were conducted on

streamwise aligned and cross-stream aligned measurement planes respectively. The two PIV setups (two-component and stereoscopic) are shown in Figure 54.

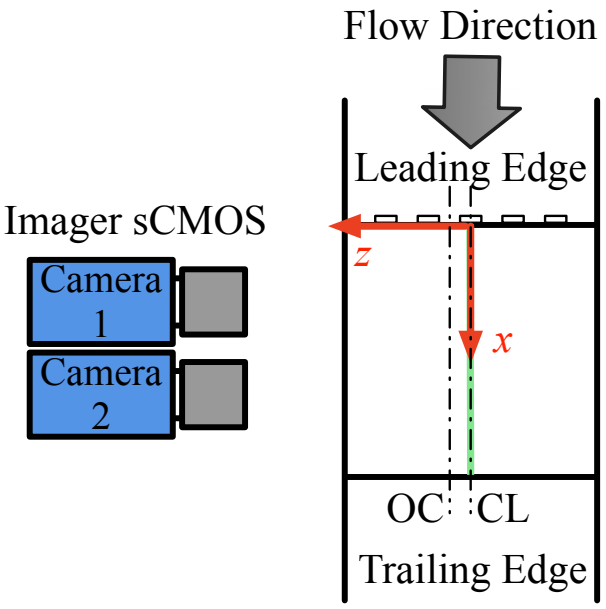

(a) Two-component streamwise-aligned PIV

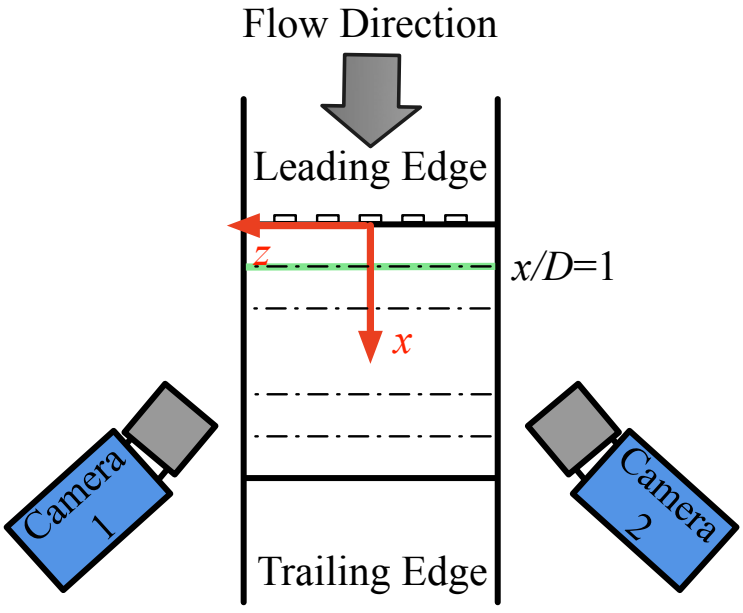

(b) Cross-stream stereoscopic PIV

Figure 54: Schematics of different PIV setups with dashed lines indicating the locations of the measurement planes.

For the two measurements, the flow was seeded with DEHS oil using a LaVision four-nozzle atomizer that produced seeding particles with mean diameter of 1μm as specified by the vendor. A Litron Nano L 135-15 Nd:YAG laser was used to illuminate the particles. The laser optics were adjusted to create a laser sheet of thickness 1mm and 3mm for two-component and stereoscopic PIV respectively. Two Imager CMOS cameras were used with each camera having a resolution of 2560 by 2160 pixels with a 16 bit digital output. The cameras were double exposure and the whole arrangement operated at a sampling rate of 12 Hz to produce PIV image pairs. The cameras were fitted with Sigma 105 mm EX DG Macro lenses for planar PIV setup and Nikon 60 mm AF Micro-Nikkor lenses for stereoscopic PIV setup. An anodized cavity floor was used to reduce laser reflections in the PIV images. To further minimize laser reflections from the cavity surfaces, the cameras were fitted with 532 nm bandpass filters and the cavity surfaces were treated with rhodamine paint before conducting PIV measurements.

For two-component PIV measurements, two cameras were placed side-by-side with a slight overlapped field of view to improve resolution in the streamwise direction (see Figure 54(a) for details). The final velocity vectors obtained from the two camera images were merged using a stitching algorithm in DaVis 8.4 software. A total of 1500 image pairs were acquired for this setup. For stereoscopic PIV, the two cameras were used in a Schiempflug arrangement so that each camera looked into the cavity measurement plane at an angle varying between $40 - 50$ degrees from the flow direction (see Figure 54(b) for details). Calibration for stereoscopic PIV was conducted using a custom-made, two-level calibration plate described in June et al. (2017). An additional step of self-calibration is performed for stereoscopic measurements to correct potential misalignment of the laser sheet. A total of 2000 image pairs were acquired for these measurements.

Processing of the PIV data was conducted using the DaVis 8.4 software. First a Gaussian time filter was applied to each image to remove any background noise. Preprocessing

was then performed using a sliding background subtraction routine to remove any undesirable reflections from the cavity surfaces. Two initial passes with interrogation windows of size 64×64 and then three further passes with interrogation windows of size 32×32 were conducted to obtain velocity fields. For post-processing, universal outlier detection was conducted using DaVis 8.4 software followed by multi-variate outlier detection (MVOD) (Griffin et al., 2010). Since the streamwise measurements had significantly higher reflections, an additional pass of universal outlier detection (Grafarend, 2006) was performed in MATLAB before conducting MVOD. PIV uncertainties were calculated directly by the DaVis software which is based on correlation statistics (Wieneke, 2015) was found to remain below 3 % of the measured freestream velocity for all velocity components.

Two-component PIV measurements were conducted in planes aligned with the streamwise direction shown as a dashed lines in Fig. 54(a). Centerline plane measurements have been abbreviated as 'CL' and off-centerline measurements abbreviated as 'OC'. One laser plane (CL) for baseline and two laser planes (CL and OC) for the $\delta/4$ tab configuration are considered. In all plots a small strip of the flow field adjacent to the cavity floor has been masked out to remove spurious vectors resulting due to glare from the surfaces and build up of oil. To counteract the effects of reflections in PIV snapshots in one of the cases (Tabs - CL) and also slight discontinuities in the stitching process for all three cases, some of the points in the flowfield have been interpolated using natural neighbor interpolation for better visualization. It is to be noted that this is only being done as we are not using the flowfields to estimate anything quantitative and use it only for comparisons in a qualitative manner.

Figure 55 shows ensemble-averaged u-velocity contour plots with mean velocity vectors overlaid. The baseline cavity flow field is consistent with previous measurements of the flow field in Dudley and Ukeiley (2014) and Lusk et al. (2012). There are significant differences between the baseline and the controlled flow mean characteristics. Compared to the baseline

flow, for the controlled flow, lifting of the shear layer is visually apparent in the CL plane of the tabs. In the OC plane, an initial dip in the mean streamwise flow field is observed, implying the flow reaches deeper into the cavity, which is followed by lifting of the shear layer flow downstream. These observations are consistent with mass injection control in Lusk et al. (2012). The $u-v$ vector plots for baseline flow indicate a large mean circulation region that extends over the majority of the cavity. Similar large recirculation regions are observed for baseline cavity flow for supersonic flow in Zhuang et al. (2006) and subsonic flow in Murray et al. (2009). Vector plots of the mean velocity for the controlled flow show significant differences as the flow approaches the aft wall from that of the baseline case. Both planes show a recirculating region sitting about half way up the rear wall leading to an apparent ejection of flow over that wall. This flow is likely fed from the outer sides of the cavity and is consistent with the results presented in Dudley and Ukeiley Dudley and Ukeiley (2014), where the predominant fluctuating pressure suppression mechanism was lifting of the cavity shear layer.

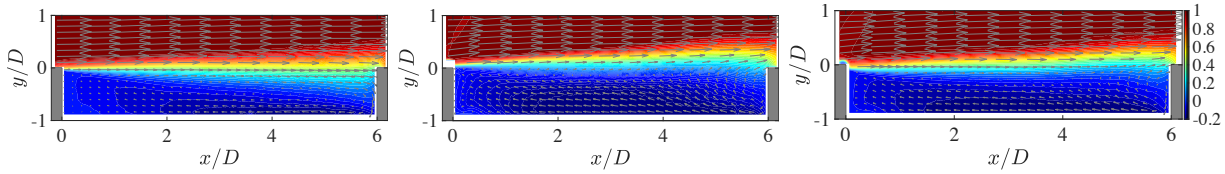

(a) Baseline (b) Tabs - CL (c) Tabs - OC

Figure 55: $\bar{u}/U_\infty$ velocity field of the baseline and controlled ($\delta/4$ tabs) cavities on streamwise-aligned planes.

Contour plots for the rms of the wall-normal velocity fluctuations are presented in Fig 56. In comparison to the baseline flow, the high rms region for the controlled flow are seen to be lifted out of the cavity in CL, as well as OC planes. Further, the high rms region for CL planes are lifted more than those in the OC planes. The amplitudes of the fluctuating components are seen to be slightly higher in the controlled flow than the baseline flow

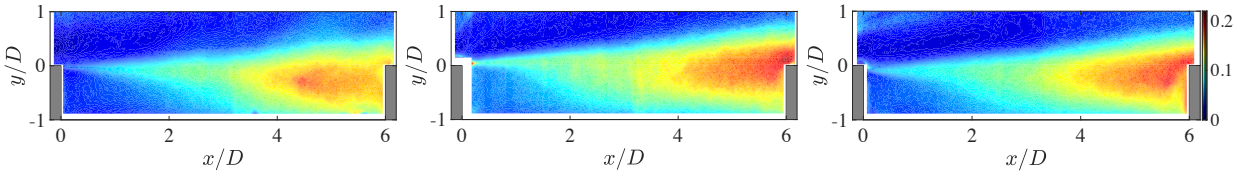

(a) Baseline (b) Tabs - CL (c) Tabs - OC

Figure 56: v_{rms}/U_∞ velocity field of the baseline and controlled ($\delta/4$ tabs) cavities on streamwise-aligned planes.

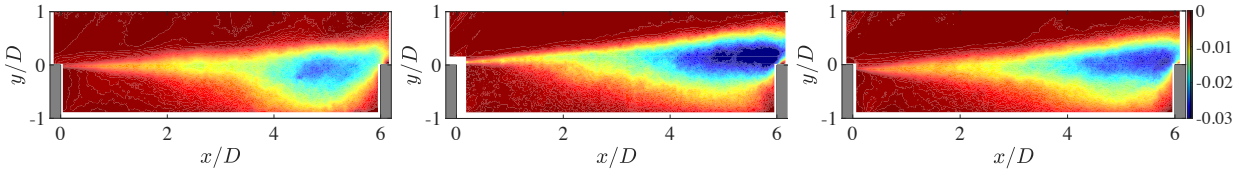

(a) Baseline (b) Tabs - CL (c) Tabs - OC

Figure 57: $\overline{u'v'}/U_\infty^2$ field of the the baseline and controlled ($\delta/4$ tabs) cavities on streamwise-aligned planes.

which is consistent with observations in Lusk et al. (2012) and Arunajatesan et al. (2009). The $\overline{u'v'}$ component of the Reynolds Shear Stress (RSS) have also been plotted in Fig 57. It shows the flow with high energy turbulent levels being pushed out of the cavity for both the CL and OC planes of controlled flow similar to that indicated in Fig 56.

Stereoscopic PIV measurements were acquired on cross-stream aligned measurement planes. Measurements were taken on 4 planes in this orientation located at $x/D = 1$, 2, 4, and 5. (The plane at $x/D = 3$ is not considered due to geometrical constraints with the cavity leading/trailing edges obstructing the camera view.) In the spanwise direction, the field of view encompasses the region where the five controlled structures are present, spanning a width of $4.5D$ out of the cavity full span ($6D$). This ensures that the physically important features are captured and unreliable regions near the sidewalls of the cavity and top of the test section are removed from the displayed flow field. The location of the tabs have been traced in each of the controlled velocity plots for reference.

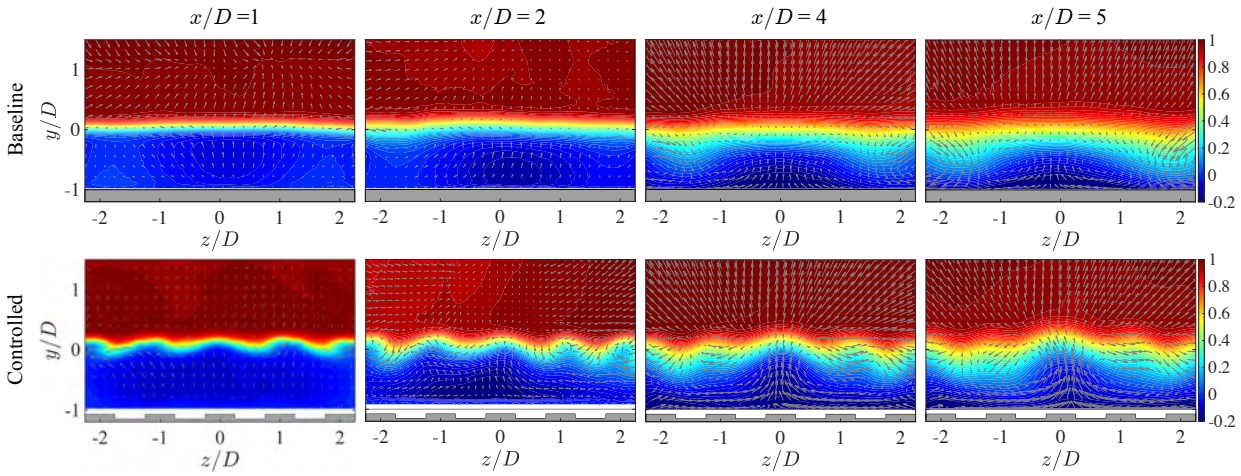

Figure 58: $\bar{u}/U_\infty$ flow field with contours representing the streamwise velocity overlaid with mean velocity vectors in the cross-stream $(y-z)$ plane for the baseline and controlled ($\delta/4$ tabs) cases.

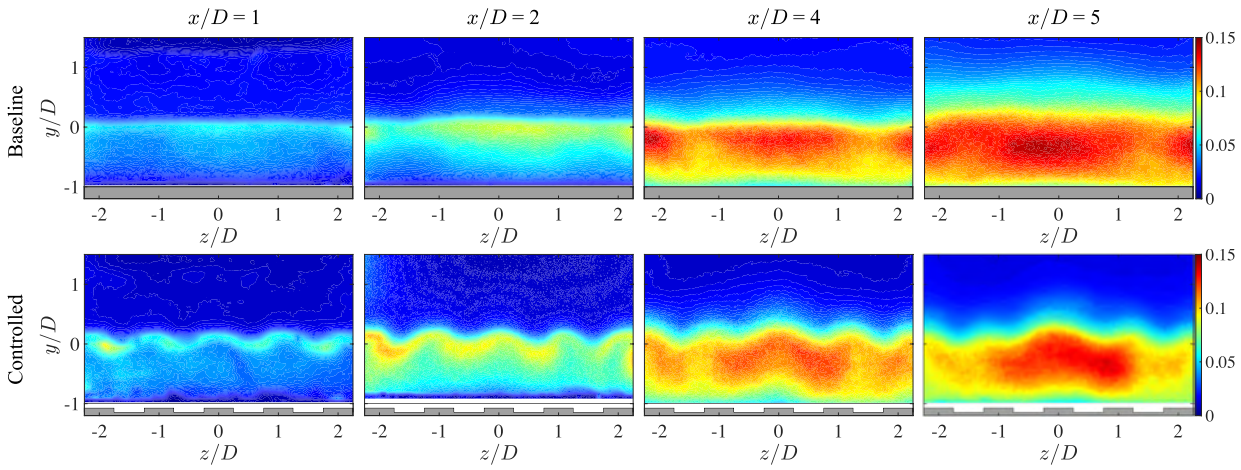

Figure 59: v_{rms}/U_∞ velocity fluctuation in cross-stream aligned planes at various streamwise locations for baseline and controlled ($\delta/4$ tabs) cases.

Figure 58 shows the mean flow field of the stereoscopic PIV measurements for planes at the various streamwise locations comparing the baseline with the controlled ($\delta/4$ tabs) flow. The color contours represent the u-velocity component, while the velocity vectors represent the v and w components in the respective $y-z$ plane. Focusing on the baseline case, the shear layer grows as the flow moves downstream with the shear layer penetrating deeper into the cavity. This increases the interaction of the flow with the cavity floor and results in amplified pressure fluctuations on the cavity floor. The vortical structures in the cavity shear layer at the downstream end around $z/D = \pm 1.5$ close to the sidewalls are consistent with observations in Lusk et al. (2012). Wall-normal mean velocity components around $y/D = 0$ indicate vectors pointing upwards in the cavity shear layer for upstream locations and downward pointing vectors for the downstream locations. This is indicative of a large recirculation region present in the baseline cavity observed in the streamwise plane. This is also consistent with Lusk et al. (2012).

The controlled flow shows presence of a spanwise waviness pattern that scales with the size of the tabs with the flow pushing up behind the tabs and pushing down between the tabs. This is consistent with results in the previous subsection where the measurements on the CL plane (behind the tabs) showed higher lifting than the OC plane (between the tabs). Downstream, these structures grow wider in the $y-$direction and enhance overall mixing of the flow. In addition, as the flow moves downstream, these patterns become more diffused (less sharply defined) which may be due to closeness of the tabs where the vortices produced by the tabs have more time to diffuse or mix. The flow features in all planes considered are very similar to those observed in mass injection active control in Lusk et al. (2012). At $x/D = 5$, counter-rotating vortical structures are observed near the edges of the mid tab (on either side) centered around $y/D = -0.4$, similar to that observed for spanwise-arranged mass injection control in Lusk et al. (2012). Overall, the shear layer is observed to be lifted out of the cavity at the cavity midspan ($z/D = 0$).

Figure 59 shows rms contour plot of wall-normal velocity fluctuations at various streamwise locations for the baseline and controlled flows. The rms fields show lower magnitudes for upstream locations in baseline cavity. As the flow moves downstream, higher magnitudes are observed which penetrate deeper into the cavity due to the growing shear layer. Also, the plots reveal regions with higher fluctuations close to the cavity sidewalls, showing significant sidewall interaction, and also near the cavity midspan. In the controlled flow, the peaks and dips describing the wavy nature of the flow are evident in the upstream part of the cavity. However, as the flow moves downstream, the flow mixes significantly, observed by the fading distinction between the peaks and the dips. In comparison with the baseline flow, rms values closer to the cavity floor are lower in magnitude, which shows that the control has been successful in lifting the flow along the cavity span to reduce fluctuations near the cavity floor. Also, overall the amplitude of the fluctuating components is lower for the controlled flow, especially in the downstream half of the cavity. These observations are similar to observations made for mass injection in Lusk et al. (2012). Proper Orthogonal Decomposition (POD) was first introduced to the turbulence community by Lumley **?** as a method to reduce a complex flow into coherent structures that are easier to analyze and draw conclusions from. When applied to a velocity field, POD seeks basis functions that maximize its turbulent kinetic energy. When the available flow field measurements are uncorrelated in time (as is the present case), a two-point velocity correlation tensor is used as its kernel Berkooz et al. (1993). The POD technique can be used to efficiently characterize flow fields by describing them using a set of basis functions that are orthonormal in nature. The basis set is composed of a series of eigenvalues, λ, which represent weights of the modes (representative of the energy contained in the various modes), and eigenvectors, Φ, which represent the spatial distribution of these modes. Over the years, different variants of the POD technique have been applied. The POD technique has been successfully applied in numerous experimental studies on cavity flows such as Murray et al.

(2009) and Singh and Ukeiley (2020) highlighting different features of the flow in a reduced form. In the current work, the snapshot POD method introduced by Sirovich (1987) is used which is computationally more efficient because the eigenvalue problem is of the order of number of snapshots and not grid locations. This method has shown to be equivalent to the classical POD model by Lumley provided sufficient number of snapshots are used in computing the modes. Here, POD has been used as an effective tool to break down complex flow phenomena associated with the baseline and controlled flows to get a better understanding of dominant unsteadiness in each flow.

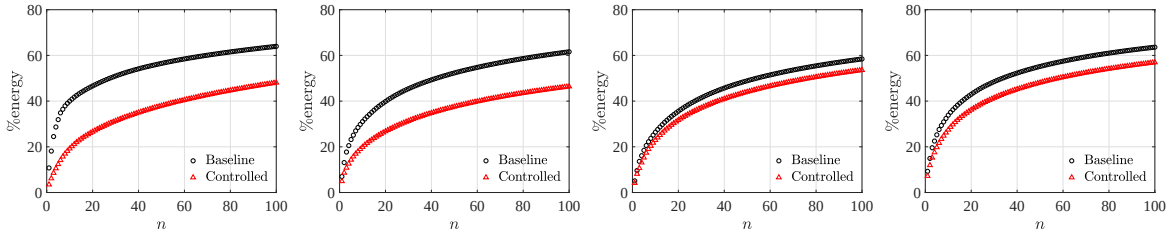

(a) $x/D = 1$ (b) $x/D = 2$ (c) $x/D = 4$ (d) $x/D = 5$

Figure 60: Eigenvalue convergence for stereoscopic PIV measurements at various streamwise locations for the baseline and controlled ($\delta/4$ tabs) cases.

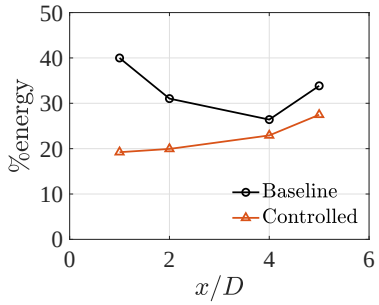

Figure 61: Accumulated percentage energy for the first 10 POD modes of baseline and controlled ($\delta/4$ tabs) flows vs. streamwise distance.

Figure 60 compares the eigenvalue convergence of baseline with the controlled flow at the various cross-stream aligned planes which is representative of the energy level in

each mode. At all streamwise locations, the convergence of modes of the controlled flow is slower than for the baseline cavity flow. This provides evidence of redistribution of energy in the controlled flow since there is more energy contained in the higher modes, i.e., smaller structures. Figure 61 compares the trend of cumulative energy percentage captured by the first 10 POD modes with the streamwise distance for the baseline and controlled flows separately. The baseline case shows that the dominant modes capture a significant fraction of the total energy at the upstream locations in the cavity. The energy captured by leading modes decreases as the flow moves downstream ($x/D = 2, 4$). However, between $x/D = 4$ and 5, the energy captured by the dominant modes significantly increases. Since the energy of the leading POD modes jumps, this indicates sudden growth of high energy events in the flow. This is a possible indication of amplification of inherent instabilities in the downstream region of the cavity, which has been noted in biglobal stability analysis conducted for cavity flows of $L/D = 6$ in Sun et al. (2017a). For the controlled flow, the control introduced small structures into the flow near the leading edge so the mode energy is lower. These structures grow larger (in size and energy) as they convect downstream, which is confirmed by the monotonic increase in mode energy with streamwise distance for the controlled flow.

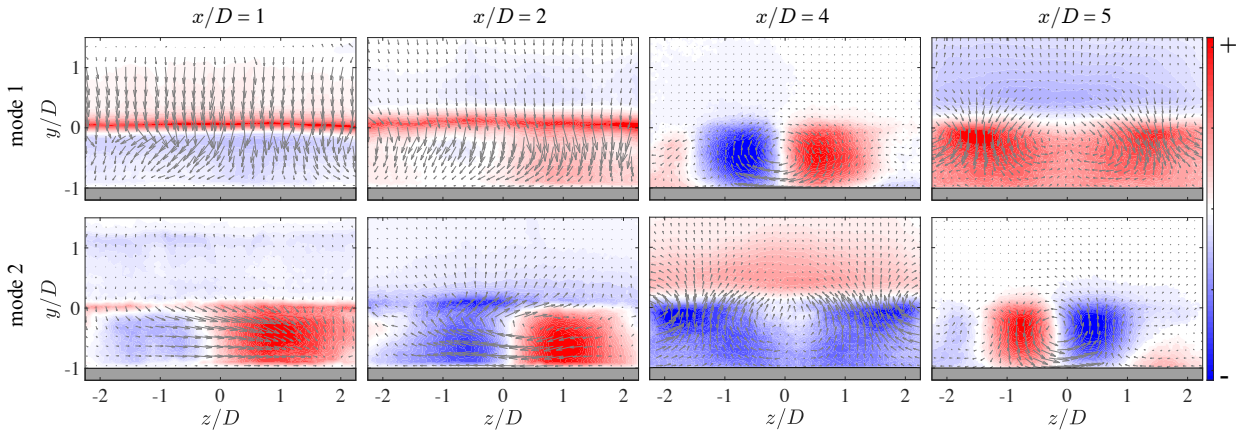

Figure 62: First 2 POD modes for baseline flow at different streamwise locations. Contours represent the streamwise u-velocity component with $v - w$ component vectors laid on top.

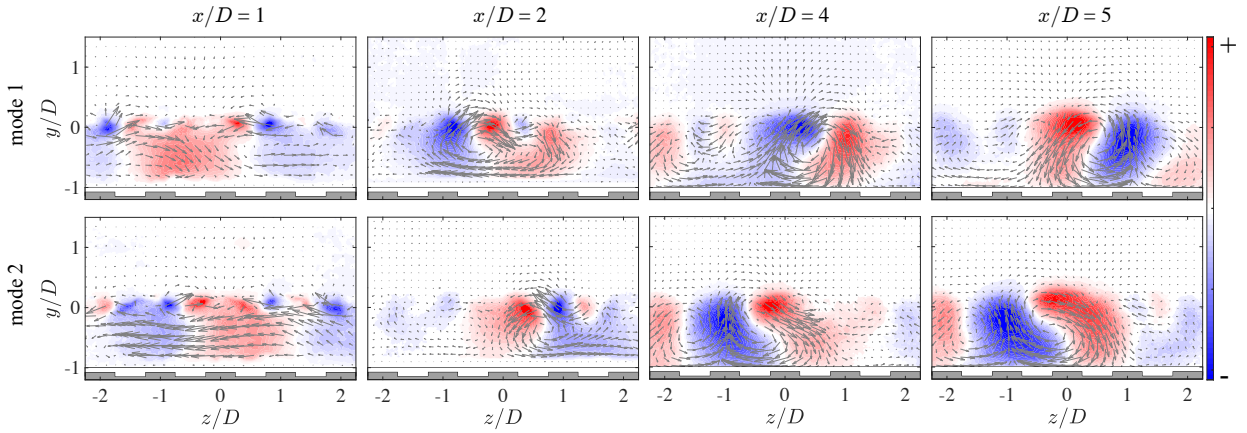

Figure 63: First 2 POD modes for controlled ($\delta/4$ tabs) flow at different streamwise locations. Contours represent the streamwise u-velocity component with $v - w$ component vectors laid on top.

The first 2 POD modes at various streamwise locations for the baseline flow can be seen in Fig 62. With the exception of $x/D = 4$, the first POD mode at all streamwise locations shows evidence of the large recirculation characteristics of the flow where the streamwise component is switched in the y-direction. As the flow moves downstream, sidewall interaction becomes more prominent evidenced by magnitude of vectors located closer to the sidewall. Again, with the exception of $x/D = 4$, the second POD mode at all locations shows alternating bands of streamwise eigenvectors in the spanwise direction. This hints at large vortical structures in the $x - z$ plane. It is noted that at $x/D = 4$, the first 2 POD modes are switched in comparison to the other locations with the first mode showing alternate streamwise bands and the second mode showing sidewall interaction. This may be due to the fact the energy fraction captured by the first 2 POD modes are very close to each other and the second mode is just as energetic as the first resulting in mode switching/mixing.

The leading 2 POD modes for the controlled flow can be seen in Fig 63. At $x/D = 1$, modes are localized in a small region (in the y-direction) spanned by the tabs upstream of

it. These modes appear to have the spanwise wavelength of the tabs ($\overline{\lambda} = 1$) as expected. In addition, there are also modes closer to the cavity floor, which are of comparatively larger wavelength. The clear distinction between these two sets of modes shows that even though the smaller scale structures have been created by these tabs, flow mixing is still incomplete. However, at $x/D = 2$, POD modes associated with the controlled flow show that the modes have grown ($\overline{\lambda} > 1$) and the flow mixing is complete as they extend from the cavity lip line to the cavity floor. These structures increase in size further downstream i.e. at $x/D = 4$ and 5 ($\overline{\lambda}$ around 2). An overall noticeable pattern is that the first two modes (with percentage energy very close to each other) at various streamwise locations seem to occur in pairs and appear to be anti-symmetric about the $z = 0$ axis. This characteristic is consistent with existence of counter-rotating vortex pairs (CVP) in the flow. In conclusion, for the controlled cavity, CVP exist (evidenced by first 2 modes) and grow as they convect downstream.

To further elucidate the differences between the baseline and the controlled flow, both flows were visualized using a surface flow visualization technique. For visualization, a mixture of oil and fluorescent powder was prepared and introduced as droplets at various locations in the cavity before running the wind tunnel. A neon black light was used to illuminate these droplets in the flow. A Nikon DSLR D5300 camera was positioned at various angles to the flow surfaces to take images of the oil film on the surface while the wind tunnel was running to capture different flow patterns. Some major surface streaklines have been enhanced by drawing curves on top of them which also show their direction. A top view of the cavity floor for the baseline and controlled cases are shown in Fig 64. Similar flow patterns are observed for these two cases. The flow bifurcates into two foci near the leading edge. These two regions show evidence of horseshoe vortices. These observations are similar to those observed ahead of a backward facing step in Tinney and Ukeiley (2009) and have also been observed for subsonic and supersonic open cavities in Sun et al. (2016).

These two vortices meet in a separation line near $x/D = 1$ (indicated by dashed lines in the figures). The reversal of flow direction with respect to freestream flow within the cavity is evident by streaklines that travel upstream from the aft wall which is indicative of mean recirculation of the flow. The distinction between the baseline and controlled cases is observed in the size and location of the horseshoe vortices. The horseshoe vortices associated with the baseline flow form closer to the cavity midspan (around $z/D = \pm 1$). Consequently, secondary vortices develop around $z/D = \pm 2$. For the controlled flow, the primary horseshoe vortices form around $z/D = \pm 2$ and strong secondary vortices are not observed. Also streaklines (marked by arrowheads) originate from the cavity sidewall for both flows, although greater three-dimensionality is observed near the sidewalls in the controlled case. Similar patterns have also been observed in Tinney and Ukeiley (2009).

Aft wall surface flow are also included in Fig 64. These images were taken at an angle and were transformed using perspective projection to obtain images in the plane of the aft wall ($y - z$ plane). Along the aft wall, for both baseline and controlled cavity flows, a downwash of fluid from top to bottom of the cavity is observed as indicated by the direction of the arrowheads. For the baseline case, streaklines on the cavity aft wall show that most of the flow moves towards the cavity midspan except for regions near the sidewalls $|z|/D > 1.5$. The controlled case shows that nearly all of the flow migrates towards the midspan. The streakline patterns of both cases are consistent with mean velocity vector plots at $x/D = 5$ for the baseline and controlled cases (Fig 58). These observations are consistent with cavity aft wall measurements in Crook et al. (2013) and also the fact that sidewall interaction is prominent for baseline cavity flow.

Some irregularities in the baseline cavity flow are observed on both the cavity floor and aft wall views. Even though the horseshoe vortices in the flow are symmetric about centerline, the flow downstream is slightly asymmetric about the midspan, apparently centered around $z/D \approx -0.33$. This could be due to an apparent larger extent of sidewall

influence and warrants further investigation.

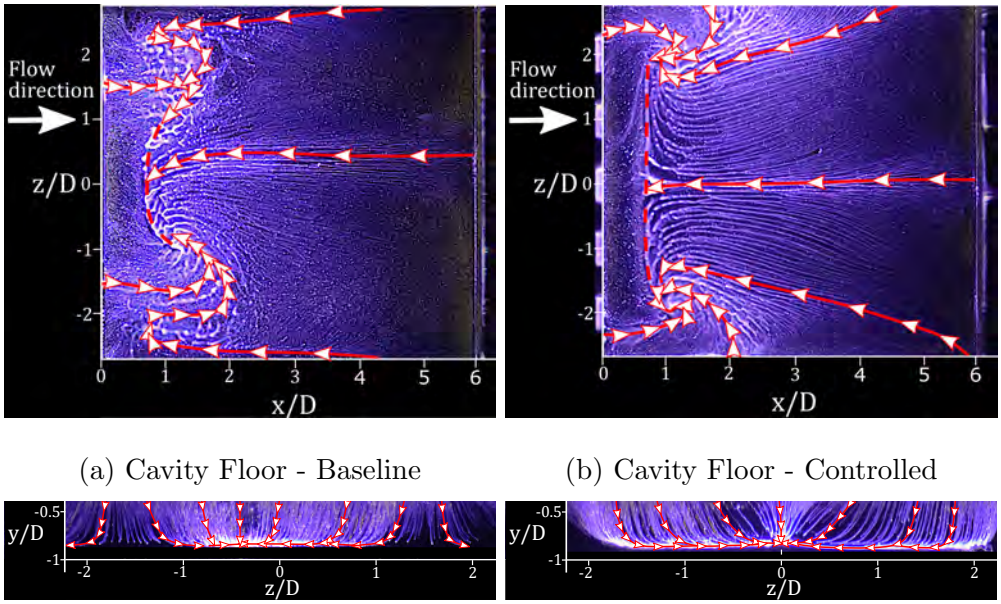

(a) Cavity Floor - Baseline

(b) Cavity Floor - Controlled

(c) Aft wall - Baseline

(d) Aft wall - Controlled

Figure 64: Surface flow visualization images for the baseline and controlled ($\delta/4$ tabs) flows.

4 Summary

This study presented a combined numerical and experimental effort to understand and control high speed flow over an open cavity in both subsonic and supersonic free stream conditions. To compliment the flow physics studies novel data driven analysis tools were examined and some new ones developed. Details of the important results include.

- A comparative analysis between snapshot POD and frequency based POD was conducted based on different mode parameters. Eigenvalue spectra in the frequency–POD mode number space reveal that the leading snapshot POD modes do not represent the dominant frequencies, whereas leading space–time POD modes do. Convergence plots in the frequency–POD mode number space showed faster convergence for eigenvalues of space–time POD as compared to eigenvalues of snapshot POD.Low-order

velocity reconstructions from both of the applications were compared in terms of the time evolution of instantaneous fluctuations, rms velocities, as well as the average power spectrum, keeping the energy content constant. The time evolution of low-order velocity reconstructions reveals that, even for moderately low-energy content (35 %), frequency-based POD modes represented the large-scale eddies and their dynamics that are present in the measured velocity fluctuation field. Snapshot POD reconstructions, however, fail to represent some of the finer details of the flow. Also, in comparison, rms fields of space–time POD reconstructions better represent the original flowfield. On further examination, PSD plots of wall-normal velocity fluctuations for a representative point in the cavity shear layer show that, even for very low-order velocity reconstructions, frequency-based POD captures the most dominant frequencies and starts to better represent the PSD plot of the original fields. Overall the modes from the frequency dependent POD are consistent with Rossiter's definition of streamwise modes at the expected frequencies.

- The spectral analysis modal methods (SAMMs) was developed to perform POD in both space and time using non-time-resolved particle image velocity (PIV) data combined with unsteady surface pressure measurements. Using a frequency-domain MIMO model combined with conditional spectral analysis, we can obtain independent inputs to the system and obtain a very good low-rank approximation of the dynamics obtained from frequency domain POD of the TR-PIV data. The eigenvector A of the input auto-/cross-spectral matrix is linked with the POD modes of the velocity fields through the transfer matrix H between the pressure and velocity field. The demonstration here showed that the modes can be captured very well with only 2 sensors from the cavity surface in SAMMs.

- Resolvent analysis was performed with respect to the time-averaged Mach 1.4 tur-

bulent cavity flow. The resolvent analysis uncovered the dominant input–output characteristics with a leading pair of forcing and response modes and the gain that represents the amount of amplification for the mode pair for a combination of forcing frequency and spanwise wavenumber. The response modes showed spatial oscillations over the shear layer with the corresponding forcing mode exhibiting high-amplitude input near the leading edge of the cavity. While the results suggest a certain three-dimensional actuation strategy naively choosing the modes with the highest gain may not be the optimal control set-up since it does not suggest how the mean flow can be modified. To further develop reliable control guideline a methodology was developed to assess the extent of how long lived the control input survives. The output of that analyis was used for unsteady blowing simulations with spanwise variation along the cavity leading edge. The simulated flows showed that the optimal flow control candidate achieved a remarkable r.m.s. pressure reduction along the cavity walls of 52 %. The control input reduced the pressure fluctuations by hindering the emergence of large spanwise vortices and by eliminating the obstructions responsible for creating oblique shock waves over the cavity.

- An array spanwise arranged tabs were developed to mimic the flow penetration from previous leading edge blowing conditions to assess the differences in passive and active leading edge flow control. The analysis suggests that the passive leading-edge control alters the development of the shear layer at the cavity opening in numerous ways. First, the tab structures cause increased lifting of the cavity shear layer, which reduces the strength of the interaction of the shear layer with the aft wall. Second, the spanwise arrangement of the tabs causes streamwise counter-rotating vortex pairs to form, which disrupt the spanwise aligned vortical structures and increase mixing of the flow. The manner in which the counter-rotating vortex pairs alter the cavity

shear layer structure was revealed through POD showing that the eigenvalue spread and growth trends along the cavity length in the baseline versus controlled case. Velocity measurements and surface flow visualization show that the tabs modify the large-scale recirculation of the flow in the cavity, which altered the cavity flow shear layer. Overall the mechanisms presented here are consistent with that of previous studies of leading edge blowing highlighting that the alterations in the cavity flow are more due blockage in the approaching boundary layer than mass addition. Further indicating that time dependent actuation from a oscillating tab should yield similar results to that of pulsed blowing jet.

References

Arunajatesan, S., C. Kannepalli, N. Sinha, M. Sheehan, F. Alvi, G. Shumway, and L. Ukeiley (2009). Suppression of cavity loads using leading-edge blowing. *AIAA J 47*(5), 1132–1144.
https://doi.org/10.2514/1.38211.

Arunajatesan, S., C. Kannepalli, and L. Ukeiley (2007). Three Dimensional Stochastic Estimation Applied to Cavity Flow Fields. *37th AIAA Fluid Dynamics Conference and Exhibit*.

Aström, K. J. and R. M. Murray (2010). *Feedback systems: an introduction for scientists and engineers.* Princeton Univ. Press.

Aubry, N., P. Holmes, J. L. Lumley, and E. Stone (1988). The dynamics of coherent structures in the wall region of a turbulent boundary layer. *Journal of Fluid Mechanics 192*, 115–173.
https://doi.org/10.1017/S0022112088001818.

Bartlett, M. (1948). Smoothing periodograms from time-series with continuous spectra. *Nature 161*(4096), 686.

Bartlett, M. (1950). Periodogram analysis and continuous spectra. *Biometrika 37*(1/2), 1–16.

Bechara, W., C. Bailly, P. Lafon, and S. M. Candel (1994). Stochastic approach to noise modeling for free turbulent flows. *AIAA J. 32*(3), 455–463.

Bendat, J. S. and A. G. Piersol (2011). *Random Data: Analysis and Measurements Procedures* (4 ed.), Volume 729. John Wiley & Sons.

Beresh, S., S. Kearney, J. Wagner, D. Guildenbecher, J. Henfling, R. Spillers, B. Pruett, N. Jiang, M. Slipchenko, J. Mance, et al. (2015). Pulse-burst piv in a high-speed wind tunnel. *Measurement Science and Technology 26*(9), 095305.

Beresh, S. J., J. L. Wagner, and K. M. Casper (2016). Compressibility effects in the shear layer over a rectangular cavity. *J. Fluid Mech. 808*, 116–152.

Beresh, S. J., J. L. Wagner, K. M. Casper, E. P. DeMauro, J. F. Henfling, and R. W. Spillers (2017). Spatial distribution of resonance in the velocity field for transonic flow over a rectangular cavity. *AIAA journal 55*(12), 4203–4218. https://doi.org/10.2514/1.J056106.

Berkooz, G., P. Holmes, and J. L. Lumley (1993). The proper orthogonal decomposition in the analysis of turbulent flows. *Annu Rev Fluid Mech 25*(1), 539–575. https://doi.org/10.1146/annurev.fl.25.010193.002543.

Brès, G. A. and T. Colonius (2008). Three-dimensional instabilities in compressible flow over open cavities. *J. Fluid Mech. 599*, 309–339.

Brès, G. A., F. E. Ham, J. W. Nichols, and S. K. Lele (2017, April). Unstructured large-eddy simulations of supersonic jets. *AIAA J. 55*(4), 1164–1184.

Chu, B.-T. (1965). On the energy transfer to small disturbances in fluid flow (part I). *Acta Mechanica 1*(3), 215–234.

Crook, S. D., T. C. W. Lau, and R. M. Kelso (2013). Three-dimensional flow within shallow, narrow cavities. *J Fluid Mech. 735*, 587–612. https://doi.org/10.1017/jfm.2013.519.

Dudley, J. G. and L. Ukeiley (2014). Passively controlled supersonic cavity flow using a spanwise cylinder. *Exp Fluids. 55*(9), 1810. https://doi.org/10.1007/s00348-014-1810-9.

Elimelech, Y., J. Vasile, and M. Amitay (2011). Secondary flow structures due to interaction between a finite-span synthetic jet and a 3-D cross flow. *Phys. Fluids 23*(9), 094104.

George, B., L. S. Ukeiley, L. N. Cattafesta, and K. Taira (2015). Control of three-dimensional cavity flow using leading-edge slot blowing. AIAA Paper 2015-1059.

Glauser, M. and W. George (1987). Orthogonal decomposition of the axisymmetric jet mixing layer including azimuthal dependence. In G. Comte-Bellot and J. Mathieu (Eds.), *Advances in Turbulence*, pp. 357–366. New York: Springer. https://doi.org/10.1007/978-3-642-83045-7_40.

Gómez, F., H. M. Blackburn, M. Rudman, B. J. McKeon, M. Luhar, R. Moarref, and A. S. Sharma (2014). On the origin of frequency sparsity in direct numerical simulations of turbulent pipe flow. *Phys. Fluids 26*(10), 101703.

Grafarend, E. W. (2006). *Linear and nonlinear models: fixed effects, random effects, and mixed models*. Walter de Gruyter, Berlin.

Griffin, J., T. Schultz, R. Holman, L. S. Ukeiley, and L. N. Cattafesta (2010). Application of multivariate outlier detection to fluid velocity measurements. *Exp Fluids. 49*(1), 305–317.
https://doi.org/10.1007/s00348-010-0875-3.

Heller, H. and D. Bliss (1975). The physical mechanism of flow-induced pressure fluctuations in cavities and concepts for their suppression. In *AIAA Paper 1975-0491.*
https://doi.org/10.2514/6.1975-491.

Heller, H., D. Holmes, and E. Covert (1971, oct). Flow-induced pressure oscillations in shallow cavities. *Journal of Sound and Vibration 18*(4), 545–553.

Hunt, J. C. R., A. A. Wray, and P. Moin (1988). Eddies, streams, and convergence zones in turbulent flows. *Proc. of the Summer Program, Center of Turbulence Research*, 193–208.

Jovanović, M. R. (2004). *Modeling, analysis, and control of spatially distributed systems.* Ph. D. thesis, University of California at Santa Barbara.

June, J., B. Bertolucci, L. Ukeiley, L. N. Cattafesta III, and M. Sheplak (2017). Diagnostic techniques to elucidate the aerodynamic performance of acoustic liners. Technical report, NASA. CR–2017–219583.

Khalighi, Y., F. Ham, P. Moin, S. K. Lele, and R. H. Schlinker (2011). Noise prediction of pressure-mismatched jets using unstructured large eddy simulation. In *ASME 2011 Turbo Expo: Turbine Technical Conference and Exposition*, pp. 381–387.

Liu, Q., Y. Sun, C.-A. Yeh, L. S. Ukeiley, L. N. Cattafesta, and K. Taira. Unsteady control of supersonic turbulent cavity flow based on resolvent analysis. *J Fluid Mech. 925.*

Lumley, J. L. (1967). The structure of inhomogeneous turbulent flows. In A. M. Yaglom and V. I. Tatarski (Eds.), *Atmospheric turbulence and radio propagation*, pp. 166–178.

Lusk, T., L. Cattafesta, and L. Ukeiley (2012). Leading edge slot blowing on an open cavity in supersonic flow. *Exp Fluids. 53*(1), 187–199. https://doi.org/10.1007/s00348-012-1282-8.

McKeon, B. J. and A. S. Sharma (2010). A critical-layer framework for turbulent pipe flow. *J. Fluid Mech. 658*, 336–382.

Murray, N., E. Sällström, and L. Ukeiley (2009). Properties of subsonic open cavity flow fields. *Phys Fluids 21*(9), 095103. https://doi.org/10.1063/1.3210772.

Rossiter, J. E. (1964). Wind-tunnel Experiments on the Flow over Rectangular Cavities at Subsonic and Transonic speeds. Technical report, Aeronautical Research Council Reports and Memoranda. No. 3438.

Schmid, P. J. and D. S. Henningson (2001). *Stability and transition in shear flows*. Springer.

Schmidt, O. T. and T. Colonius (2020a). Guide to Spectral Proper Orthogonal Decomposition. *AIAA Journal 58*(3), 1023–1033.

Schmidt, O. T. and T. Colonius (2020b). Guide to spectral proper orthogonal decomposition. *AIAA Journal 58*(3), 1023–1033.

Schmidt, O. T., A. Towne, T. Colonius, A. V. G. Cavalieri, P. Jordan, and G. A. Brès (2017). Wavepackets and trapped acoustic modes in a turbulent jet: coherent structure eduction and global stability. *J. Fluid Mech. 825*, 1153–1181.

Schmidt, O. T., A. Towne, G. Rigas, T. Colonius, and G. A. Brès (2017). Spectral analysis of jet turbulence. *J. Fluid Mech. 855*(25), 953–982.

Shaw, L. (1998). Active control for cavity acoustics. AIAA Paper 1998-2347.

Singh, S. and L. Ukeiley (2020). Proper orthogonal decomposition of high-speed particle image velocimetry in an open cavity. *AIAA J 58*(7), 2975–2990. https://doi.org/10.2514/1.j059046.

Sirovich, L. (1987, Oct). Turbulence and the dynamics of coherent structures, part i-iii. *Quarterly of Applied Mathematics 45*(3), 561–590.

Sun, Y., Q. Liu, L. N. Cattafesta, L. S. Ukeiley, and K. Taira (2019). Effects of sidewalls and leading-edge blowing on flows over long rectangular cavities. *AIAA J. 57*(1), 106–119.

Sun, Y., K. Taira, L. N. Cattafesta, and L. S. Ukeiley (2017a). Biglobal instabilities of compressible open-cavity flows. *J Fluid Mech. 826*, 270–301. https://doi.org/10.1017/jfm.2017.416.

Sun, Y., K. Taira, L. N. Cattafesta, and L. S. Ukeiley (2017b). Biglobal stability analysis of compressible open cavity flow. *J. Fluid Mech. 826*, 270–301.

Sun, Y., Y. Zhang, K. Taira, L. N. Cattafesta, B. George, and L. S. Ukeiley (2016). Width and sidewall effects on high speed cavity flows. In *AIAA Paper 2016-1343*. https://doi.org/10.2514/6.2016-1343.

Taira, K., S. L. Brunton, S. T. M. Dawson, C. W. Rowley, T. Colonius, B. J. McKeon, O. T. Schmidt, S. Gordeyev, V. Theofilis, and L. S. Ukeiley (2017, dec). Modal analysis of fluid flows: An overview. *AIAA Journal 55*(12), 4013–4041.

Tinney, C. and L. Ukeiley (2009). A study of a 3-D double backward-facing step. *Exp Fluids. 47*(3), 427–438. https://doi.org/10.1007/s00348-009-0675-9.

Tinney, C. E., F. Coiffet, J. Delville, A. M. Hall, P. Jordan, and M. N. Glauser (2006, Nov). On spectral linear stochastic estimation. *Experiments in Fluids 41*(5), 763–775.

Toro, E. F., M. Spruce, and W. Speares (1994). Restoration of the contact surface in the HLL-Riemann solver. *Shock Waves 4*, 25–34.

Towne, A., O. T. Schmidt, and T. Colonius (2018). Spectral proper orthogonal decomposition and its relationship to dynamic mode decomposition and resolvent analysis. *Journal of Fluid Mechanics 847*, 821–867.

Trefethen, L. N. and M. Embree (2005). *Spectra and pseudospectra: the behavior of nonnormal matrices and operators*. Princeton University Press.

Tutkun, M. and W. K. George (2017). Lumley decomposition of turbulent boundary layer at high reynolds numbers. *Physics of Fluids 29*(2), 020707. https://doi.org/10.1063/1.4974746.

Ukeiley, L., L. Cordier, R. Manceau, J. Delville, M. Glauser, and J. Bonnet (2001). Examination of large-scale structures in a turbulent plane mixing layer. part 2. dynamical systems model. *Journal of Fluid Mechanics 441*, 67–108. https://doi.org/10.1017/S0022112001004803.

Vreman, A. W. (2004). An eddy-viscosity subgrid-scale model for turbulent shear flow: algebraic theory and applications. *Phys. Fluids 16*(10), 3670–3681.

Wieneke, B. (2015). PIV uncertainty quantification from correlation statistics. *Meas Sci Technol 26*(7), 074002. https://doi.org/10.1088/0957-0233/26/7/074002.

Williams, D. R., D. Cornelius, and C. W. Rowley (2007). Supersonic cavity response to open-loop forcing. In *Active Flow Control*, pp. 230–243. Springer.

Yeh, C.-A. and K. Taira (2019). Resolvent-analysis-based design of airfoil separation control. *J. Fluid Mech. 867*, 572–610.

Zhang, Y., L. Cattafesta, and L. Ukeiley (2019, Aug). A spectral analysis modal method applied to cavity flow oscillations. In *11th International Symposium on Turbulence and Shear Flow Phenomena (TSFP10)*, Southampton, UK.

Zhang, Y., Y. Sun, N. Arora, L. N. Cattafesta, K. Taira, and L. S. Ukeiley (2019). Suppression of cavity flow oscillations via three-dimensional steady blowing. *AIAA J. 57*(1), 90–105.

Zhang, Y., Y. Sun, N. Arora, L. N. C. III, K. Taira, and L. S. Ukeiley (2019, jan). Suppression of cavity flow oscillations via three-dimensional steady blowing. *AIAA Journal 57*(1), 90–105.

Zhuang, N., F. S. Alvi, M. B. Alkislar, and C. Shih (2006). Supersonic cavity flows and their control. *AIAA J 44*(9), 2118–2128. https://doi.org/10.2514/1.14879.